Department of Precision and Microsystems Engineering

An experimental setup for photonic integrated circuit alignment sensors

Name

Report no : 2021.096
Coach : Dr.Ir. L.A. Cacace
Professor : Prof.Dr.Ir. J.L. Herder
Specialisation : Opto-mechatronics
Type of report : Thesis report
Date : 9-12-2021

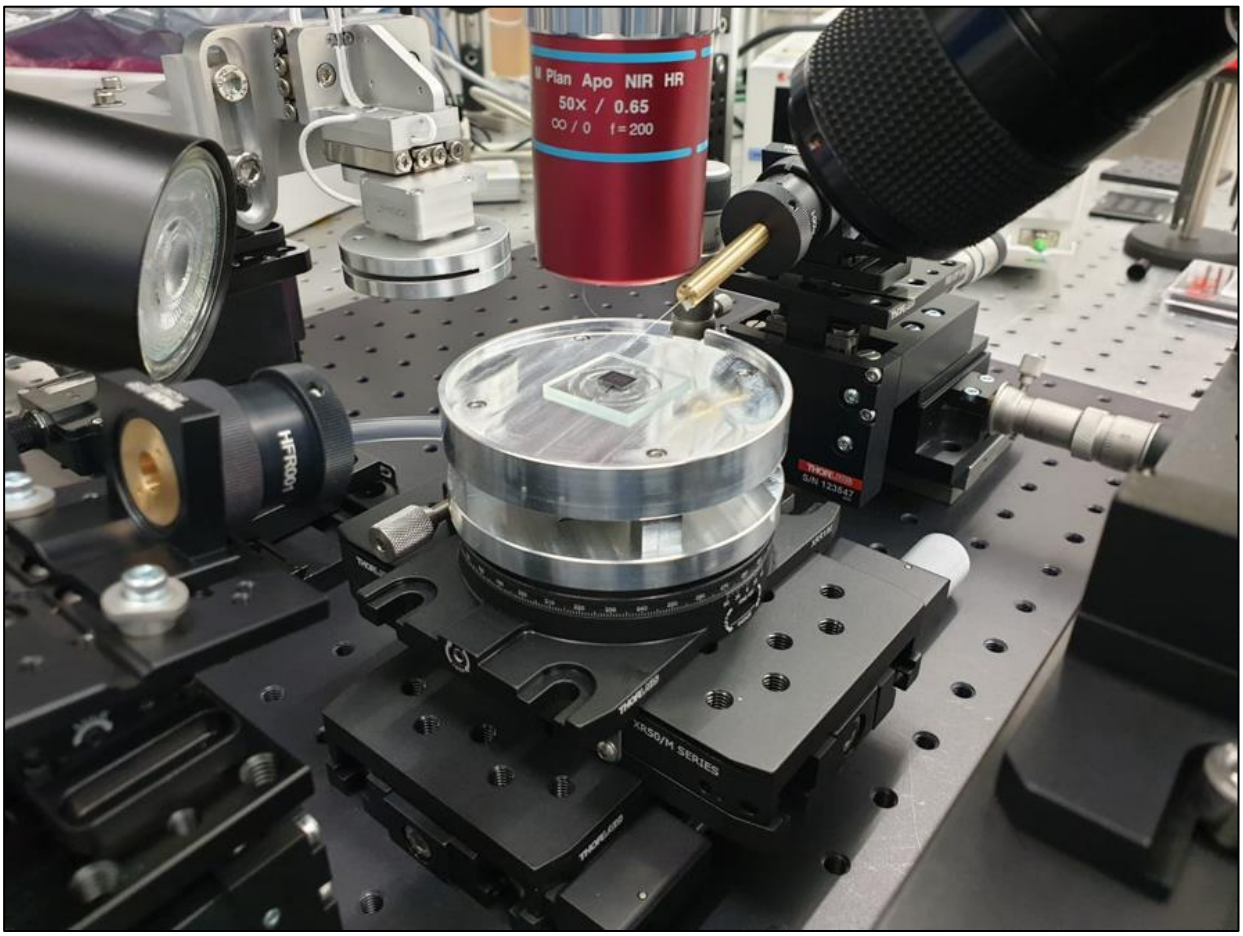

An experimental setup for photonic integrated alignment sensors

Thesis report

M.R. Otto

Technische Universiteit Delft

TU Delft

An experimental setup for photonic integrated alignment sensors

Thesis report

by

M.R. Otto

to obtain the degree of Master of Science
at the Delft University of Technology,
to be defended publicly on Thursday December 9, 2021 at 15:00.

Student number:	4449304	
Project duration:	November 9, 2020 – December 9 , 2021	
Thesis committee:	Prof.Dr.Ir. J.L. Herder,	TU Delft, chair
	Dr.Ir. L.A. Cacace,	TU Delft, supervisor
	Dr.Ir. W.J. Westerveld,	TU Delft
	Dr.Ir. I.D. Setija,	ASML, supervisor

TU Delft

Abstract

The ever-growing demand for smaller microchip feature sizes and thus more powerful chips, has fuelled innovation in photolithography machines for decades. Currently, within this context, one possibility that is explored at ASML involves an increase in the number of alignment markers on a wafer, for a more accurate mapping of local wafer deformations. The current alignment marker metrology system consists of a diffraction-based sensor that is space consuming and measures the markers one-by-one. To prevent a longer total measurement time due to a larger number of markers, parallel read-out is pursued by miniaturisation of the sensor. The technology that is explored for this miniaturisation is integrated optics, in which classical optical components are replaced by their waveguide-based equivalent structures on a chip-sized sensor. Contributing to the feasibility study of integrated optics for ASML's wafer metrology, this work focuses on the design, construction and verification of an experimental setup for photonic integrated circuit (PIC) alignment sensors. The setup is capable of characterizing the output beams of grating couplers, important PIC components, by imaging their intensity profiles at different locations along their propagation direction. Spots of 40 µm can be imaged with a spatial resolution of 0.3 µm and an expected Z-position accuracy of 6 µm. The setup is also able to scan alignment marks with a PIC alignment sensor, with an expected repeatability of 1.1 nm. Anticipating completion of the first PIC alignment sensor designed by the TU Eindhoven, measurements on an alternative PIC containing elementary structures were conducted. Successful coupling between angle polished fibers and 15x15µm grating couplers was achieved, with a verified coupling efficiency of 21.4±3.6%, compared to a coupling efficiency of 28% with the conventional flat end-face fiber coupling method.

M.R. Otto
The Hague, November 2021

Contents

1
Introduction

Semiconductors are heavily embedded in our everyday life, as part of consumer electronics like televisions and smartphones, or by making their appearance in devices ranging from coffee machines to automobiles to airplanes. The semiconductor industry has seen incredible growth since it became a profitable business occupation around the 1960s. Especially during the past few years, due to innovations in technologies like artificial intelligence and the Internet of Things, the demand for more functionalities assembled on smaller integrated circuits has made a significant impact on the semiconductor industry [1]. An observation called Moore's law states that the number of transistors on a chip doubles every two years (figure 1.1). It is an observation made in 1965, as well as a prediction that has held valid for 50 years now [2]. The constant accumulation of developments in and around photolithography machines has had an enormous share in establishing this trend.

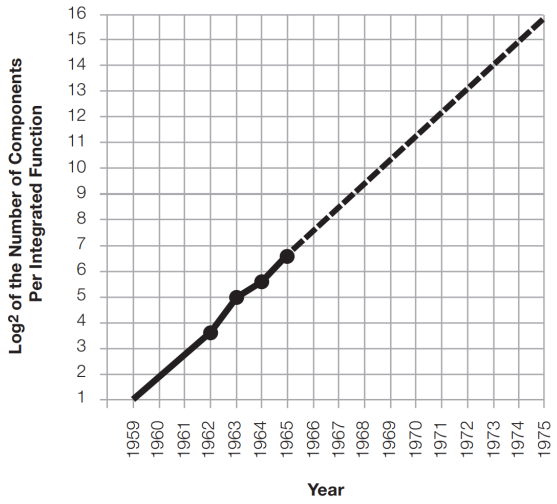

Figure 1.1: Moore's law; transistor density over the years [2].

1.1. The next step in wafer alignment

The most recent generation EUV photolithography machines of ASML is capable of producing chips with feature sizes down to 5 nm. The semiconductor manufacturing process entails several steps of depositing, processing and removing material on a silicon wafer. After all steps have been taken, there is a layer of features on the wafer. The same process is carried out a number of times, dependent on the chip design, for multiple layers of features. The step that is executed in the photolithography machine involves the wafer being exposed to light in a pattern corresponding to a particular layer of features. That means that the dimensions and locations of features of a layer are established in this process step. An associated process step is the alignment step. In order to reach the small feature dimensions of today, the position error between two successive layers of features, or the overlay error, must be kept to a minimum. This is partly accomplished by the alignment sensor, which is also located in the photolithography machine. In the alignment step, the layer to come at the exposure step is aligned with respect to the previous layer. On the wafer, a number of alignment markers is located. The alignment sensor accurately measures the position of these markers one by one in the plane of the wafer. With the locations of these markers, the orientation of the wafer as a whole

can be determined, and local deformations can be estimated and then accounted for [3]. Chip manufacturers are now demanding more alignment markers, so that local deformations can be determined more accurately. This will decrease the overlay error between layers and positively impact the density of features on the chip. However, an increased number of markers introduces a trade-off with the duration of the alignment process, since the alignment sensor measures the marker locations sequentially. Parallel read-out of the markers is not possible, since the sensor is too bulky for multiple of them to be situated alongside each other above the wafer. Before addressing the potential solution that is at the basis of this report, the alignment sensor working principle must be described.

The alignment sensor system in the lithography machine measures the position of alignment markers in the plane of the wafer. The alignment sensor at ASML is a diffraction-based measurement system, and it is capable of measuring the displacement of a diffraction grating. The working principle of the Athena alignment sensor, an earlier version of the sensor, is depicted in figure 1.2. The sensor illuminates an alignment mark, which is a diffraction grating, and captures the reflected diffraction orders $-m$ and $+m$. The orders are interfered with each other at a reference grating after, which has the same period as the interference pattern. A lateral translation of the marker relative to the sensor induces a phase shift of a reflected order conforming to [4]:

$$\Delta\Phi_m = \frac{2\pi m}{\Lambda}\delta x \tag{1.1}$$

where m is the diffraction order, Λ is the period of the marker, and δx is the displacement of the marker grating. The phase shift of the negative order differs in sign from the phase shift of the positive order. When interfering the two captured orders with each other and displacing the marker, the opposite phase shift of the orders causes a spatial shift of the interference pattern over the reference grating, resulting in a sinusoidal intensity signal at the detector behind the reference grating. From this alignment signal, the displacement of the marker can be deduced.

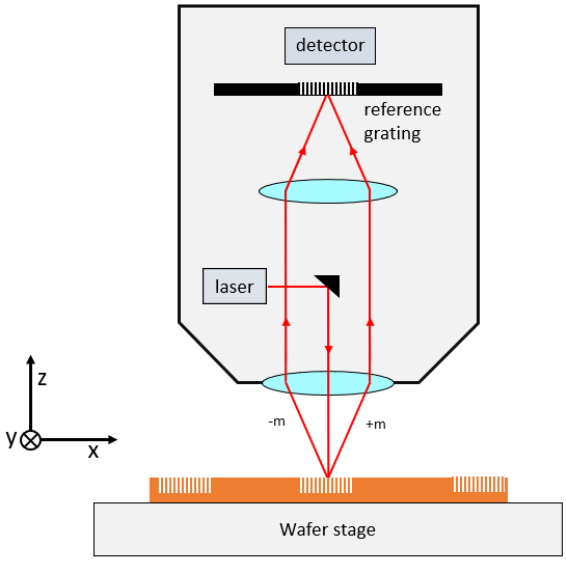

Figure 1.2: Working principle Athena alignment sensor

As mentioned, the alignment sensor as it currently exists, consists of relatively large optical components. To enable parallel read-out of the markers, ASML is exploring the possibility of reducing the size of the alignment sensor through a technology called photonic integration. In this design approach, classical optical components are replaced by their on-chip waveguide-based equivalent components. A photonic integrated alignment sensor could have dimensions in the order of only a few mm^2, allowing them to be positioned together in an array. Although integrated photonics as a technology is very mature, the exploration of the technique applied to alignment sensors for ASML lithography machines is in an early stage and is posing a number of new challenges. Before addressing those challenges, photonic integration or integrated optics requires an introduction.

1.2. Photonic integration

Photonic integration covers the processing and transmission of optical signals, not by traditional bulk optics (lens, beamsplitter, etc.), but through their on-chip waveguide-based equivalent components. A photonic integrated circuit (PIC), combining multiple photonic functions on one chip, provides numerous advantages with respect to both classical optics and electrical circuits. Compared to a conventional optical system, it is smaller, facilitates batch fabrication and has an improved optical alignment. Compared to electrical integrated circuits, photonic circuits have an increased bandwidth, due to the absence of the limiting effects of inductance and capacitance. In addition, there is less heat generation. A disadvantage would be the relatively large bending radii of waveguides, requiring more space than electrical guiding. With respect to either optical signal transmission through fiber or electric signal transmission through wire, the former is immune to electromagnetic interference and is free from short-circuiting [5]. The topic of photonic integration erupted in the early 1960s, with the first PIC being proposed in 1964 by Miller [6]. Since then, developments quickly succeeded each other, driven at first by telecommunication and data communication [7]. Fabrication remains expensive and although it has limited their commercial success in areas besides communication, a large amount of promising research is conducted and future potential applications in precision metrology, imaging and sensing are forthcoming [8]. New fabrication techniques have brought feature sizes down to nanometer dimensions. PIC's based on the Indium phosphide membrane on silicon (IMOS) platform have evolved rapidly over the last then years, because it enables active-passive integration, while maintaining the benefits of silicon photonics [9].

There is a diverse and broad selection of photonic integrated devices for PIC's, from lasers to photodetectors to interferometry modules. Before addressing the PIC alignment sensor and the experimental setup that is at the basis of characterizing PIC's, the working principles of two important photonic integrated devices must be explained: waveguides and grating couplers. Rectangular waveguides are the backbone of PIC's, transferring optical signals from component to component, some of which also consist of waveguide structures. Grating couplers are a diffraction-based method for coupling light in or out of the chip, from or to free space. They are extensively used in the PIC alignment sensor. See the subsections 1.2.1 and 1.2.2 below for a more detailed description. In subsection 1.2.3 the first PIC alignment sensor design is described, as it is at the base of this project.

1.2.1. Waveguides

Optical waves propagate through waveguides in distinct optical modes. An optical mode is a spatial distribution of optical energy, in one or multiple dimensions, remaining constant in time [5]. Which modes are supported by a waveguide depends on the refractive indices of the waveguide, superstrate (usually air), substrate (silicon in our case) and waveguide thickness. Considering a ray optics explanation approach, figure 1.3 shows a three-layer waveguide structure with a supported, or guided mode and a non-supported, or radiation mode. A guided mode experiences total internal reflection at the substrate and superstrate interfaces according to Snell's law, with $n_1 > n_{\text{sub}}$ and $n_1 > n_{\text{sup}}$. The discrete nature of guided modes is a result of constructive or destructive interference, which can again be visualized with figure 1.3. If we consider the plane wavefront of a totally reflected ray to be infinite, it overlaps with the wavefronts of the same ray, reflected up and down along the waveguide. A mode is only allowed to exist, if the wavefronts up or down of its ray path are completely in phase and constructively interfere; otherwise they will attenuate over short waveguide distances. The waveguides in the PIC alignment sensor support one mode, the fundamental mode, which has a Gaussian-like intensity profile.

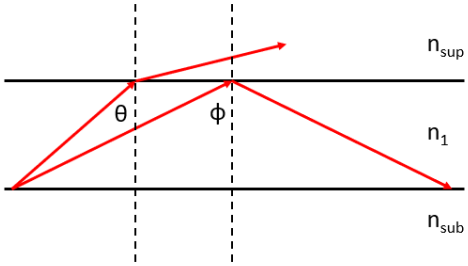

Figure 1.3: Ray-optic approach schematic of waveguide modes. $\phi > \phi_c$, where ϕ_c is the critical angle for total internal reflection.

1.2.2. Grating couplers

A grating coupler is a diffraction-based method to couple light into or out of an on-chip waveguide. These gratings induce diffraction of the waveguide mode, resulting in outward-directed diffraction orders. The PIC alignment sensor designed by Jasper de Graaf (see the following subsection 1.2.3) employs grating couplers for two different applications. Firstly, grating couplers are used for coupling light via fibers from an external light source into a PIC and from a PIC into an external measurement system. Secondly, they are used for emitting or capturing beams to or from an alignment marker. The particular gratings and their application will be discussed in section 1.2.3.

Grating couplers, with a period Λ are placed in or on top of the waveguide and induce diffraction of the waveguide mode according to [10]:

$$\Lambda = \frac{m\lambda_0}{n_{\text{eff}} - n_{\text{sup}}\sin(\theta)} \tag{1.2}$$

where θ_m is the diffraction angle of the order m, n_{eff} is the effective refractive index of the grating in the waveguide and n_{sup} is the refractive index of the superstrate (usually air). The wavelength in vacuum is denoted by λ_0. Important to mention is that the coupling process is reciprocal, so the equation is also applicable to a free space beam incident on the grating. Figure 1.4 shows a uniform grating coupler, where the optical power from the incoming waveguide (P_{wg}) is partly diffracted into the superstrate (P_{sup}) and partly into the substrate (P_{sub}). The distribution depends on the relative refractive indices: a smaller n_{sup} to n_{sub} ratio leads to a smaller P_{sup} to P_{sub} ratio. There are techniques to reduce these losses to the substrate, such as a layer between waveguide and substrate acting as a mirror [11] or the use of a blazed grating [12]. Implementation of these techniques in the PIC alignment sensor is described in section 1.2.3. Equation 1.2 shows a strong dependency on the wavelength of the output (or input) angle, which will play an important role in the feasibility of the PIC alignment sensor. This dependency limits the bandwidth of the coupler, which is usually the main disadvantage of grating couplers. The principal advantage of grating couplers in general is that they are an integral part of the PIC once fabricated, resulting in a constant coupling efficiency [5]. In addition, grating couplers allow for wafer-scale device characterization without the need for chip dicing and polishing, since they are exposed on the surface of the chip.

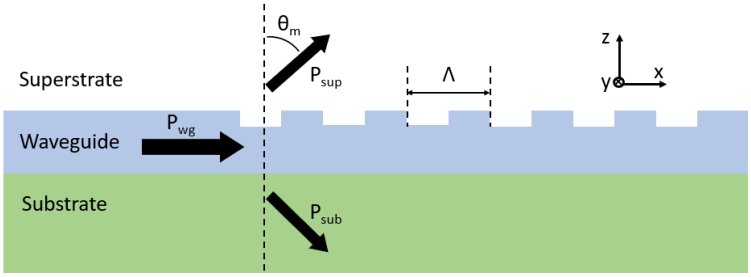

Figure 1.4: Diffraction orders out of waveguide induced by a uniform grating coupler [10].

1.2.3. PIC alignment sensor

The first PIC alignment sensor was designed by Jasper de Graaf. Its working principle and layout are clarified in this subsection. For a detailed description of the PIC alignment sensor subcomponents, the thesis report by de Graaf can be consulted [13]. Figure 3.1 shows a schematic of the PIC alignment sensor (blue surface) with a marker grating (MG) on a piece of wafer (orange surface). During operation in the lithography machine, the wafer moves underneath the PIC alignment sensor. The PIC alignment sensor has dimensions of 4 mm × 20 mm and operates similarly as ASML's Athena alignment sensor, explained in section 1.1. The operating wavelength of the PIC is 1550 nm. Via an emitting grating coupler (EG), the PIC focuses a converging Gaussian beam under an angle through free space onto the marker grating (MG) at a distance $z = 10\,\text{mm}$. Two specific diffraction orders (m) reflected by a standard ASML alignment mark, ideally diverging Gaussian beams, are picked up by the capturing grating couplers (CG). The optical signals from both capturing gratings are transferred via waveguides to the interferometry module, or beam combiner, on the PIC.

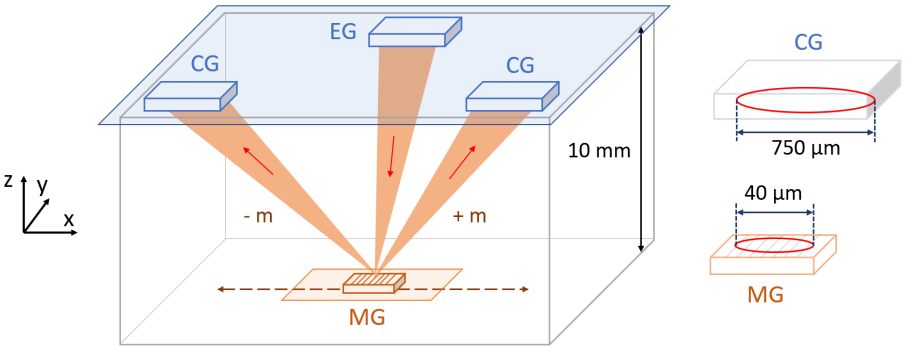

Figure 1.5: Schematic overview of PIC alignment sensor working principle. PIC in blue, wafer sample in orange. Focused Gaussian spot of 40 µm on marker grating (MG) and Gaussian spots of 750 µm on the capturing gratings (CG). Movement of wafer sample below PIC in x-direction.

The emitting and capturing gratings demand a more detailed explanation with respect to the Gaussian beam profile. The grating coupler with uniform grating from figure 1.4 produces a plane wave with an exponential intensity profile [14]:

$$P(z) = P_0 \exp(-2\alpha x) \tag{1.3}$$

It does not match the phase and intensity profile of a converging/diverging Gaussian beam. The leakage factor α however, depends on different grating properties like period, etch depth, filling factor (shown in figure 1.6) and material. In order to match a certain phase profile, the output angle θ_m must become a function of z over the waveguide, resulting in a grating period Λ variable over z. Matching the Gaussian intensity profile requires a variation in etch depth and/or filling factor [14]. In the design of the emitting grating, some of these techniques are applied to create a converging Gaussian output beam. The capturing gratings are designed to capture a diverging Gaussian beam. The techniques that can be applied to gratings to reduce the radiation losses to the substrate, which were shortly discussed in section 1.2.2, are not implemented in the gratings of the PIC alignment sensor, keeping the manufacturing process as simple as possible.

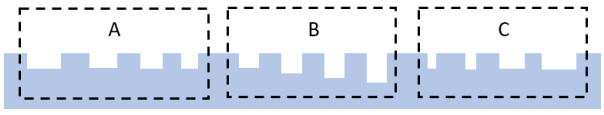

Figure 1.6: Schematic of different grating structures. A: variable grating period Λ for phase matching. B: variable etch depth for intensity matching. C: variable filling factor for intensity matching.

In figure 1.7 the complete PIC system flow is depicted, with indexing corresponding to the subsystem locations in the schematic top view of the PIC in figure 1.8. All PIC components are located on a single side of the IMOS wafer and are not accessible from the other side. Blue blocks are components on the PIC and the

orange block is the marker grating on the wafer sample. The transfer of optical signals through the PIC via waveguides is represented by the continuous arrows and transmission through air by the dashed arrows.

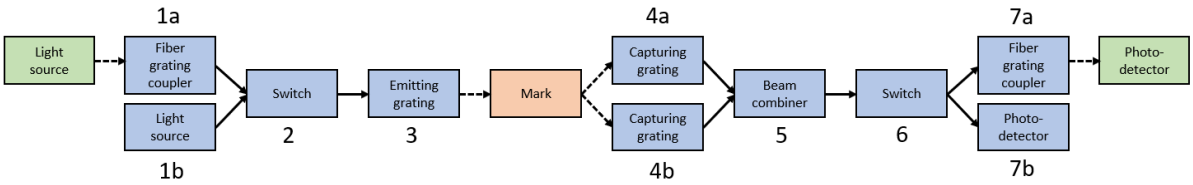

Figure 1.7: PIC system flow schematic. On-chip components indicated with blue.

The optical signal input for the emitting grating can either be inserted from an external light source (in green) via a fiber-to-chip grating coupler (fiber grating coupler) (1a), or by an integrated laser diode (1b). The laser diode is actuated by applying a current to its electrical probe pads, depicted in yellow. An opto-electronical switch (2) connected to both devices also requires electrical excitation, in order to select between the external or internal light source. On-chip devices that need excitation from a current or voltage source are called active devices and on-chip devices that do not are called passive devices. After the switch, the light travels through a waveguide to the emitting grating (3). In figure 1.8 the marker grating is out of screen at $z = 10\,\text{mm}$ from the PIC. The two diffraction orders captured by the capturing gratings (4) are propagated through waveguides and interfered at the beam combiner (5), which is an integrated Mach Zehnder interferometry configuration [15]. The output of the beam combiner passes a switch (6) again, after which the sensor alignment signal can be extracted passively, via the fiber grating coupler (7a), or actively, via an integrated photodetector (7b). In chapter 3 the relation between alignment signal and supposed marker displacement is explored more extensively. Figure 1.8 shows only the fifth-order system on the PIC for a standard ASML alignment mark, but the PIC also includes a third-order system and many separate subsystems (gratings, interferometry modules, etc.) for the sake of research. For an overview of the relevant PIC specifications for this project, the reader is referred to appendix A.

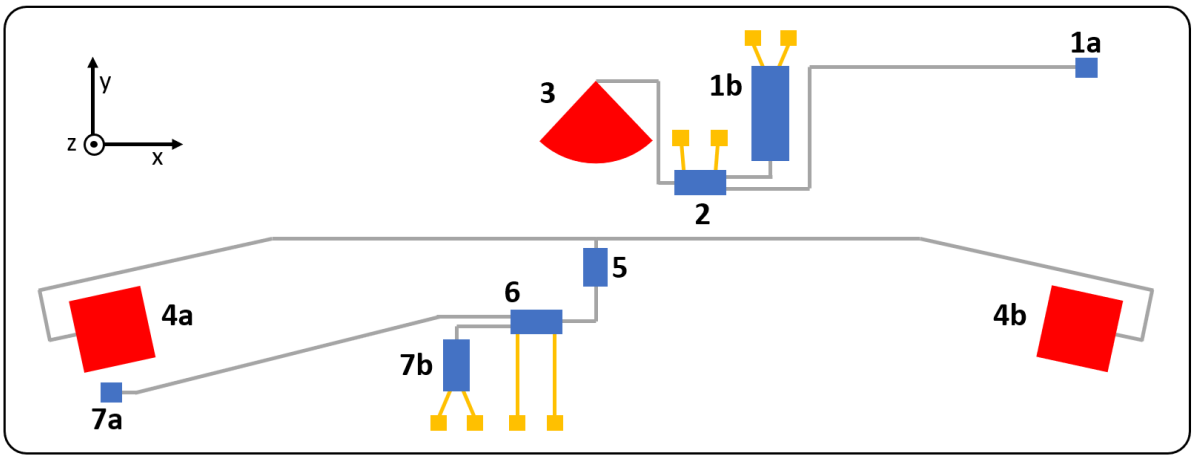

Figure 1.8: Schematic top view of the PIC alignment sensor (4 mm × 20 mm). Components in blue and red. Waveguides in grey. Electrical probe pads in yellow.

1.3. Project goal & report outline

As mentioned, integrated optics is very mature, but the exploration of the technique applied to alignment sensors for ASML lithography machines is in an early stage. The PIC alignment sensor discussed is the first of its kind ready for examination. The exploration of photonic integration introduces a number of new challenges. One of them is the testing and characterization of photonic integrated alignment sensors. This project aims to contribute to the feasibility study on PIC alignment sensors for ASML's lithography machines like the one described. It will do so by the realization of an experimental setup, able to investigate the required aspects of PIC's for this feasibility study, which translates to the project goal below.

Project goal

The design and construction of an experimental setup for PIC alignment sensors, capable of characterizing grating coupler output and acquiring an alignment signal through an alignment marker scan with the PIC.

Report outline

Below, an outline of the report is provided, shortly explaining the content and purpose of each chapter.

1. Introduction

The exploration of photonic integration for wafer metrology is introduced. A first PIC alignment sensor design by the TU/e is at the base of this project, which is why its working principle and structure are elaborated on, emphasizing the importance of grating coupler operation.

2. Setup requirements

The requirements of the setup are elaborated on in this chapter, which originate from the information in the introduction and appendices A and B. In order to study the feasibility of a PIC alignment sensor, the grating output must be characterized and an alignment marker scan must be conducted with the PIC. The requirements are categorized in 4 sections: Grating output characterization, Alignment marker scanning, Signal insertion & extraction and Environment & operation.

3. Alignment marker position measurement

Before turning to the design of the setup, the principles behind a marker position measurement by the alignment sensor are explained. An understanding of the different error sources impacting that marker position measurement is an essential preparation for the design choices concerning the alignment marker scan.

4. Concept creation

In the design process, the possibilities surrounding certain subsystems and the setup as a whole are explored first. The concept creation and selection of a few subjects are expanded on in this chapter: the beam profiling method, the fiber-to-chip coupling method and the configuration of all subsystems involved. Especially the configuration of the setup and its subsystems provides a foundation for the build-up of the detailed design.

5. Detailed design

The choice and design of the components per subsystem are presented and the alignment strategy of subsystems, PIC and alignment marker w.r.t. each other is illustrated. The error budgets, relating design choices to expected performances, are incorporated at the end of the chapter.

6. Setup verification

This chapter is concerned with the verification of certain aspects of the realized setup, conforming to its design in chapter 5. Since the manufacturing process of PIC alignment sensor experienced delays, initial measurements on it could not be conducted, and an alternative PIC is used for part of the verification steps.

7. Conclusion & recommendations

The results of chapter 6 are compared to the requirements of chapter 2 and the expectations from the detailed design in chapter 5. After concluding if the setup meets its requirements, a few recommendations for setup improvement and future research are mentioned.

2
Setup requirements

The goal of the experimental setup is to perform measurements contributing to the feasibility study on PIC alignment sensors. The requirements for this new setup are described and substantiated in this chapter, but before the requirements of the setup can be defined, PIC behaviour that is important to study and quantify must be identified. The most obvious operation that is to be examined is the performance of an alignment marker scan, which is thus one of the capabilities this setup must possess. Ideally, the PIC will produce an alignment signal like described in section 1.2.3. If the system does not behave the way it was designed to, the setup must also contain capabilities to find out why. The most critical elements in the PIC system are the emitting and capturing gratings. Their performance is crucial for the PIC behaviour and is prone to deviations by a number of factors, elaborated on in section 2.1, which influence the focal spot location and intensity profiles of the emitted bundles. Characterization of the grating coupler output is therefore the second feature that must be incorporated in the setup. Figure 2.1 shows the conceptual schematics of how these two functionalities are included in the setup. In figure 2.1A an alignment mark on a wafer sample is depicted during a scan over the PIC alignment sensor. Note that in contrast to the configuration of the alignment sensor in the lithography machine, the PIC within the novel experimental setup will be on the bottom (fixed), with its components facing up and the alignment mark scans over it. Figure 2.1 illustrates a bundle of light from one of the gratings, captured by an infrared imaging system, which records the intensity profiles at different planes over the z-direction and should allow for spot location comparison between the different gratings. Both setup capabilities will be discussed further in sections 2.1 and 2.2.

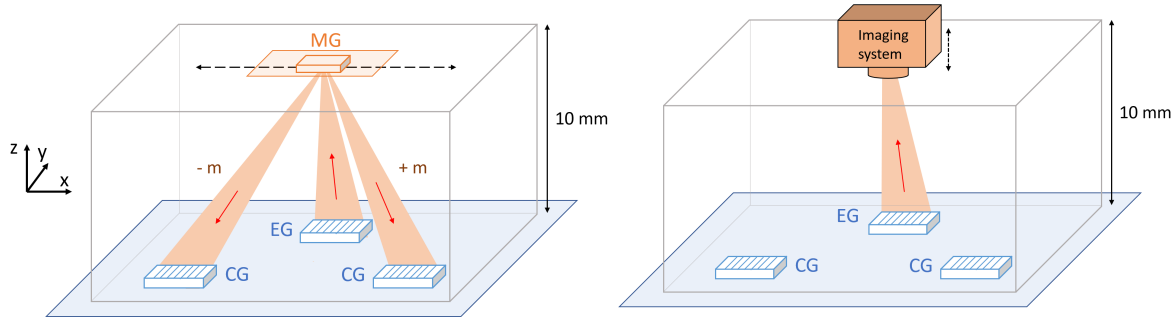

(a) Wafer sample with alignment mark translating over the PIC.

(b) Infrared imaging system, imaging the intensity profiles in different z-locations.

Figure 2.1: Conceptual schematics of experimental setup functionalities

The requirements that have been defined, following from the intended PIC properties to pursue, have been structured in the following four categories:

1. Grating output characterization
2. Alignment marker scanning
3. Signal insertion and extraction
4. Environment & operation

The requirements are explained per category in the sections below. Although this project covers experiments on the PIC from Jasper de Graaf, the requirements of the setup are not only constructed around this sensor, but also to some extent around possible future PIC designs, introducing versatility in certain requirements.

2.1. Grating output characterization

As discussed, the emitting and capturing gratings of a PIC alignment sensor are designed for a certain focal distance in z-direction with a Gaussian intensity profile. However, inherent design limitations obstruct a perfect Gaussian profile directly above the grating. Simulations performed with FDTD (finite-difference time-domain) methods show the effects at the focal distance, culminating in additional intensity peaks, or lobes, in the profile. Furthermore, the fabrication tolerance on the grating line width is ±30 nm. It will influence the output angle across the grating adhering to equation 1.2, ultimately resulting in an uncertainty in the overall output angle, focal distance and intensity profile.

Firstly, the grating outputs need to be characterized via measurements, after which they can be compared to the simulations. Important properties for this purpose are the focal distance in the Z-direction and the intensity profile at the focal distance. By measuring the intensity profile at multiple z-distances, the angle of the beam can also be retrieved.

A second operation in preparation of the alignment marker scan, would be to compare the spot locations in the designated focal plane of both the emitting grating and the capturing gratings, by using the latter as emitters (see 'reciprocity' in section 1.2.2). A deviation in the output angle of the emitting grating causes a alteration of the angle of the diffracted orders. If this angle differs significantly from the ideal angle accepted by the capturing gratings, the coupling efficiency will drop rapidly. This means that the more spots of all three gratings overlap at the intended focal distance, the better the performance of the alignment sensor will be.

The properties described above will be measured by an imaging system with the following requirements:

Spatial resolution
In order to sufficiently distinguish the beam features predicted by the simulations, the imaging system requires a certain spatial resolution. A rule of thumb for the spatial resolution in Gaussian beam intensity profiling is diameter divided by 20. With a minimum spot size at focus of 40 µm a spatial resolution below 2 µm is required.

Wavelength
The fabrication tolerances described above might alter the designed wavelength of the gratings. The dependency of the gratings to the wavelength is to be investigated around a wavelength of 1550 nm with at least ±15 nm. The system must capture light within this spectrum and avoid interference from other light sources.

Positioning
Besides recovering the intensity profile at the intended focal distance, we are also interested in the intensity profiles at different z-distances. The position of intensity profiles in the Z-direction will be absolutely determined within a range of 0 mm - 12 mm from the PIC with an accuracy of 25 µm. The range will allow for future PIC designs with slightly longer or shorter focal distances to be tested, but also for a better analysis of the beam properties. The accuracy originates from the alignment tolerances of a marker, discussed later on in this chapter. The gratings can be located anywhere on the IMOS wafer with a diameter of 75 mm, so the imaging system must be able to travel over this range in x- and y-direction, while adhering to the other requirements. The imaging system must also be removable from above the wafer surface to make place for the execution of the alignment mark scanning.

2.2. Alignment marker scanning

The scan of the wafer sample with alignment markers is the main purpose of the experimental setup, where behaviour of the alignment sensor as a whole is investigated. The current alignment sensor in the lithography machine measures the absolute locations of the markers it passes. In the experimental setup for the PIC absolute position measurement will not be necessary, so the focus will be on relative displacement and repeatability.

Scanning travel range
The scanning motion of the wafer sample with marker relative to the PIC is a translation over the x-axis (coordinate system figure 2.1a). High accuracy, absolute position determination with respect to a fixed reference

point is a difficult task, due to the required capability of the scanning stage to be interchangeable with the intensity profile imaging system discussed before. Relative position determination is a more realistic approach, with the placement of multiple markers along the the scan line. The measured position of one of the markers would act as the reference point and the displacement to the other markers will be measured. With standard ASML marker dimensions of 150x80µm (x,y) being 10 mm apart on test wafers, a travel range in the scanning direction of 11 mm will make the measurement of two markers possible.

Alignment tolerances
Before performing alignment marker scans, the wafer sample must be aligned with the PIC. For a correct study of the PIC, the diffraction orders from the marker grating must be sufficiently captured by the capturing gratings. A deviation of the marker orientation from its nominal position will result in a shift of the spots with respect to their ideal positions on the capturing gratings. The tolerances of these wafer sample orientation deviations in several degrees of freedom are deduced from a maximum shift of the spots. The maximum shift is specified by the spot still being completely incident on the capturing grating, which is possible since the grating is slightly larger than the ideal spot. The spot size, or beam waist definition applied here is defined by an intensity of $1/e^2$ of the maximum at both sides of the spot. The directions of the reflected diffraction orders and thus the locations of the spots are calculated with the conical diffraction formulas, because of the oblique incidence angle on the marker grating from the emitting grating beam. Appendix B contains calculations of spot locations and dimensions over the diffracted beam trajectories for an arbitrary order m and their alteration with marker orientation deviations. The alignment tolerance requirements for the marker orientation relative to the PIC are listed in table 2.1. The translation in x-direction is the scanning direction. A deviation in the y-position of the marker does not shift the spot and its tolerance depends on the size of the marker grating.

Marker alignment tolerances

Rotation x	±6 mrad
Rotation y	±1.5 mrad
Rotation z	±20 mrad
Translation x	-
Translation y	-
Translation z	±70 µm

Table 2.1: Marker to PIC alignment tolerances around nominal position.

Repeatability
In the experimental setup the relative distance between two markers is measured. In order to reduce the complexity of this measurement, the absolute accuracy is not regarded as important and the repeatability, or precision, will be a priority. This means that if two markers that are in reality 10 mm apart from each other, show a measured relative distance of 9.99 mm, it is not a problem. The variation of this error, or repeatability, is important and the experimental setup aims for a repeatability of ±5 nm, assuming the PIC behaves like the Athena alignment sensor. This assumption is made because of the complexity in the coupling of free space beams to or from gratings, and the effect of for instance marker orientation deviations on coupling. FDTD simulations are expensive, so with respect to certain error sources, like the marker orientation deviations, the PIC alignment sensor will be treated as the Athena alignment sensor. It is also a means of benchmarking the new sensor with respect to a conventional one. The potential contributions to the position error are elaborated on in chapter 3.

Positioning
The effect of marker orientation deviations from the nominal position to the detected alignment signal must be analysed. Together with the need for alignment within the alignment tolerances (table 2.1), this implies that the wafer sample with markers must be adjustable in all degrees of freedom. The rotational degrees of freedom will require no more than 100 mrad of movement range. In the Z-direction, the ideal working distance between the wafer sample and the PIC sensor is designed at 10 mm, but it might be lowered to 5 mm in future PIC designs. A Z-movement range of around 15 mm will cover PIC design in the near future and provide manoeuvring freedom for the current design. Translation x is the scanning direction. Translation Y does not require a high resolution, because of the 40 µm spot on the 80 µm wide grating.

2.3. Signal insertion & extraction

With signal insertion the supply and coupling of both external optical and external electrical signals to the PIC is meant. Extraction covers the out-coupling of signals from the PIC. In section 1.2.3, the relevant PIC components for this signal insertion and extraction were indicated and the corresponding requirements will be presented in this section.

2.3.1. Optical

As mentioned, fiber-to-chip grating couplers are used in the sensor for the in-coupling of light from an external light source and the out-coupling of the on-chip alignment signal to an external photodetector. The fiber grating couplers on the PIC alignment sensor are designed for an angle of incidence (AoI) of 9°, defined with respect to the normal of the grating surface. Conventional experimental setups for PIC's couple light in or out via fibers with a flat end face that are brought in close proximitiy of the grating coupler, like in figure 2.2. However, this near-vertical coupling is not feasible in the novel experimental setup. The coupling process is complicated by the alignment marker scanning and IR imaging system for grating output characterization. They take up space above the PIC and obstructs fibers to be brought in from this direction, making it impossible for planar polished fibers to couple light in and out of the chip. This demands a different way of coupling. The requirements concerning this new method and properties related to optical coupling are described below.

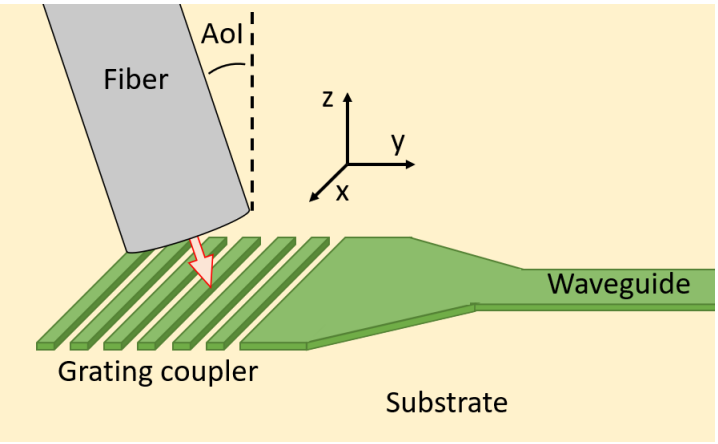

Figure 2.2: Schematic of near-vertical coupling between fiber and grating. Angle *AoI* is the angle of incidence corresponding to the grating design.

Polarization

Fiber grating couplers are designed for either TE or TM polarized light (parallel or orthogonal to grating lines respectively). The grating couplers on the PIC TE polarized light, but a future sensor design might require TM polarization, meaning the optical input signal must be adaptable in its linear polarization.

Wavelength

A tunable wavelength is needed around 1550 nm with ±15 nm to characterize the gratings, but also to find the ideal wavelength of the total sensor system. The possibility of typical fabrication errors to be present in the grating couplers might force us to change the wavelength within the mentioned range, optimizing the beam directions, but also increasing attenuation in on-chip components.

Power input

The lower limit of the required optical power input is related to the signal-to-noise ratio (SNR), which is a factor in the repeatability requirement of the scan. The influence of the SNR on the repeatability is discussed in chapter 3. The theoretical upper limit of the power in InP waveguides is 20 mW. Above this value, nonlinear effects will occur, which will influence the behaviour of the PIC.

Positioning
As specified earlier, there is a space restriction in the z-direction. For our PIC alignment sensor this space is 10 mm, but future designs might impose a design space of 5 mm. This restriction forces the fibers to be brought in horizontally between the sensor and marker sample, making the angle of incidence (AoI) impossible to achieve for standard planar polished fibers. The AoI for the fiber grating couplers in this particular PIC is 9°. In general, it can vary between 5° and 15° for different grating designs [10], so the fibers in our experimental setup require rotational positioning within this range. The tolerance on this AoI is rather loose, with the power transmission decreasing by half with a ±4 deg angle deviation. The z-distance between the fiber tip and the grating should be as low as possible and power transmission decreases by half with a distance of approximately 100 µm [14]. The alignment tolerances in x- and y-direction are tighter with half the transmission as a result of displacement. The grating couplers can be located anywhere on the IMOS wafer with a diameter of 75 mm, so the fibers must be able to travel over this range in x- and y-direction, while adhering to the other requirements.

2.3.2. Electrical
The system flow in figure 1.7 showed us that there are four active devices integrated on the chip. A laser diode, one photodetector and two switches. Electrical excitation or read out of these elements is done by making contact between electrical probes carrying signal/power from or to external equipment, and probe pads attached to both ends of every single element. The switches are actuated in both optical and complete electrical operation of the system, meaning four electrical probes are always in contact with the chip. When selecting the on-chip light source or on-chip photodetector, or both, either two or four extra electrical probes respectively are required. The specifications of these active components are listed in appendix A. The space restriction in z-direction also applies to the electrical probes.

2.4. Environment & operation
The experimental setup will be constructed in a clean room on an a stabilized optical table. The temperature inside is kept constant at 21°±2° and the air pressure is just greater than outside of it. The time it takes to first align the input and output fibers and then to align the scanning stage with sample, before being able to conduct measurements will be kept to 1 hour.

2.5. Requirements overview
The table below contains an overview of the most important requirements.

Requirements

Category	**Property**	**Requirement**
Grating output char.	Spatial resolution	< 2 µm
	Wavelength	1550
	Positioning	
	Z travel	> 12 mm
	Z accuracy	< ±25 µm
	X,Y travel	75 mm
Marker scan	Scan travel (x)	> 10 mm
	Alignment tolerances	*Table 5.1*
	Repeatability	< ±5 nm
Signal insertion & extraction	Polarization	Linear (TE,TM)
	Wavelength	1550
	Power input	5 – 20 mW
	AoI	5° – 15°
	X,Y travel	75 mm
Environment & operation	Temperature	21±2°C
	Installation time	1 hour

Table 2.2: Experimental setup requirements.

3

Alignment marker position measurement

The scanning motion of the wafer sample with the alignment markers over the PIC alignment sensor is the prime function of the experimental setup. In order to be able to reach the repeatability of 5 nm in marker position measurement stated in the requirements and understand the implications for the setup design, we must first comprehend the following two subjects: firstly, the relation between the alignment signal (shortly described in section 1.1) and the alignment mark position deduced from this signal, and secondly, the error sources in alignment mark position measurement. In sections 3.1 and 3.2 respectively, these subjects will be discussed.

3.1. Alignment signal fitting

In this section, the connection between the alignment signal coming from the alignment sensor and the position of an alignment mark is made. Earlier, the movement of the interference pattern over the reference grating in the Athena alignment sensor, as a result of the opposite phase shift of the two captured orders during the translation of the marker grating was described (see equation 1.1). The detector behind the reference grating captures a sinusoidal signal during this marker displacement at a constant velocity. Due to the absence of a correct model for the PIC, the working principle of Athena is extended to the PIC alignment sensor. The output power signal of the PIC P_{out} is proportional to the phase shifts induced by a marker grating translation according to equation 3.1:

$$P_{\text{out}} \propto \cos(2\Delta\Phi_m) \tag{3.1}$$

In reality, the alignment signal will resemble a function as in the graph below, with the marker translation on the X-axis and the intensity on the Y-axis. The signal has an envelope due to the finite length of the mark, leading to a variable overlap of the light incident on the mark, and a finite length of the spot. In the center position of the mark, overlap is maximal and the intensity the highest. The dc offset is caused mainly by the binary reference grating in the conventional alignment sensor, always permitting a part of the light from the interference pattern through. Considering the PIC alignment sensor, there is no reference grating, but there are other contributions to the dc offset, like a difference in transmission between the two capturing gratings and their paths to the beam combiner.

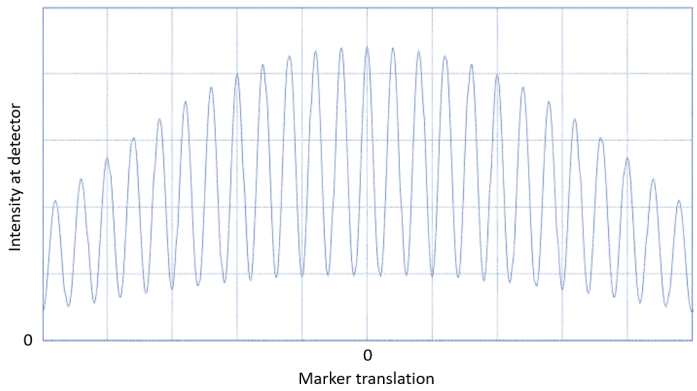

Figure 3.1: Alignment signal characteristics Athena alignment sensor. X: marker translation, Y: intensity at detector.

For now, we assume the grating to be infinite and include an unknown dc offset, amplitude and position offset. We obtain the following constant sinusoidal alignment signal $P(x)$ over the displacement x (I. Setija, private communication, December 2020):

$$P(x) = d + A\cos\Big(\frac{4\pi m}{\Lambda}(x - \Delta x)\Big) \tag{3.2}$$

where d is the dc offset, A the amplitude, Δx the position offset, m the diffraction order and Λ the marker grating pitch. This is the ideal alignment signal, but in practice, the signal can be distorted by a number of causes, some more harmful than others, which will be addressed in the next section. In order to retrieve the perceived position of an alignment mark from this non-perfect sinusoidal signal with all its deviations, it is fitted with a fitting function that is deduced from the ideal alignment signal 3.2:

$$f(x, a_1, a_2, a_3) = a_1 + a_2\cos\Big(\frac{4\pi m}{\Lambda}x\Big) + a_3\sin\Big(\frac{4\pi m}{\Lambda}x\Big) \tag{3.3}$$

from which the linear fit parameters a_1, a_2 and a_3 are retrieved with the least-squares method. The unknown d, A and perceived marker position, or position offset, Δx from the ideal alignment signal (equation 3.2) can now be calculated by equating the ideal alignment signal with the fitting function:

$$d = a_1 \qquad A = \sqrt{a_2^2 + a_3^2} \qquad \Delta x = \frac{\Lambda}{4\pi m}\tan^{-1}\Big(\frac{a_3}{a_2}\Big) \tag{3.4}$$

Through this linear regression method, certain error sources concerning the setup can be distinguished, in order to make correct design choices.

3.2. Error sources

The method for determining the marker position Δx is now known. The most important influences on this position measurement are demonstrated in this section. They are separated in two categories:

1. Signal quality
2. Marker orientation deviations

The first subsection is about the sources that affect the signal quality and thus the marker position measurement through the fitting procedure. These originate from the displacement sensor that is integrated with the scanning stage, and the signal processing equipment. Marker orientation deviations, described in the second subsection, have an impact on the marker position measurement via the working principle of the alignment sensor.

3.2.1. Signal quality and processing

The main sources affecting the signal quality are the integrated displacement sensor (measuring the displacement of the scanning stage) and the signal processing equipment (photodetector, amplifier, etc.). The displacement sensor properties, like resolution and error characteristics, manipulate the fit that is performed on the alignment signal and might introduce problems in the repeatability of the measurement. These sensor properties are dictated by the displacement sensor working principle. Other factors impacting the alignment signal fit are concerned with the signal processing equipment. Properties like the signal-to-noise ratio and bandwidth of for instance the light source and photodetector to be chosen, will influence both the repeatability of the measurement and the scanning velocity we can achieve. In chapter 5 the subject will be addressed again, where the content of this section will support the choice of a displacement sensor and the surrounding equipment for the experimental setup.

The resolution of the displacement sensor could be considered as the minimum sampling distance of the alignment signal. However, the signal processing equipment will have a maximum bandwidth. Depending on the scanning velocity that will be applied, either this processing equipment bandwidth or the sensor resolution is limiting for the sampling distance of the alignment signal. The minimum sampling distance required depends on the frequency of the alignment signal (equation 3.2). The standard ASML alignment marker has a period Λ of 16 µm and the PIC alignment sensor uses the 5^{th} diffraction orders, resulting in an alignment signal period of $\frac{\Lambda}{2*m}$ = 1.6µm. The Nyquist sampling criterion tells us that in order to retrieve

the correct frequency of the signal f_{signal}, a sampling frequency f_{sample} two times larger than the signal frequency is necessary. A Rule of thumb for sufficient amplitude measurement is $f_{sample} > f_{signal} * 10$, resulting in a required sampling distance d_{sample} below 0.16 µm. The maximum scanning velocity v depends on the maximum bandwidth b of the processing equipment according to $v = d_{sample} * b$. The velocity can be decreased, consequently decreasing the sampling distance, to a certain point where the resolution instead of the bandwidth is limiting to the sampling distance.

A next property of the displacement sensor in the scanning stage that has an important influence on the signal fitting procedure, is the error in its perceived displacement. In particular, the nature of this error. An error in the communicated displacement of the wafer sample translates to an incorrect intensity for that position, which might have an impact on the deduced alignment marker position, depending on the characteristic of the error. The most substantial characteristics in displacement errors and their effects on marker position determination will be covered in the remainder of this section. These include random errors and periodic errors. Since the alignment signal is fitted with a sinusoidal function via the least squares method, some errors are filtered out and have a minimal impact on the deduced alignment marker position. Random error errors are mostly filtered out, provided that they remain small and the sampling distance is high enough. To get a feeling for what this means for the design, an example is provided, in which a typical motorized linear stage without a displacement sensor is used, having a random displacement error of ±0.25 µm. The sampling distance is 0.1 µm. The graph below (figure 3.2) shows the sampled alignment signal with the linear stage described, in blue. The red line represents the fitted function to these data points, resulting from the linear regression method described in section 3.1. The marker position uncertainty resulting from this positioning stage displacement error is around ±15 nm. Since the repeatability requirement reads ±5 nm and this is not the only error source, the typical stage without sensor used in this example will not be sufficient. A linear stage including an integrated high precision displacement sensor is needed, which is elaborated on in section 5.1.2. The same effect could be demonstrated with noise sources in the signal processing equipment. The total signal-to-noise ratio in the alignment signal is an accumulation of noise sources in all separate components and it must be high enough in combination with the sampling distance, to adhere to the repeatability requirements.

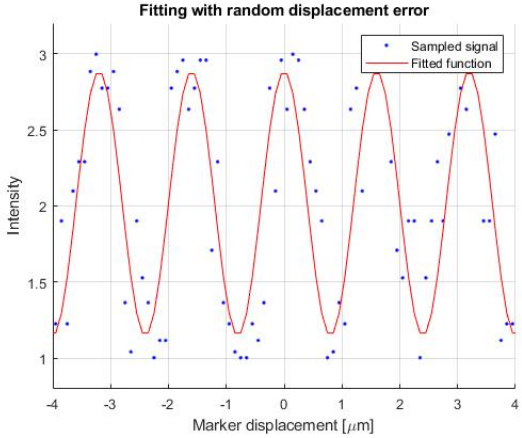

Figure 3.2: Function (red) fitted to sampled alignment signal with random error (blue). Resolution is 0.1 µm, random error amplitude is 0.25 µm

If periodic errors are present in the reported displacement, depends on the type of displacement sensors. Periodic errors often arise in displacement sensors with scales, such as optical encoders. The sensor deduces displacement by counting the markings on a scale it passes, resulting in the periodicity of an error, proportional to the scale resolution. Since the alignment signal is sinusoidal, certain error frequencies will resonate with this signal. A slight position deviation between scans can change the phase difference between alignment signal and periodic error signal, meaning that this resonance is not very repeatable. To assess what periodic sensor displacement errors have an effect, again an ideal alignment signal is sampled, now with the following error ϵ:

$$s_i = x_i + \epsilon_i = x_i + B\cos(\frac{2\pi}{P}x_i(i)) + B\sin(\frac{2\pi}{P}x_i(i)) \tag{3.5}$$

where s_i are incorrect sample locations, B is an error amplitude component and P is the period of the error. In the graph of figure 3.3, marker position error is displayed over the period P of the sensor displacement error after fitting. An amplitude B of 200 nm was chosen to clearly demonstrate that over this interval of frequencies, three peaks in the error are obvious, one higher than the other. They correspond to periods 0.8, 1.6 and 2.4, all positive integer multiples of half the alignment signal period. It reveals that harmonics play a key role in this periodic error source. Periodic errors that resonate at the alignment signal harmonics, should be avoided in the integrated displacement sensor. This error source is addressed again in section 5.1.2, where the choice of displacement sensor is expanded on.

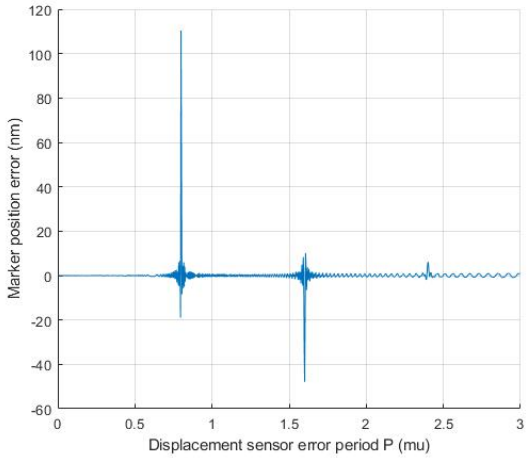

Figure 3.3: Marker position error over the period of the displacement sensor error in equation 3.5

3.2.2. Marker orientation deviations

The second category of error contributions revolves around the orientation of the alignment mark grating relative to the alignment sensor. A deviation of the marker orientation from the nominal position alters the direction of the diffraction orders reflected from the marker, as described in B. As a result, the path lengths from marker to capturing grating will change, as well as the incoming wavefront on the capturing gratings. In the previous chapters, the complexity of this coupling process was elaborated on and the treatment of the PIC alignment sensor as the Athena alignment sensor was mentioned. In this section, the effects of orientation deviations on the alignment signal are demonstrated.

The working principle of the Athena alignment sensor was explained in chapter 1. To illustrate the effect of marker orientation on the alignment signal, the focus is on the interference pattern focused on the reference grating. The individual degrees of freedom of the marker are discussed prior to combinations of them, which actually result in an error of the deduced marker position. All of the phenomena are assumed to be dealing with small rotations and are thus reduced to small-angle approximations. Important to point out, is that in a 4F lens system, the magnification is equal to one and that a translation or rotation of the object leads to a translation or rotation of the image, in which the marker grating and interference pattern can be considered as the object and image respectively. A translation in the scanning direction X of the marker leads to an alteration in X of the interference pattern over the reference grating, stemming from equations 1.1 and 3.1 in previous chapters. It is mentioned on behalf of thoroughness, but this displacement is of course not the source of an error. A translation of the marker in Y-direction (coordinate system of figure 3.4), along its grating lines will not affect the interference pattern position. It will influence the intensity of the signal since the marker has finite dimensions. If the marker translates in the Z-direction, the interference pattern translates an equal distance in the Z-direction, which is depicted in figure 3.4. The green ray paths are those of the system with the marker in nominal position. The orange ray paths are the result of a translation ΔZ of the alignment mark. This defocus relates to the signal at the detector with a decrease in amplitude because of the decreased contrast in the interference pattern before or after focus, which is apparent from the blow up in the figure of the region around the reference grating. It does not directly introduce an error in marker position measurement, because the pattern does not drift in X from the nominal X-position.

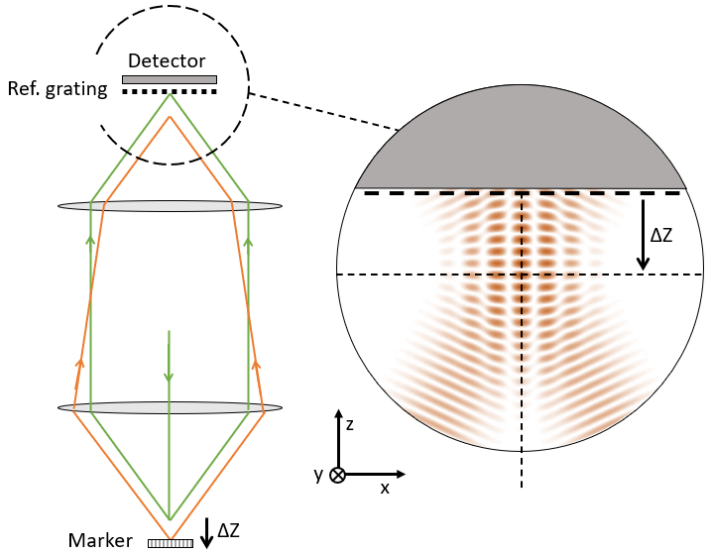

Figure 3.4: Translation in Z-direction of interference pattern, due to a translation in Z-direction of alignment mark w.r.t. nominal position (defocus).

Rotations do not affect marker position measurement independently. A marker rotation around its X-axis, leads to an opposite rotation of the interference pattern around its X-axis. The pattern does not shift in the X-direction, meaning that there is no position error. However, the tip of the pattern plane causes defocus, positive and/or negative depending on the axis of rotation. As stated before, a defocus only introduces a reduction of the amplitude of the signal. The result of a marker y-axis rotation β is depicted in figure 3.5. The beam from the light source is now incident under an angle. We do not make use of the equations for conical diffraction, but take the small-angle approximation approach and treat the alteration of the reflection angle of the diffraction orders as if they reflect of a mirror instead of an alignment mark, with extra angle of 2β. Thus, at the reference grating, the interference pattern also rotates with an angle 2β around the y-axis in focus. There is no shift in X of the pattern and because of the small angles, the period of the projection of the pattern in the plane of reference grating can be considered equal to that of reference grating.

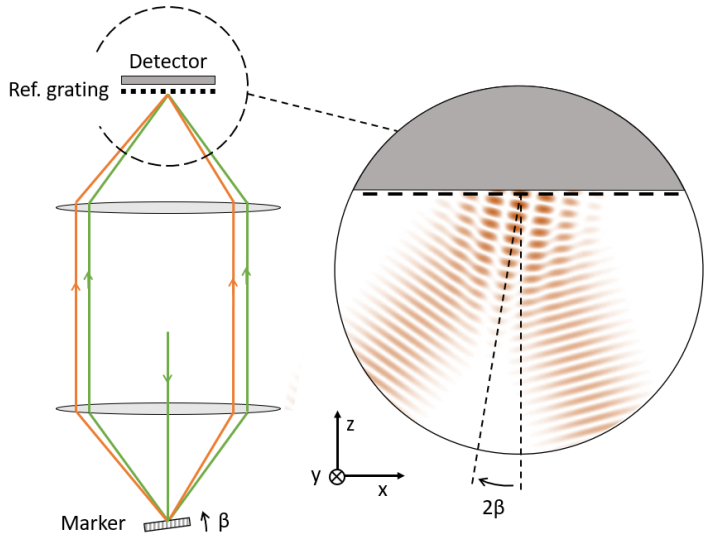

Figure 3.5: Rotation 2β around the y-axis of the interference pattern, due a rotation β around y-axis of alignment mark w.r.t. nominal position.

A rotation of the marker around the z-axis results in an equal rotation of the interference pattern. Figure 3.6 shows a schematic top view of the reference grating in black, with the interference pattern in nominal position in green and in rotated position in orange. The nominal pattern maxima are in the center of the

grating slots, so the alignment signal will be at a maximum as well. After rotation γ, the pattern maxima still coincide with the center of the grating (dotted line) and they are still distributed symmetrically over the slots, meaning that the alignment signal will remain at a maximum for this position. Consequently, there is no X position error, only a drop in amplitude of the alignment signal, since the maxima/minima are stretched out over the grating slots during a scan.

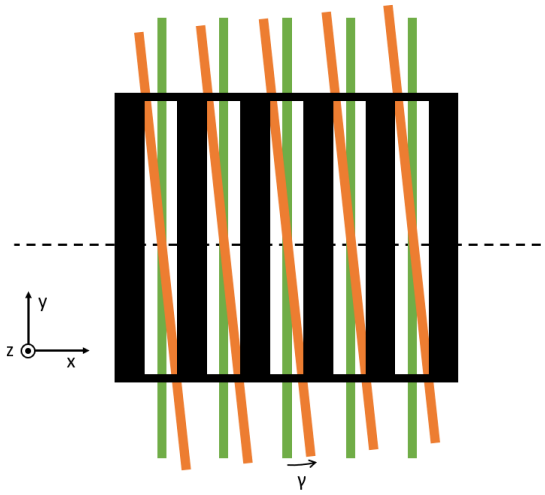

Figure 3.6: Rotation γ around the Z-axis of the interference pattern, due to a rotation γ around the Z-axis of the alignment mark w.r.t. nominal position.

All the degrees of freedom have been covered and it was shown that they do not introduce a position error individually. However, there are two combinations of them that do. The first case is a combination of a defocus ΔZ and a rotation around the y-axis β. Figure 3.7 displays the effect. There is a shift ΔX, an error, over the reference grating that can be assigned to the marker deviations as follows:

$$\Delta X = 2\beta\Delta Z \tag{3.6}$$

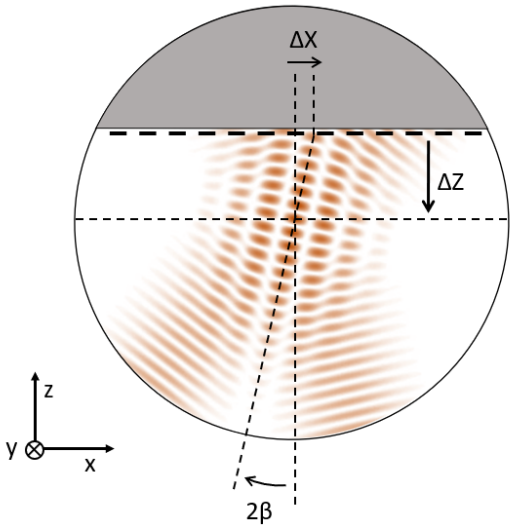

Figure 3.7: Marker position measurement error ΔX, as a result of a combined marker defocus ΔZ and rotation β.

The second combination of marker orientation deviations consists of a rotation γ around the z-axis and a translation in the Y-direction (ΔY). In figure 3.8 a similar schematic to the one in figure 3.6 visualises the influence on the perceived marker position. The altered interference pattern (orange) has lost its position of maximum detector exposure through the reference grating, in contrast to the pattern in nominal position.

The altered pattern would have to translate in the negative X-direction for this maximum exposure. This error ΔX relates to the marker orientation deviations γ and ΔY as follows:

$$\Delta X = \gamma \Delta Y \tag{3.7}$$

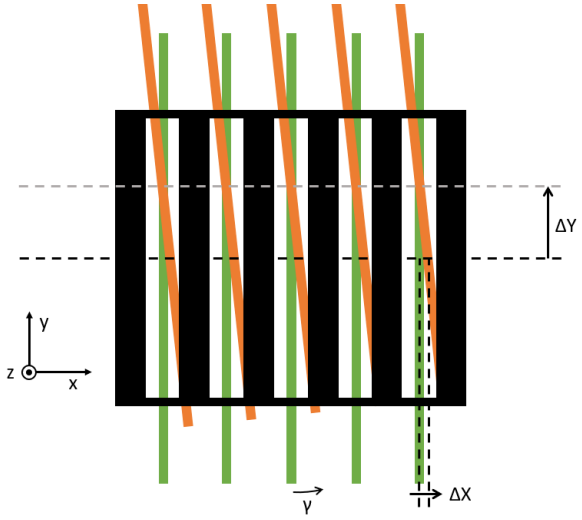

Figure 3.8: Marker position measurement error ΔX, as a result of a combined marker Y-translation ΔY and rotation γ.

4
Concept creation

In order to convert the requirements stated in chapter 2 to a detailed design of the experimental setup, it is essential to explore the possibilities surrounding certain subsystems and subjects. In this chapter, for some subjects, the different concepts are explained and evaluated using adequate considerations and criteria. The possibilities for the following subjects will be discussed and evaluated:

1. Beam profiling
2. Fiber-to-chip coupling
3. Setup configuration

From the evaluations of the concepts, a justified choice of direction can be made. This will be a good base for the detailed design of the setup, featured in chapter 5, where the selected concepts are further developed.

4.1. Beam profiling

The emitting and capturing gratings of the PIC are designed to respectively produce and receive ideal Gaussian intensity profiles with their focal point at z=10mm from the chip, on the alignment marker. In this section, we will discuss the (near-)Gaussian beam properties we are interested in, conceptualize the different methods to measure them and compare these methods by means of the requirements and other desirable criteria.

The measurement of 2D intensity profiles of a light beam, is referred to as beam profiling. It is a common practice in the laser industry, where several techniques can be implemented by the user to evaluate a laser. The most straightforward property of a Gaussian beam is its diameter, which is usually defined by the two points where the optical intensity drops to $1/e^2$ with respect to the maximum. More information can be retrieved from the measurement of the spatial or 2D intensity profile at a certain location. The distribution of the electric field can be determined with a certain accuracy, depending on the measurement method. As stated in chapter 2, the spatial intensity profile at the focal point is an important property to measure and a minimal starting point, in order to provide insight in the interaction between the beam and the marker grating and to evaluate the grating design choices. Capturing spatial intensity profiles at different distances from a grating coupler, will allow for mapping the beam in 3 dimensions over a certain range and thus a more thorough analysis of that grating. A next step could be phase retrieval, and although the first measurements conducted with the infrared imaging system on PIC's do not aim at phase retrieval, it might be applied with future PIC designs. There are two primary electronic techniques implemented in spatial intensity profile measurement with a sufficient resolution: mechanical scanning profiling and camera-based profiling. They will be elaborated on, so that they can be compared for the purpose of the experimental setup. The requirements are leading when making a choice between the two afterwards, also keeping factors like complexity and cost in mind.

Mechanical scanning profiler

Scanning slit, knife-edge or pinhole beam profilers are the mechanical scanning devices that are used most frequently. Their working principle is visualized in figure 4.1, with a scanning slit profiler. By mechanically moving an aperture (slit or pinhole) or a knife-edge through a beam, orthogonal to the direction of propagation, the amount of light passing through becomes a function of the position of the aperture or knife-edge. The light passing through is captured by a detector and its intensity signal is related to that position. In almost all commercially available mechanical profilers, the movement is achieved by rotating a drum in which

the aperture or knife-edge is present. The disadvantage of scanners is that they do not image or measure, but calculate the spatial intensity profile. With a scan in one direction, only the intensity profile in this one dimension measured and the reconstruction of the entire 2D profile is dependent on assumptions. Most mechanical profilers perform scans in multiple directions, by adding apertures in different orientations to the rotating drum, like in the slit profiler of figure 4.1, and/or by rotating the drum itself around the beam propagation axis. This way the spatial intensity profile can be reconstructed with more detail, through algorithms developed for tomography. However, conducting scans in multiple directions is time consuming, and real time beam profiling is not possible. The spatial resolution of mechanical profilers depends on the readout speed of the detector and the consistency of the aperture velocity. A higher scan rate will result in a lower spatial resolution if the max readout speed of the detector is approached. If the velocity of the aperture has a certain variability, it introduces an uncertainty in the resolution. Both aperture and knife-edge scanners can reach very low resolutions down to 0.1 µm, but are only compatible with pulsed light beams in the kilohertz range [16].

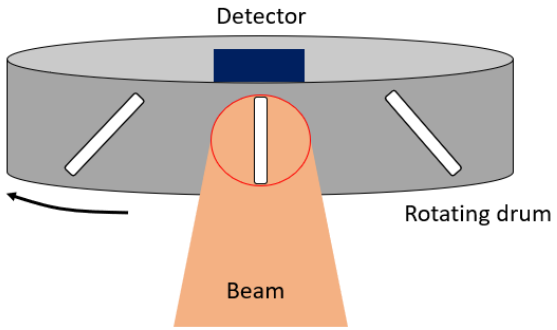

Figure 4.1: Schematic of scanning slit beam profiler.

Camera-based profiler

The two-dimensional array of rectangular pixels a camera consists of, can image the spatial intensity distribution of the focal spot of a beam. Contrary to the mechanical scanning techniques, the profile is measured and not calculated. As a result, camera-based beam profilers are capable of imaging beams more complex than near-Gaussian beams. The pixel size, or more specific the spacing between the centers of the pixels, determines the resolution of the camera. A rule of thumb for the robust measurement of a relatively complicated near-Gaussian beam is that the diameter of the beam should cover at least 20 pixels [17]. The pixel sizes of modern, regular CCD and CMOS beam profiling cameras can be as small as 4 µm, meaning that beam diameters may not be lower than 70 µm. For smaller beam diameters, like the 40 µm beams of the PIC alignment sensor gratings, the camera must be accompanied by a magnifying system, such as a microscopic objective. CCD and CMOS cameras are only sensitive in the visible spectrum and part of the near-infrared spectrum (NIR) from 400 nm to 1000 nm. If beams in the short-wave infrared region (SWIR), between 900 nm to 1700 nm are to be imaged, there are two main commercial and compact solutions. Firstly, a phosphor-coating could be applied to the light-receiving surface. The energy a photon carries is inversely proportional to the wavelength. According to Stokes shift [18], the energy it takes to excite an electron is larger than the energy it emits when it returns to its normal state, so the wavelength of the radiation must be longer than the absorbed wavelength. However, so-called 'anti-stokes' phosphors have the ability to absorb two or three photons of a wavelength in the infrared region and combine their energy to emit a photon in the visible or NIR region. The sensitive spectral bandwidths for which these phosphor-coated cameras can be designed are rather non-uniform and small with approximately 100 nm [19]. A larger bandwidth can be provided by the second option, InGaAs cameras, which cover the entire SWIR region fairly consistently. Their array is formed by two indium phosphide (InP) layers enclosing an indium gallium arsenide (InGaAs) adsorption layer. They are bonded to a CMOS readout integrated circuit [20]. InGaAs cameras have some limitations, of which the most important one is a high susceptibility to dark current. In order to achieve a good signal-to-noise ratio by minimizing the dark current, the camera must be cooled significantly. For low power applications, thermoelectric cooling is commonly used and for high light intensities, cameras also utilize liquid cooling. Another disadvantage is the pixel size, which is larger with respect to visible light CCD and CMOS sensors, with dimensions of around 20x20 µm. The use of magnifying optics for the spatial intensity profiling of beams becomes inevitable. A

consideration for all camera types is the irradiance of the beam. When imaging a high-power laser, components for sampling and attenuation are needed to avoid saturation of the camera pixels. In the case of the PIC alignment sensor power is low and attenuation is not needed.

Concept selection

Conceptually, there are three possible solutions to image spatial intensity profiles: a mechanical scanning profiler and two camera-based profiler, namely a phosphor-coated camera profiler and an InGaAs camera profiler. All concepts are regarded as off-the-shelf systems, including potential necessary surrounding equipment. Now, we can compare them against the requirements and a select beam profiling principle that will be further developed for the detailed setup design. The spatial resolution of mechanical scanning profilers is high enough and because of that, they do not demand for heavy and space consuming magnifying optical components. This option would benefit the complexity of the setup, since the space around the device under test will be limited by all other subsystems involved. Mechanical scanning profilers are also relatively inexpensive, compared to InGaAs cameras. However, a shortcoming of mechanical profilers is that the profile they image is a partly calculated, reconstructed version of the real beam. This approximation is sufficient when the beam is relatively circularly symmetric and near-Gaussian, or when a detailed measurement is not necessary. But when the intensity profile to be imaged becomes more complex, the mechanical scanning methods fall short. As described in section 2.1, the outputs of the grating couplers will most likely not resemble perfect Gaussian profiles, due to design limitations and fabrication tolerances. This uncertainty of the output beam combined with the wish to optimally analyze the grating couplers by means of their emitted light, has resulted in rejecting the mechanical scanning profilers as a concept. The bulky options remain, the camera-based profilers.

Beside the exact profile measurement, there is another argument for a camera-based profiler. In order to align the wafer sample containing the alignment markers with respect to the PIC alignment sensor within the tolerances stated in the requirements, a reliable, relatively quick and space efficient method must be found. If the PIC under test is functional (which is determined by the IR imaging system), the wafer sample could be aligned by trial and error. It would involve the tuning of every degree of freedom one by one in a highly iterative process, until the beam from the emitting grating is not only incident on the marker grating, but the diffraction orders are also incident on the capturing gratings. This would be a time consuming and fairly arbitrary method. Complex microscopy equipment and specifically designed features in both chips (PIC and wafer sample), often used in alignment for wafer bonding [21], could be used to correctly and efficiently align the components. For the experimental setup, a simpler approach was must be found. The choice for a camera-based profiler with objective, will aid in the development of a cost effective alignment strategy. By using properties like focal depth, focal distance and the positioning accuracies of such an imaging system, the PIC will be referenced to the alignment marks in certain degrees of freedom with some uncertainty. This alignment strategy is described in section 5.2.

Now the selection between the two camera types has to be substantiated. Although the pixel size of phosphor-coated cameras is smaller than that of InGaAs cameras (4 µm to 20 µm respectively), it is still not enough to prevent the implementation of magnifying optical equipment. An advantage of phosphor-coated over InGaAs is that it is significantly less costly, the former being in the same price range as mechanical scanning profilers and the latter being in a range a factor 10 higher. The main argument that declares the InGaAs camera solution superior to the phosphor-coated camera for our purposes is related to the behavior of the spectral bandwidth of both cameras. The uncertainties in grating design might alter the ideal working wavelength for a particular PIC to focus and receive sufficient light beams, meaning at the right location on/from the alignment mark and of sufficient intensity. Thus, one of the characteristics of the PIC grating couplers that is to be investigated, is their response to changes in wavelength over a ± 15 nm range. If the detector responsivity is highly variable over this range, which is the case for phosphor-coated detectors, it will be more difficult to draw conclusions from wavelength dependency measurements of the output beam of a grating coupler. The InGaAs camera-based profiler presents itself as the preferred option as it adds the most experimental capability and versatility to the setup. The fact that an InGaAs camera has been located among the assets of ASML's lab equipment, removes cost related issues. The detailed design of the infrared imaging system including an InGaAs camera is unfolded in chapter 5.

4.2. Fiber-to-chip coupling

Aside from diffraction-based coupling, with the use of fibers and grating couplers, there are other methods to couple light into or out of a photonic integrated circuit. On the PIC alignment sensor only grating couplers are implemented, since they are relatively uncomplicated to fabricate and align to the external light carrying medium. On top of that, grating couplers are accessible without having to dice the wafer they were fabricated on, a considerable advantage when conducting experiments. The experimental setup aims to perform experiments on early stage PIC designs and is thus expected to only handle PIC's with fiber grating couplers, now and in the future. As mentioned in chapter 2, the normal near-vertical fiber coupling method is not an option. Nevertheless, the use of fibers is indisputable. Their simplicity, coupling efficiency with the gratings and small dimensions in the potentially crowded space above and around the chip are valuable. As a result, the possible solutions will all regard fiber modifications that allow the fiber to come in (near-)horizontally and redirect the light to the grating coupler near-vertically, which we define as quasi-planar coupling. The criteria that are important to compare these different concepts are the coupling efficiency, cost and stability, where cost manifests itself in manufacturability. There are several single-mode fiber modification methods considered for quasi-planar coupling, in two categories:

1. Angle polished fiber
   (a) Single angle polished fiber
   (b) Double angle polished fiber
2. Lensed fiber
   (a) Ball-lensed fiber
   (b) GRIN-lensed fiber
   (c) cylindrical polished fiber

Before addressing the conceptual fiber modifications and selecting between them, a qualitative introduction to fiber optics is given, in order to understand the choices made in fiber design modifications and their consequences on performance with grating couplers.

Fiber optics

Fibers are essentially waveguides, with a circular cross-section, consisting of a core and a surrounding cladding. With respect to figure 1.3, the refractive indices become $n_{\text{clad}} = n_{\text{sup}} = n_{\text{sub}}$ and $n_{\text{core}} = n_1$. A single-mode fiber (SMF) supports only the fundamental transverse (TE) mode. Figure 4.2 shows the dimensions of the most commonly used standard SMF type at a 1550 nm wavelength, the SMF-28. The intensity profile of the fundamental TE mode is depicted in blue. Its mode field diameter (MFD) of 10.4 µm extends over the core diameter of 8.2 µm into the cladding and is determined by the radial points where the intensity drops to $1/e^2$ with respect to the maximum. This intensity profile resembles a Gaussian profile [22]. The beam divergence of the light originating at the end-face of the fiber is an important property for coupling methods. An approximation of the far-field divergence angle α often used for flat end-faced single-mode fibers is given by:

$$\alpha = \sin^{-1}(NA/n_{\text{air}}) = \sin^{-1}\left(\sqrt{{n_{\text{core}}}^2 - {n_{\text{cladding}}}^2}/n_{\text{air}}\right) \tag{4.1}$$

The numerical aperture $NA = ({n_{\text{core}}}^2 - {n_{\text{cladding}}}^2)^{1/2}$ does not depend on fiber dimensions. For our fiber to grating coupling purposes, this approximation is not particularly useful, since the distance between fiber and grating is in the near-field below the Rayleigh length (eq. C.2). A Gaussian beam model can however accurately describe the beam divergence of light leaving a SMF in near- and far-field [23]. The initial beam diameter $2w_0$ ($1/e^2$ of maximum) is set to the MFD of the fiber at its end facet and the spot width as a function of the propagation distance z becomes:

$$w(z) = w_0\sqrt{1 + \left(\frac{z}{z_R}\right)^2} \tag{4.2}$$

With the Rayleigh length:

$$z_R = \frac{\pi w_0^2 n}{\lambda_0} \tag{4.3}$$

Where n is the index of the propagation medium and λ_0 is the wavelength in vacuum. The divergence in the near-field is very small, which is of course advantageous in uniform grating-coupling, where the distance between fiber and coupler is often in the near-field.

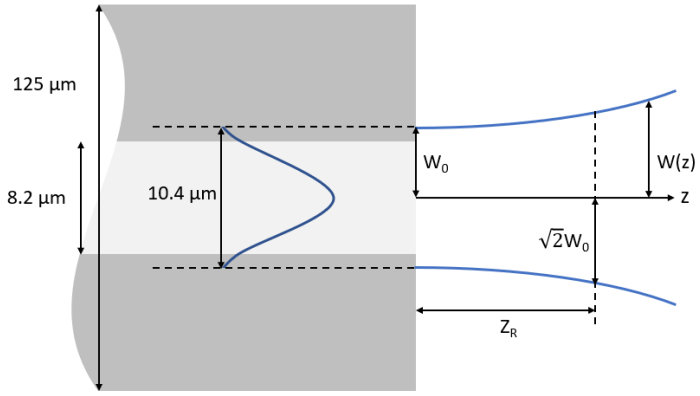

Figure 4.2: Standard single-mode fiber and output Gaussian beam dimensions.

Angle polished fiber

Angle polished fiber is the least complex quasi-planar coupling method in terms of manufacturability. A schematic of its working principle is depicted in figure 4.3a. Light from the fiber core is reflected by the angle polished end-face in the direction of the grating with the correct AoI. For a grating coupler designed for an AoI (θ_{AoI}) of 10°, the fiber polished angle θ_{fiber} would become 40°:

$$\theta_{\text{fiber}} = \frac{90 - \theta_{\text{AoI}}}{2} \tag{4.4}$$

A reflective coating on the end-facet of the fiber is not necessary, because of the total internal reflection angle ϕ relation:

$$\phi = \arcsin\left(\frac{n_{\text{air}}}{n_{\text{core}}}\right) = \arcsin\left(\frac{1.00}{1.45}\right) = 43.6 < (90 - \theta_{\text{fiber}}) \tag{4.5}$$

Refraction at the cladding to air interface alters the output angle to the grating, from 10° to almost 15°, shown in figure 4.3a. It also increases the divergence of the beam in this direction, which is expanded on later. The changed output angle can be accounted for by adjusting the polishing angle, but the increase in divergence will remain. In applications where fibers are assigned to a particular grating permanently, an epoxy bonding layer with a refractive index equal to that of the cladding can be used between the cladding and the grating. In that case, the divergence in the X-direction will not increase and the fiber is less susceptible to drift and stability issues after one-time alignment [24]. In an experimental setup intended to do relatively quick measurements on multiple devices on the same and other chips, bonding is not favorable.

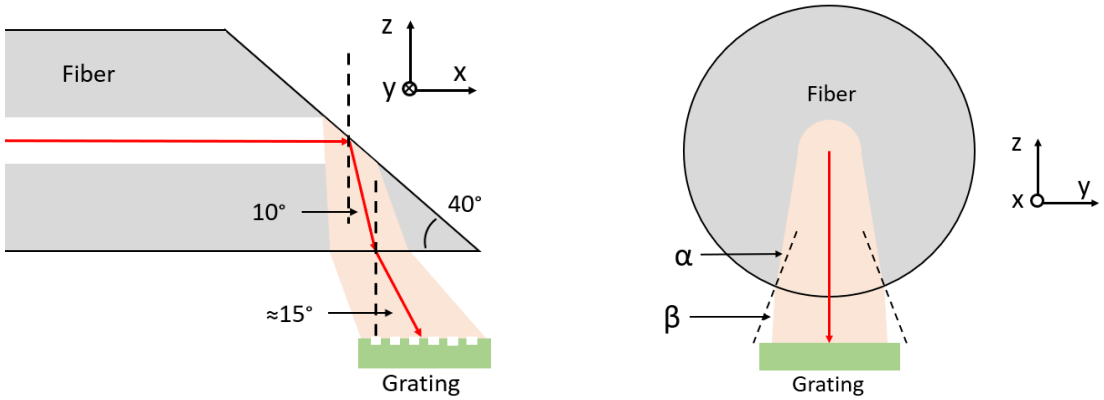

(a) (b)

Figure 4.3: Schematic of angle polished fiber. Refraction at the cladding to air interface must be accounted for. Beam divergence increased in X-direction and reduced in Y-direction.

In appendix C a prediction of the output beam of an angle polished fiber is made and for a complete understanding of the light beam behaviour, the reader is referred to it. The essence is demonstrated in figures 4.3a and 4.3b. Just like the output of a flat end-face fiber, the output of an angle polished fiber reaching the grating coupler is expected to have a Gaussian profile according to the fiber optics equations discussed. However, the profile along the propagation direction through air will be rotationally asymmetric. Also, the beam will have traveled a greater distance, through the cladding, compared to flat end-face fiber coupling. The effect of refraction at the cladding to air interface on the Y-divergence of the beam is visualized in the schematic of 4.3b. With the dotted lines being the normals at the interface, angle α is smaller than angle β and the divergence over the Y-axis in air is thus smaller than in the cladding, according to Snell's law. With the method described in appendix C, we can compare the parameters of the spot on the grating coupler created by the angle polished fiber to the spot of normal flat end-face fiber. For this, we assume both fibers can be brought as close to a 15 µm × 15 µm grating coupler as 20 µm. For the flat end face fiber, the spot diameter is 11.3 µm and the full angle divergence is 3.7°. For angle polished fiber, the diameter in x-direction is 15.9 µm and in y-direction 13.8 µm, with a full angle divergence of 7.0° and 1.5° respectively. The angle polished fiber spot will be partly outside the grating coupler and have a slightly higher net divergence.

An accurate evaluation of the actual coupling efficiency is difficult. The physics are complicated and numerical simulations are expensive. However, an estimation of the performance of angle polished fiber coupling compared to near-vertical coupling can be made using the literature concerned with it. Research conducted with angle polished fiber and particular grating couplers like the ones used on the PIC alignment sensor has not been found. A comparison with equal gratings between near-vertical coupling and quasi-planar coupling must be made. Zhang et al. [25] with near-vertical coupling, and Li et al. [26] with quasi-planar coupling, used the same non-uniform grating coupler and provide us with a coupling loss comparison of 1.5 dB and 3.25 dB respectively. This equals a transmission difference of 33% between the two. Their grating dimensions are 13 µm × 10 µm, so the Gaussian beam with $2w_0$ set to 10.4 µm at the polished reflective surface will be larger than the grating by a few micrometers after propagation through the cladding (C.1). It is likely that this mismatch in spot and grating size provides a bigger contribution to the reduced coupling efficiency, than the slightly overall increased divergence angle addressed before, considering that a 4° AoI deviation of light will cause a relative transmission loss of 50% [14]. The fiber-to-chip grating couplers used in the PIC alignment sensor have dimensions of 15 µm × 15 µm and are thus expected to have a smaller reduction in transmission when transferring to angle polished fiber coupling, in comparison to the 33% loss deduced from literature. Normal near-vertical coupling is assumed to have a coupling efficiency of 28% on the fiber grating couplers of the PIC alignment sensor (J. de Graaf, private communication, December 2020 [13]) . A reduction of 33% with angle polished fiber would result in a coupling efficiency that is high enough, if taken into account in the choice of laser source power and signal processing equipment.

There is a solution shortening the traveled path between the core and the grating, resulting in a smaller spot size and a decrease in divergence. Figure 4.4 shows a double angle polished fiber described in a patent

[27]. There is no record of the concept being realized and applied in fiber-to-grating coupling. The transmission would theoretically be equal to or better than near-vertical coupling, since the distance from core to grating can be made even shorter. It does however introduce manufacturing complexities. The location and orientation of a second polished face are constrained to that of the first polished face, which can not be done correctly by standard fiber polishing machines.

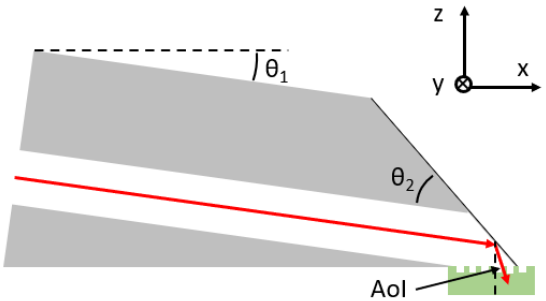

Figure 4.4: Schematic of double polished fiber [27]. AoI = $2(45-\theta_2)-\theta_1$.

Lensed fiber

Fibers can combined with optical components to manipulate the in- or outcoming beam. Figure 4.5 shows two concepts that use a type of lens attachment: a gradient-index (GRIN) lens attachment and a ball-lensed fiber attachment. Both concepts also consist of a polished angle, simply because it is the superior method to direct light downward. The GRIN lens extension of the fiber focuses the beam along the original propagation direction and the angle polished lens surface redirects the beam downward according to total internal reflection, just as was the case with the angle polished fibers. The ball-lensed fiber attachment focuses the beam after the reflection downward, instead of before [28]. The working distance and NA of both concepts can be modified by extending the coreless attachment and changing the lens properties. These focusing or collimating lens attachments are not yet applied to fiber-to-grating coupling, but they could be advantageous. Just as is the case with the double angle polished fiber concept, lensed fibers allow the grating coupler to be illuminated with a plane wavefront, increasing the coupling efficiency. The choice of spot size at focus lightly influences the alignment tolerances of the fiber to the grating. With a small spot size, the fiber will have looser tolerances in the plane of the grating, but also a higher divergence, thus a tighter tolerance in the direction normal to the grating.

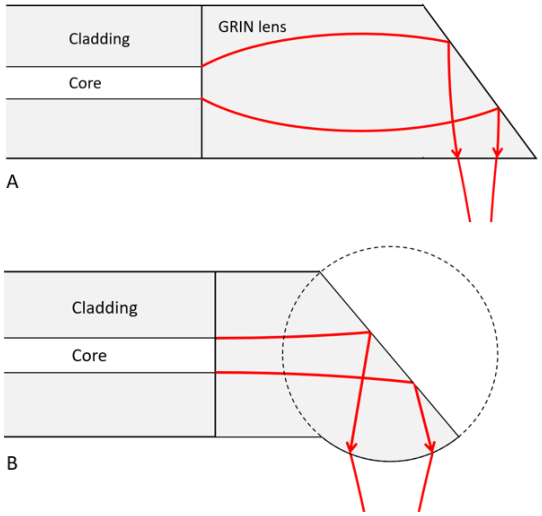

Figure 4.5: Schematic of redirecting lensed fibers. A: GRIN lens fiber attachment. B: Ball-lensed fiber attachment.

A last concept that is categorized under the lensed fibers, but is very similar to the single angle polished fiber discussed before, is the cylindrical polished fiber depicted in figure 4.6. The polished surface acts as a focusing mirror for the beam in X-direction. The principle of the schematic in figure 4.3b also holds here, meaning that this concept restrains the divergence in both the X- and Y-direction. Again, standard fiber polishing machines are not capable of realizing this concept (Te Lintelo B.V., private communication, April 2021), greatly affecting the cost of manufacturing.

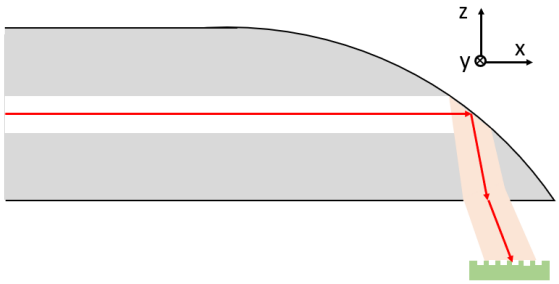

Figure 4.6: Schematic of cylindrical polished fiber.

Concept selection

Assessing the quasi-planar coupling methods is mainly about coupling efficiency and complexity, since they do not differ much in their stability and handling during alignment. If the method is efficient enough for the photodetector at the end of the system to capture enough light, the manufacturing complexity, thus cost and lead time, is the conclusive factor. Normal near-vertical coupling is assumed to have a coupling efficiency of 28% on the fiber grating couplers of the PIC alignment sensor. Apart from the single angle polished fiber, all concepts are expected to have a slightly better coupling efficiency. The single angle polished is expected to have a coupling efficiency of at least two-thirds of that of near-vertical coupling. Inserting a coupling efficiency of 18.7% in the full PIC system efficiency estimate in appendix A, results in a full system transmission that is manageable for signal source and processing equipment (see 5.1.3). If the coupling efficiency of single angle polished fiber is sufficient and they are the least complex to manufacture, this concept is selected with conviction.

4.3. Setup configuration

The experimental setup will consist of multiple components that need to be positioned with respect to each other within a certain space. In this section, the different conceptual subsystems are shortly addressed, together with their degrees of freedom and the conceptual positioning stage configurations that were chosen, adhering to the requirements around these degrees of freedom. A schematic of the setup concept is depicted in figure 4.7. It consists of the following subsystems:

1. PIC chuck
2. Alignment marker scanning
3. Infrared imaging
4. Fiber coupling
5. Probe coupling
6. VIS imaging

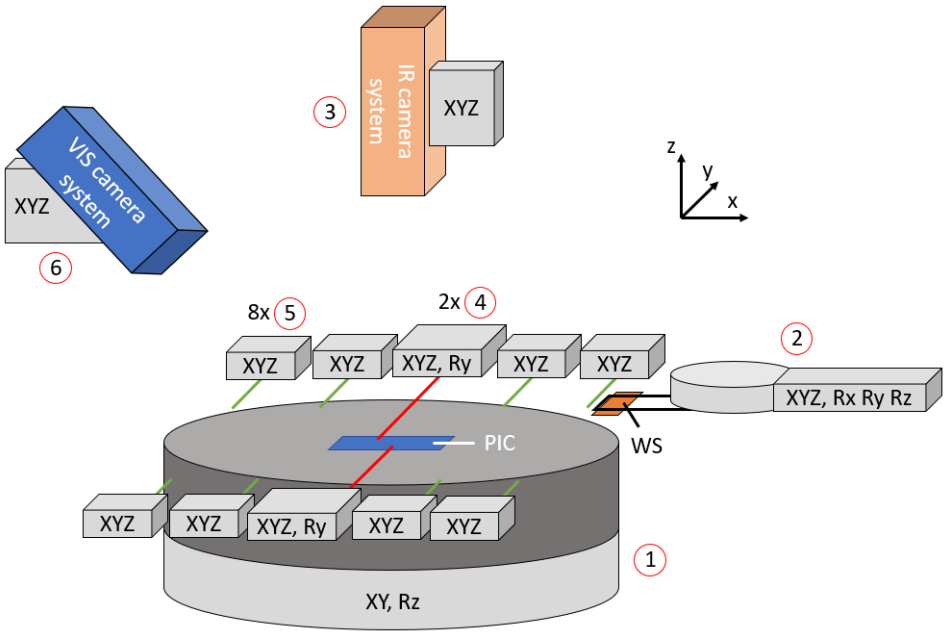

Figure 4.7: System schematic. Subsystems numbered according to enumeration above the figure.

The PIC chuck (fig. 4.7 (1)) is at the center of the setup and it facilitates a 3 inch (76.2 mm) IMOS wafer. PIC's located over the entire wafer must be accessible to all surrounding subsystems. Since most surrounding subsystems must be aligned fairly accurately with respect to the PIC under test, their positioning stages require a relatively high resolution. Within positioning stages there is always a trade-off between resolution and range within a certain price range. By adding two translation stages (X & Y) to the PIC chuck, large (coarse) movements to select a particular PIC on the wafer for testing are covered. It will enable the positioning stages of most surrounding subsystems to have small ranges that enclose one PIC in the XY-plane (4 mm × 20 mm) and thus maintain a high resolution. During measurements, the PIC chuck will be fixed. The PIC chuck is also able to rotate around the Z-axis, in order to align the PIC with the scanning (X-)direction of the wafer sample and the wafer sample itself in this rotational degree of freedom. It is a necessary addition resulting from the stage configuration of the alignment mark scanning subsystem (fig. 4.7 (2)), of which a schematic is shown in figure 4.8.

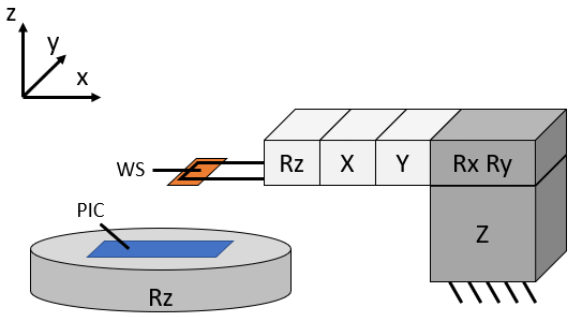

Figure 4.8: System schematic

The specific stage choice in the (alignment mark) scanning subsystem will be elaborated on in chapter 5, but in relation to the necessity for the PIC chuck Rz-stage, it is important to know that the wafer sample is mounted to the scanning system Rz-stage, which is located at the end of the series after the scanning (X-)stage. Regarding alignment of wafer sample to PIC, this implies that after mounting the wafer sample to the Rz-stage, the wafer sample can be aligned to the scanning direction around the Z-axis, but the scanning direction can not be aligned to the PIC around the Z-axis without an extra Rz-stage. This extra Rz-stage could be included either in the scanning subsystem or in the PIC chuck subsystem. The choice was made to include it within the PIC chuck, in order not to overcrowd the scanning subsystem. All positioning stages in the alignment mark scanning subsystem will be motorized. The effect of small marker orientation/location deviations from the nominal position on the detected alignment signal must be analysed over small ranges (approximately $\pm 20\,\mu m$ and 20 mrad in all degrees of freedom). With manual stages, the read-out accuracy and resolution over these small ranges is not sufficient enough. Motorization will also permit for automation, if needed in the future.

The infrared imaging system (fig. 4.7 (3)) is positioned above the PIC chuck and will capture the intensity profiles at different z-distances from the PIC. In section 4.1 the selection of an InGaAs camera with a magnifying objective was substantiated. With the rather large grating output angles from the PIC of up to 30°, there are two options to capture the emitted beams:

1. Imaging in planes parallel to the PIC surface (figure 4.9 left) with a NA over 0.55.

2. Imaging in planes tilted to the PIC surface (figure 4.9 right) with an NA below 0.55.

The advantage of option 1 manifests itself mainly in the positioning stages required for the imaging system. Only translation stages are needed to provide the capability of imaging profiles at different locations. Since the imaging system will have a mass of at least 2 kg and is brought close to the PIC from above, meaning it will have an overhang from its mounting position on the table, its stage configuration should remain as uncomplicated as possible for higher stability. Translation stages are a great deal better at handling loads and moments than rotational stages of the same size. Adding large rotational stages would also only add to the mass of the total system. The large NA (>0.55) in option 1 does come paired with some consequences for other optical properties. Firstly, a greater magnification is needed for a high NA, compared to what is required for our spatial resolution of $2\,\mu m$. A large magnification will result in a reduced FoV, limiting the size of the spots that can be imaged. On top of that, the working distance (WD) of a high magnification objective is rather low, which could pose a problem regarding the limited space above the PIC. Though, an advantage would be a decreased focal depth, which is beneficial for the alignment of the wafer sample to the PIC. Originating from the same arguments, option 2 is more complex in its positioning stage configuration, but the design space for the imaging system optical specifications is larger. Since the subsystem will also facilitate the alignment of the wafer sample to the PIC, as stated in section 4.1, stability is an important factor. Together with findings of existing objectives with specifications that will fit the requirements, the preference for option 1 was fixed. The Z-stage of the stage configuration will be motorized, providing the right accuracy, resolution and velocity that is needed for both grating output characterization and wafer sample to PIC alignment.

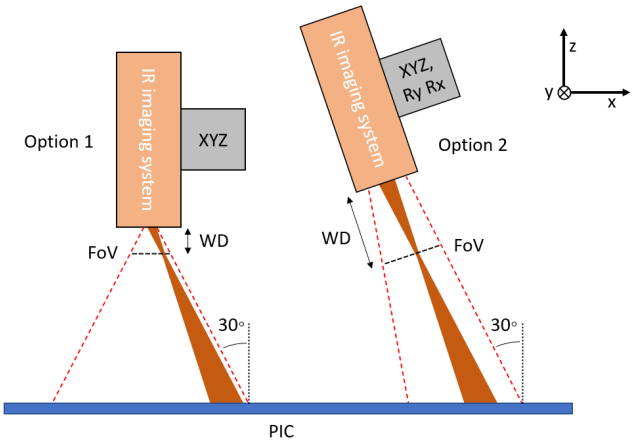

Figure 4.9: Schematic of the two imaging system configuration options.

The angle polished fiber modification concept selection was already discussed in section 4.2. The angle polished fiber subsystem (fig. 4.7 (4)) consists of two fibers, both supported by a stage configuration. The fibers must be aligned to 15 µm × 15 µm grating couplers and need sensitive translation stages in X,Y and Z to find the location of maximum transmission. Since the measurements that will be conducted on the PIC alignment sensor require a stable and sufficient coupling efficiency, but do not revolve around further study of the coupling process, manual stages are satisfactory. Figure 4.10 shows the conceptual orientation that was chosen between fiber and grating. As opposed to aligning the angle polished fiber orthogonal to the grating lines, which is common practice in the literature discussed in section 4.2, the fibers in the experimental setup will be aligned parallel to the grating lines. Naturally, the polarization state of the fiber for a particular grating would also have to change between these orientations. Alignment parallel to the grating lines in combination with a rotation stage with its axis of rotation coincident with the fiber axis, is superior to alignment orthogonal to the grating lines. That is because the chosen concept allows for fast AoI changes, without having to rearrange in other degrees of freedom since there are no (or less) additional motions. It will make alignment on a particular grating and switching between gratings of a different design easier.

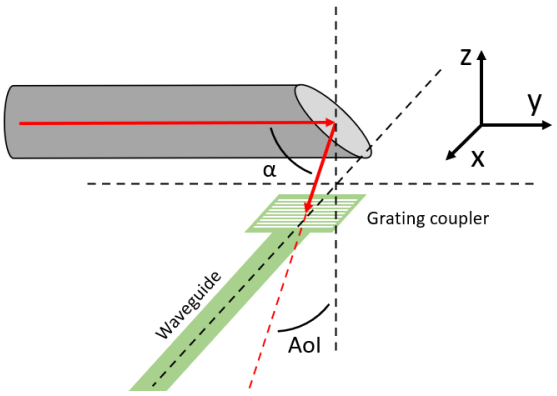

Figure 4.10: Schematic of conceptual fiber to grating orientation.

In case of full electrical operation of the PIC alignment sensor, the subsystem inserting and extracting the electrical signals (fig. 4.7 (5)) must bring 8 probes in contact to probe pads with dimensions of 50 µm × 50 µm. The probes need sensitive positioning in X,Y and Z over the range of the PIC surface.

The alignment of the fibers (and probes) will be done in two steps: coarse alignment and fine alignment. The components are too small to bring them close to each other with the naked eye. Coarse alignment will be conducted by a visible imaging system (fig. 4.7 (6)) at a working distance of approximately 100 mm, not obstructing the other subsystems. It is placed under an angle of 45° with the normal of the PIC. The distance between the imaged fiber tip and its reflection on the chip surface now gives an indication of their relative

position. The principle is visualised in figure 4.11. The fiber must be brought in close proximity to the grating in Z-direction without making contact, which could damage either the fiber or a structure on the PIC. When the fiber is coarsely aligned to a PIC and a transmitted signal is seen at the grating coupler at the other end of the structure under test (captured by the infrared imaging system), the next step is fine alignment. Fine alignment is accomplished by tuning the position in its degrees of freedom and maximizing the signal intensity at the detector. The VIS imaging system requires an appropriate magnification and spatial resolution for coarse alignment. The stage configuration should allow for movement in X,Y and Z. In order to correctly focus the imaging system on the PIC, either the stages should provide sufficient sensitivity, or the imaging system must consist of a focusing mechanism.

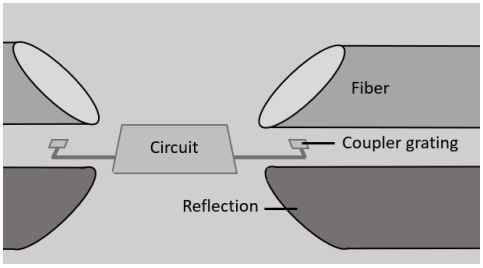

Figure 4.11: A schematic of the proposed image produced by the camera and lens combination, depicting the fiber tips, their reflection from the PIC and the fiber grating couplers.

5
Detailed design

For a global understanding of the experimental setup configuration, the reader is referred to section 4.3. In this chapter, the choice and design of the components per subsystem are presented (section 5.1) and the alignment strategy of subsystems, PIC and wafer sample with respect to each other will be elaborated on (section 5.2). The detailed design has been established by constantly evaluating the uncertainties and tolerances involved with the specifications and properties of certain design choices. Section 5.3 contains the error budgets for the essential requirements for setup performance: the Z-accuracy in intensity profile measurements and the repeatability of the alignment marker scan. The budgets have been filled with the values compliant to the definitive detailed design, which will provide us with the expected setup performance parameters. The descriptions of the subsystems in the first section are accompanied by figures of the digital 3D model. Pictures of a (nearly) complete setup can be found in appendix D.

5.1. Subsystems

The detailed design is structured per subsystem, in a similar order applied in section 4.3. A 3D model of the experimental setup is depicted in the figure below, to provide an initial feeling for the complete assembly that will be built up in the following subsections and trace back the subsystems. During the explanation of the detailed design per subsystem, certain alignment steps and uncertainty components are mentioned, at which the reader is referred to the relevant *step* (in *italics*) of the alignment strategy in section 5.2.

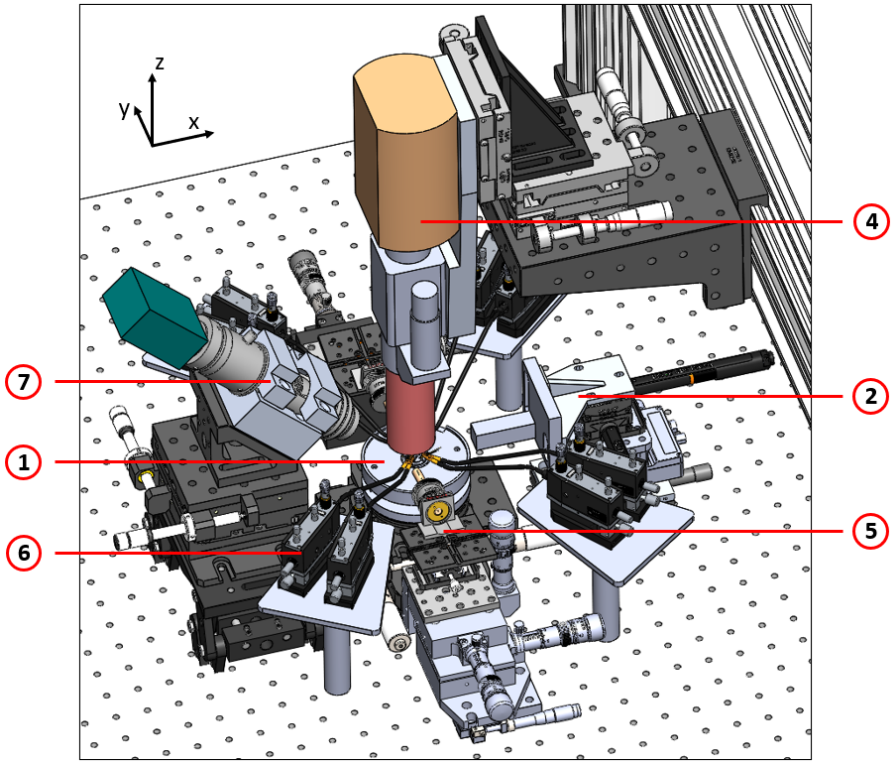

Figure 5.1: 3D model of experimental setup. **1**: PIC chuck. **2**: Alignment marker scanning stage. **4**: IR imaging system. **5**: Fiber coupling. **6**: Probe coupling. **7**: VIS imaging system. Rough dimensions of complete assembly: 1x1x1m.

5.1.1. PIC chuck

The PIC chuck subsystem is depicted in figure 5.2. It consists of two stacked translation stages, allowing for the positioning of a PIC located anywhere on the chuck, to the central region in the setup, accessible to all surrounding subsystems. As mentioned in section 4.3, the rotation stage plays a role in the alignment between PIC and wafer sample. The fine adjustment screw of the rotation stage provides an appropriate sensitivity to align the PIC to the scanning direction (*step C2*), within the alignment tolerances. All positioning stages are equipped with locking mechanisms to minimize drift. The aluminium chuck, a component not off-the-shelf, comprises of two parts: the bottom part is mounted to the rotation stage and the separate top part allows for connection of a vacuum tube with 90° connector to a straight vertical opening running from the bottom to the top surface. Pressurizing the IMOS wafer onto the chuck will also minimize drift. The engraved pattern in the surface must spread the range of the airflow and suck away a greater amount of dust particles. The reason for the 22.5 mm diameter of the pattern, instead of coverage over the complete chuck surface, is that the first PIC alignment sensor was initially expected to be delivered glued on a 25x25x1mm glass plate.

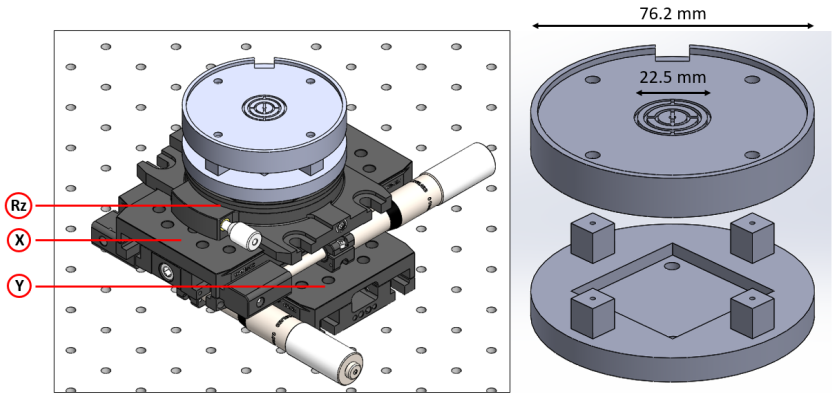

Figure 5.2: PIC chuck subsystem. The chuck consists of two parts to allow for vacuum tube mount. The X-, Y- and Rz-stage are indicated with the red circles

5.1.2. Alignment marker scanning

In figure 5.3, the different elements in the alignment marker scanning subsystem are presented. Its stage configuration (all motorized) corresponds to the schematic in figure 4.8. All positioning stage resolutions were chosen such that they are well below the fine alignment tolerances stated in table 2.1, in order to ease the alignment process and study small orientation deviations during a scan. How far the resolutions and displacement accuracies are below the fine alignment tolerances, is the result of other stage properties (dimensions, range, compliance with the other stages) making them suitable for application in the setup and a result of a limited variety in off-the-shelf stages. The Z-stage chosen is a vertical translation stage, which is space efficient and provides a stable platform as a base for the other positioning stages. It has a range of 20 mm with a 0.1 µm resolution. The range of the Rx- & Ry-stage combination is ±90 mrad with a 10 µrad resolution. The Z-, Rx- and Ry-stages do not include an integrated displacement sensor, resulting in relatively low absolute accuracies (specified by suppliers with 5 µm and 3 mrad respectively). However, the alignment strategy does not require high absolute accuracies for these degrees of freedom. The Y-, X- and Rz-stages do incorporate a displacement sensor. The X-stage, with a range of 16 mm, an accuracy of 30 nm and a resolution of 1 nm, will function as the scanning stage in our setup configuration and its properties will satisfy the requirements of this motion, which is explained later on in this subsection. The Y-stage with integrated displacement sensor has similar properties, meaning that this direction could also act as a scanning direction if the PIC is rotated 90° in Rz, in combination with a fiber orientation orthogonal to the grating lines (see section 4.3). The high precision Y-stage will also be used in *steps C1 and C5* of the alignment strategy. The Rz-stage is located at the end of the stage series, which has a full rotation 2π range and a 1 µrad resolution.

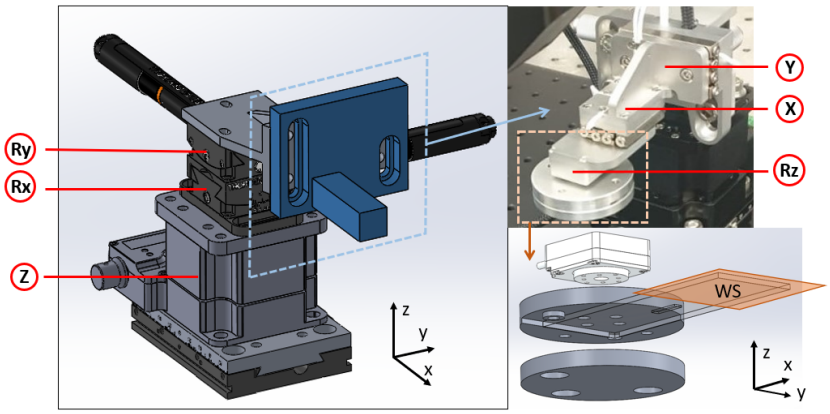

Figure 5.3: The alignment marker scanning subsystem. The different positioning stages are indicated in red circles. The wafer sample (WS) is depicted in orange, attached to the glass plate.

The wafer sample (25x30x0.5 mm) with the alignment markers facing downward is glued at the underside of one end of a glass plate with dimensions of 25.4x76.2x1.5 mm, which is clamped in between two aluminium components at the other end (fig. 5.3). The aluminium clamp is mounted to the underside of the Rz-stage. The glass plate serves multiple purposes. Firstly, it is a plate that extends the reach of the positioning stage configuration, without adding significant mass. The plate is thin and prevents a volume conflict with other setup components. Secondly, the glass plate will have a function in the alignment of the marker with respect to the PIC in the X- and Y-direction. It will do so by an integrated micrometer scale located on one side, in the center of the plate. The scale is visible through both sides of the glass with the infrared imaging system and this fact will make the mentioned XY-alignment possible. The process is explained in detail in *step C1* of the alignment strategy.

In order to determine if the scanning stage (X-stage) will satisfy our repeatability requirement, we turn to the content of chapter 3, where both the integrated displacement sensor error properties and alignment marker orientation errors were related to absolute position measurement errors. The displacement sensor error that is important for the repeatability of the scan is the periodic error, of which the period(s) must not be equal to the alignment signal period or its harmonics. There is a periodic error in the integrated sensor. The integrated sensor in the scanning stage is an optical encoder, which is a type of linear encoder. Its working principle is described below. Linear encoders are sensor reading heads united with a linear scale, along which position is encoded with geometrical patterns. They come in different orientations, but most often the construction comprises of a rod or a strip with the scale, which moves linearly through a housed sensor. An alternative configuration is a separate scale and sensor, where either of the two is attached to the moving component and the remaining one to a stationary member, so that the sensor hovers above the scale in close proximity. The physical properties exploited in linear encoders vary, such as magnetism and light [29]. We consider only the optical encoder, which has the highest resolution and precision. In essence, optical encoders operate by observing the scale lines with a light source and a detector. A broad distinction can be made between encoders not using optical interference and encoders that do. The one in the selected scanning stage is an encoder of the first type. Figure 5.4 shows a schematic of the basic configuration of the this optical encoder type. The scale of this incremental encoder consists of opaque and transparent parts. Around it, the light source and two detectors, A and B, translate, resulting in the square-wave signals of A and B. The detectors are spaced 90° from each other, resulting in a quadrature output. It means that one signal is trailing the other by a quarter of a period and the sign of this phase difference tells us the direction of the displacement. The higher the opaque strip density, the higher the resolution. In order to increase it further, square-wave signals can be fitted with a sinusoidal function, or a sinusoidal gradient can be applied in the encoder pattern [29]. The disadvantage of the periodic scale is the high probability of a periodic error. The period of the scale in the optical encoder of our scanning stage is 20 µm. Due to the quadrature output from the double signal, the period of the error becomes half the scale period, so 10 µm. The absolute overall accuracy specified for the scanning stage displacement sensor is ±30 nm. This could be a largely systematic error, which would not influence the repeatability of the scan. However, for now this accuracy is assumed to be the amplitude of the periodic error. Running the periodic error through the alignment marker measurement

fitting process (section 3.1) at different phase offsets between error and alignment signal, does not yield a significant contribution to the repeatability uncertainty.

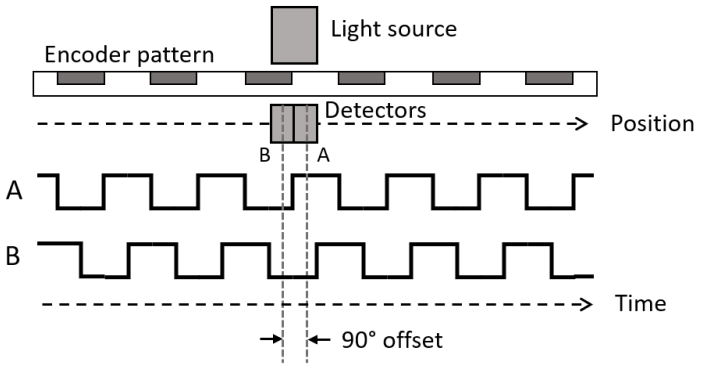

Figure 5.4: Schematic of a basic incremental optical encoder. Light source and detectors translate along scanning direction over encoder pattern (gray: opaque strips, white: transparent). [29]

Next, the influence of the combined marker orientation errors in Z & Ry and Y & Rz are taken into account. Since we are interested in the repeatability of a relative position measurement between two markers 10 mm apart, the influence reduces to the variation of the difference in these degrees of freedom between marker number one and marker number two. The variations of the error motions of the scanning stage play an important role. The error budget reveals that rotation variations around the Y- and Z-axis have the highest sensitivity (section 5.3), with 40 nm/mrad and 15 nm/mrad respectively, which we assume to behave linearly. The specified angular error motion over the full range of 16 mm is ±45 µrad for both Ry and Rz. In a worst case scenario, this error motion fully develops in the range between the two markers, being constantly 0 µrad at marker one and either 45 µrad or −45 µrad at marker two, or somewhere in between, differing per scan. The contribution to the repeatability would be ±4.3 nm. This number is expected to be lower, since the portrayed behaviour of the error motions is not very likely. The behaviour of the rotational error motions of the scanning stage around the Y- and Z-axis has been investigated, of which a description and result is included in section 6.

5.1.3. Light source & signal processing

In this subsection, the equipment is discussed that supplies and processes the optical and electrical signals to and from the PIC. A schematic overview of the selected equipment involved in the setup is depicted in figure 5.5. For a detailed description of the fiber and probe coupling subsystems, which transmit the signals to and from the PIC, the reader is referred to subsections 5.1.5 and 5.1.6. A description of the working principle of the PIC and its components can be found in section 1.2.3. The switches and on-chip laser sources are excited through current sources. The switches are expected to operate at a current around 100 mA and the laser sources around 500 mA. The alignment signal from the on-chip photodetector can be collected by applying a negative 5 V bias voltage. Although the estimated transmission of complete active/electrical PIC operation is at least 12 times higher than passive/optical operation (table A.1 [13]), active operation introduces a substantial amount of uncertainties. Active components are rather sensitive to defects during the manufacturing process and their performance is insecure. In other words, the probability of their transmission and noise contributions being insufficient is high. The priority of the feasibility study is situated around the passive components. The use of waveguides and fiber grating couplers is more established and stable from PIC sample to sample. That is why in this report, the focus will be on the surrounding optical equipment and its properties. The effect of bandwidth and total signal-to-noise ratio on grating output characterization and the alignment marker scan that must be conducted are important selection criteria for the different components.

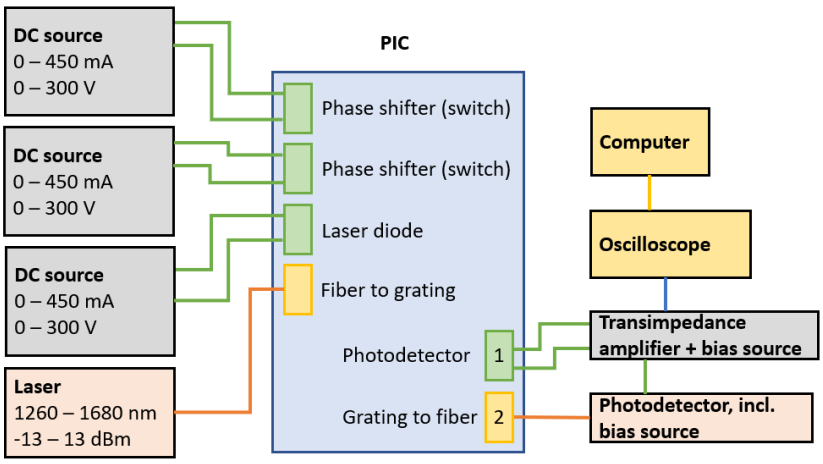

Figure 5.5: Schematic overview of signal source and processing equipment for optical and electrical PIC components. Green lines: current signals. Blue lines: voltage signals. Orange lines: optical signals

The selected laser source has a tunable wavelength over a range of 1260-1680nm and an adjustable output power between 0.05 mW and 20 mW. Its spectral bandwidth is 1.6×10^{-3} pm. Together with an ±15 pm wavelength accuracy, high precision grating output characterization is supported. The wavelength and power stabilities of ±5 pm and 1 mW over a period of one hour will both have a slight influence on the amplitude of the alignment signal (assuming correct PIC operation). The impact on the repeatability is negligible, since power transmission will remain high enough, as we will see later on in this subsection. The signal-to-noise ratio (SNR) of the laser source is >70 dB, which equals a ratio of $1E7$. The only noise source over the PIC in passive operation, would be a vibration of the fibers with respect to the gratings. In a later subsection 5.1.5, the fiber design is deemed to have no significant vibrations. At the other side of the PIC system, the alignment signal is coupled to the fiber and directed into a photo detector. The photodetector has responsivity of approximately 1 A/W at the 1550 nm wavelength. The photodetector is equipped with its own bias voltage source. The important parameter to consider is the Noise-Equivalent-Power (NEP), which is a measure for the sensitivity of the detector through its SNR. The NEP designates the incoming signal power that results in an SNR of 1 with an 1 Hz bandwidth. The current signal from the photodetector advances to the transimpedance photocurrent amplifier. The amplifier includes a bias voltage source, which should be applied to the on-chip photo detector in active PIC operation. There is a selection of current measurement ranges in the amplifier, from 100 nA to 10 mA, in decade steps. The noise equals 0.02% of the selected measurement range.

The important parameters of the optical signal supply and processing equipment have been explained. Before the effect of the SNR on the repeatability is determined, the velocity of the alignment scan is calculated. The limiting maximum bandwidth in the system belongs to the photodetector with 1 kHz. Assuming we want to utilize its full potential, the scanning velocity becomes a function of the proposed sampling distance of the alignment signal. A rule of thumb states that for a correct retrieval of period and amplitude, the number of samples must be at least 10 per period. With an alignment signal period of 1.6 µm, this results in a maximum scanning velocity of an alignment marker over the PIC of

$$\frac{1.6\,\mu m}{10} * 1\,kHz = 160\,\mu m/s \tag{5.1}$$

The scanning motion is only restricted to this velocity when the markers translate over the PIC emitting grating spot and could be increased in between the markers. For the SNR, the estimated power at the photodetector must be known. The estimated transmission of the complete PIC and marker system, included with the estimated coupling efficiency of the angle polished fiber (see section 4.2), is $3.1 * 10 - 5\%$. With a maximum input power of 20 mW from the laser, the optical power at the detector becomes 6.2 nW, which converts to 6.2 nA due to the detector responsitivity of 1 A/W. Linking the detector NEP with the chosen 1 kHz, results in an SNR of the detector of $7.8E6$. The amplifier current measurement range for 6.2 nA is the smallest 100 nA range, leading to a noise contribution of $0.02\% * 100\,nA = 0.02\,nA$, corresponding to an SNR of 310. The SNR contributions of the laser ($1E7$) and photodetector ($3.9E5$) are negligible compared to this amplifier contribution. In order to know how a sampling resolution of 0.16 µm and an SNR of 310 affect the repeatability

of the alignment marker scan, the noise and signal parameters are evaluated through the alignment marker measurement fitting procedure of section 3.1. A simulation of an alignment signal from a 160 µm long marker with the 310 SNR, yields an insignificant contribution to the measured marker position repeatability.

5.1.4. Infrared imaging

The 3D model of the infrared imaging system is depicted in figure 5.6. The optical specifications are listed in table 5.1. Both the optical components and the positioning stages have been selected to satisfy the requirements and suffice in the alignment strategy. As mentioned in section 4.3, the subsystem configuration that has been selected, applies a large NA and a stage configuration consisting of only translation stages. The NA of the objective is 0.65. The infrared camera is an InGaAs camera, containing a thermoelectric cooling element, a cooling fan and the possibility of liquid cooling, all to maintain a sensor temperature of −20°C and minimize dark current. With maximum optical power levels in the µW range from the PIC reaching the detector, liquid cooling will not be necessary. The pixel pitch is 15x15µm and the pixel array is 640x512. In combination with the magnification of the infrared objective, the Field of View (FoV) and spatial resolution of the system become 192 µm x 154 µm and 0.3 µm respectively. Over a Z-translation of ±125 µm around the PIC focal distance, the beams emitted from the PIC are retained within the FoV of the imaging system and a 3D representation of the beam can be retrieved by combining the 2D intensity profiles imaged at different Z-locations. The working distance of the objective is 10 mm, which provides a Z-distance of at least 10 mm between the objective and the PIC during grating characterization measurements, leaving enough space for fibers and probes. The Depth of Field (DoF) of the objective is 0.65 µm. The spatial resolution, FoV, working distance and DoF are parameters that are extensively used during the alignment strategy and determine with what uncertainties an alignment marker can be aligned to the PIC. The DoF also contributes to the total Z-position measurement accuracy of a 2D intensity profile (see 5.3). Alignment of the imaging system optical axis to the PIC surface is discussed in *step B1* of the alignment strategy.

Optical specifications

Magnification	50
Numerical aperture	0.65
Spatial resolution	0.3 µm
Field of View	192 µm x 154 µm
Working distance	10 mm
Depth of Field	0.65 µm

Table 5.1: Specifications of optics in IR imaging subsystem

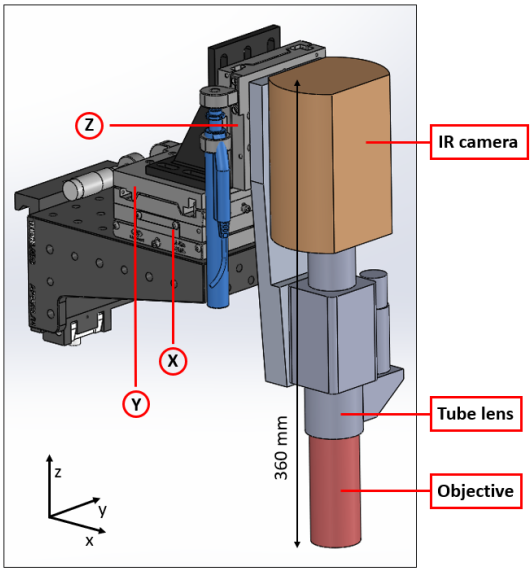

Figure 5.6: 3D model of the infrared imaging system. Positioning stages and optical components outlined in red.

The stage configuration consists of two manual translation stages (X- and Y-direction) and a motorized translation stage (Z-direction). They are the same type of positioning stage and share a range of 25 mm. Their selection was largely based on their load capacity, which is 325 N orthogonal and 80 N parallel to the direction of movement. It is sufficient for the imaging system load of 25 N on the vertical Z-stage and a load of 70 N on the X-stage, including the subsystem moment contributions. The motorized stage has a resolution of 0.1 µm and an absolute position accuracy of ±2 µm. The accuracy affects the total Z-position measurement accuracy of the 2D intensity profiles and the alignment uncertainty of alignment marker to PIC in the Z-direction (*step C4*). The rotational error motions of the Z-stage over the X- and Y-axis are specified to be 0.02 mrad over the 10 mm range used in the alignment strategy. Their contribution to the rotational alignment uncertainties Rx and Ry in *step C3* are considered insignificant. The small translational error motions of the Z-stage are also negligible. The IR imaging system is relatively large and can only reach the PIC chuck by extending over several other subsystems. This will be realized by mounting the anodized aluminium platform, underneath the X-stage (fig. 5.6), to an aluminium bridge extending over the experimental setup (fig. 5.1).

5.1.5. Fiber coupling

The fiber coupling method in the detailed design below is slightly altered with respect to the described method in section 4.3. Instead of introducing the angle polished fiber horizontally to the 15 µm x 15 µm grating coupler, it will be brought in under an angle of around 10°, denoted by ω in figure 5.7.

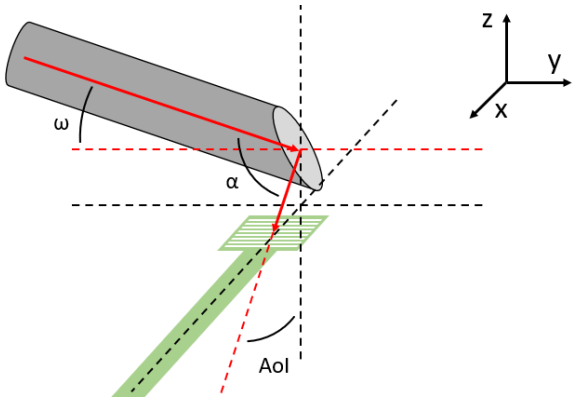

Figure 5.7: Schematic of fiber orientation with respect to fiber grating grating in final design.

The reason for this is the stability of the fiber. Figure 5.8 visualizes the difference between parallel coupling (left) and near-parallel coupling (right) from a complete setup perspective. The fiber requires support close to its tip for sufficient stability. Since the PIC chuck is designed for handling 76.2 mm IMOS wafers, supporting a fiber parallel to the PIC is complex. The fiber would only be accessible from above for a supporting structure and the wish for quick rotation adjustment of the fiber over the Y-axis (roll) reduces the possibilities for such a structure even more. With near parallel coupling, by adding an extra degree of freedom (rotation ω over Rx) to the fiber stage configuration, the fiber can be supported over a larger distance and the required range of grating coupler AoI's can still be achieved if the right fiber output angle α (fig. 5.7) is chosen, in combination with the range of the stage responsible for angle ω. The angles are related (through the dot product formula) as follows:

$$\omega = \sin^1 \frac{\cos(\alpha)}{-\cos(\text{AoI})} \tag{5.2}$$

Angle ω has a limited range due to space restrictions. This restriction depends on the location of the fiber grating coupler under the wafer sample positioned above it at $z = 10$ mm. Other factors are the length of the unsupported fiber tip and the dimensions of the supporting structure. The unsupported length is determined at a safe 20 mm with an ω range limit between 10° and 15°, ensuring the fiber will remain within the available space between PIC and wafer sample. The expected stability of a bare fiber tip with this length has been coarsely approximated in COMSOL (FEM software) by applying an airflow to the fiber and retrieving its displacement. Following a study to cleanroom airflows, the peak velocity in the airflow after large movements in the surrounding space is $v = 0.2$ m/s [30]. The force F on the fiber is assumed to be distributed according to the drag equation:

$$F = 0.5 * c_w * \rho * v^2 = 0.012\,\mathrm{N/m^2} \tag{5.3}$$

where c_w is an estimated drag coefficient for a smooth cylinder and ρ is the density of air. Applying this force over a single mode fiber with a length of 20 mm, results in a 0.08 µm deflection of the tip with. Although this approximation consists of large assumptions and the effect of this deflection on the coupling efficiency is complex to model, it does give an indication. This indication was enough to decide on continuing with this fiber coupling design.

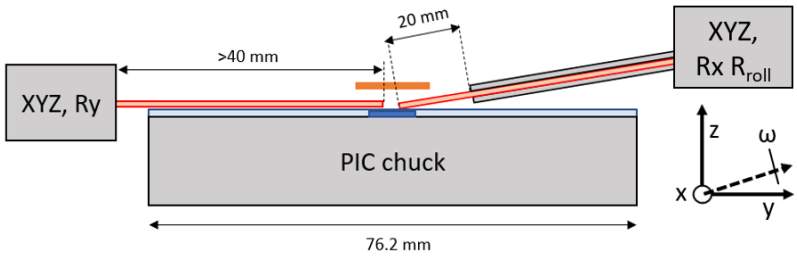

Figure 5.8: Schematic of fiber orientation comparison. Parallel to PIC surface on the left and near-parallel on the right. Wafer sample in orange, PIC in blue.

The fiber coupling subsystem is shown in figure 5.9. The combined XYZ-stage has a range of 13 mm in every direction. It is actuated manually with 1 µm scale resolution screws and contains locking mechanisms to minimize drift. Rotation of the fiber around the X-axis is achieved with a goniometer stage possessing a range of ±17° and a scale resolution of 1°. The read-out resolutions will be utilized during quantification of the fiber alignment tolerances with respect to the gratings (chapter 6). In the top left corner of figure 5.9, the rotation mechanism responsible for rolling the fiber over its own axis is schematically depicted. The fiber is clamped in a fiber chuck (yellow), which is mounted to the dark grey part of the mechanism. The light grey part is mounted to the goniometer and the dark grey part can rotate relative to the grey part over the fiber propagation axis. Knowing the unsupported length of the fiber and the dimensions of the fiber chuck, an appropriate tip angle ω of approximately 13° was chosen.

The fiber that is used is a polarization-maintaining fiber, which only allows linear polarization over two axes. The fiber has a polished angle over one of these axes and the laser source output polarization is restricted to one axis as a result of the connector between fiber and laser source. The polarization is incident parallel to the grating coupler lines (TE) on the PIC alignment sensor in the orientation of figure 5.7. With a change of grating coupler polarization design (TM, orthogonal to grating lines), a polarization converter can be used in between the laser source and the angle polished fiber. The chosen fiber output angle α of 90° + 13° is the result of the selected approximate tip angle ω and the range of relatively small AoI's of gratings that should be achievable (5°-15°), according to equation 5.2. This translates to a polished angle of 40.5°, using equation 4.5 in section 4.2 and refraction at the cladding-to-air interface.

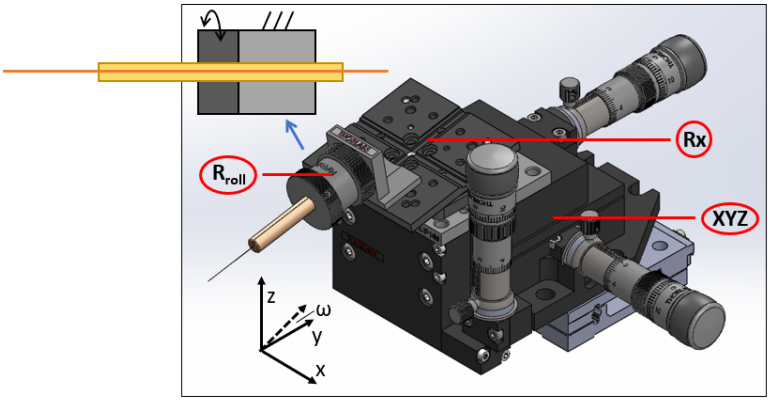

Figure 5.9: Fiber coupling subsystem. The schematic on the top left depicts the fiber chuck in its rotation mechanism. Positioning stages indicated in red.

5.1.6. Probe coupling

Mentioned earlier was the necessity for 8 electrical probes. In case of full electrical operation of the PIC alignment sensor, the subsystem inserting and extracting the electrical signals must bring 8 probes in contact to probe pads with dimensions of 50 µm × 50 µm. Figure 5.10 shows the micropositioner that is used in the setup to position a probe arm with probe needle in X,Y, and Z. Their ranges are 8 mm, 6 mm and 25 mm respectively. The micropositioners are placed in pairs on 4 platforms in the corners of the setup, which is apparent from figure5.1. The aluminium platforms are fixed to the breadboard via aluminium poles and their top surface is covered with a steel sheet. Since the micropositioners are mounted on magnetic bases, they can be coarsely positioned and secured over the surface of the platform. If none or only part of the probes are required for a certain experiment, the redundant probes can be easily removed to create more space. The coaxial probe arms and needles are going to be used for constant DC signals on the PIC alignment sensor, but allow for RF (radio frequency) signals in potential future research. The probe needles terminate in a tip with a diameter of 12 µm and make contact with a probe pad under an angle of 45°.

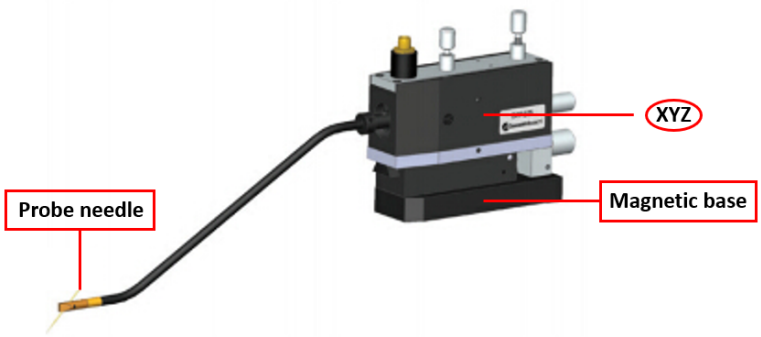

Figure 5.10: Probe coupling subsystem: XYZ-stage on a magnetic base, capable of positioning a probe needle mounted to a probe arm.

5.1.7. VIS imaging

The conceptual alignment strategy for the fibers and probes to their gratings and probe pads was described in section 4.3. A visible-light imaging system must perform coarse alignment. The magnification of the system must be rather high to sufficiently identify the 15 µm x 15 µm grating structures on the PIC. However, with such a high magnification, the FoV of the system would be too small to quickly recognize the location on the PIC in the image. Locating both the PIC structure and the fiber tip when they are not immediately in the same image, would be time consuming and the method would lose its purpose. For this reason, a camera with a zoom lens system has been selected, which is depicted in figure 5.11. Its optical properties are listed in ranges in table 5.2 below. The alignment of the fibers and probes with the VIS imaging system is elaborated on in *steps A1-A5* of the alignment strategy. The imaging will also be utilized in a verification step discussed in chapter 6.

Optical specifications

Magnification	1.16 - 14
Numerical aperture	0.019 - 0.101
Spatial resolution	3.03 µm - 0.25 µm
Field of View	9.5 mm - 0.78 mm
Working distance	86 mm
Depth of Field	0.95 mm - 0.1 mm

Table 5.2: Specifications of optics in VIS imaging subsystem.

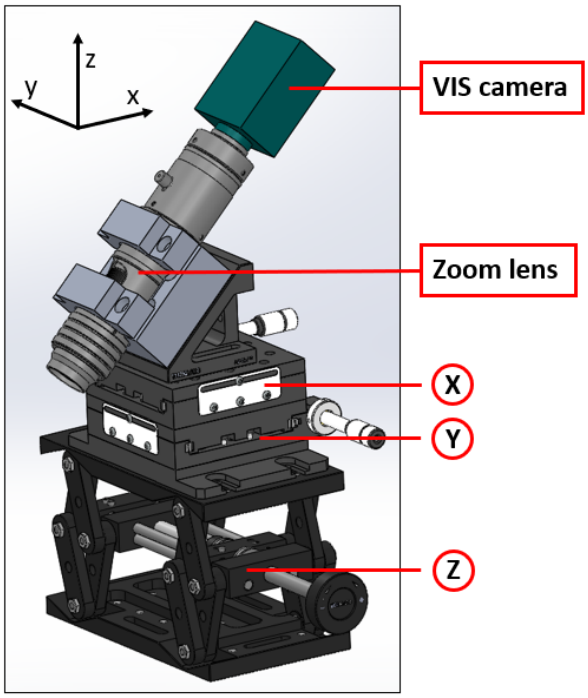

Figure 5.11: VIS imaging system. The camera and zoom lens system are under a 45° angle with the PIC surface.

5.2. Alignment strategy

The detailed design of all subsystems has been explained in the previous section. In this section, the alignment strategy is discussed, considering passive PIC operation (external optical power source and photodetector). First, the steps and actions involved will be treated per subsystem, together with their uncertainties contributing to a total alignment uncertainty. Then, a chronological overview of the alignment strategy is provided.

Before carrying out the alignment of all subsystems to the PIC in the subsections below, the PIC under test must have been positioned in the central region of the setup, accessible to all subsystems, with the translation stages underneath the PIC chuck. This position is fixed by tightening the locking mechanisms of the translation stages.

5.2.1. Fibers & probes

The steps taken to align both the fibers to their grating couplers and the probes to the probe pads of the switches are listed and explained in this subsection. The VIS imaging subsystem is utilized in this alignment process. In figure 5.12 below, a top view of the PIC orientation in the setup with respect to the fibers and probes is depicted. The four probe positioners on the upper two platforms are used for the two switches, to avoid obstruction of the optical paths between PIC and alignment marker. The PIC orientation in the figure could also be flipped 180°; the lower probe platforms would then have to occupied by micropositioners.

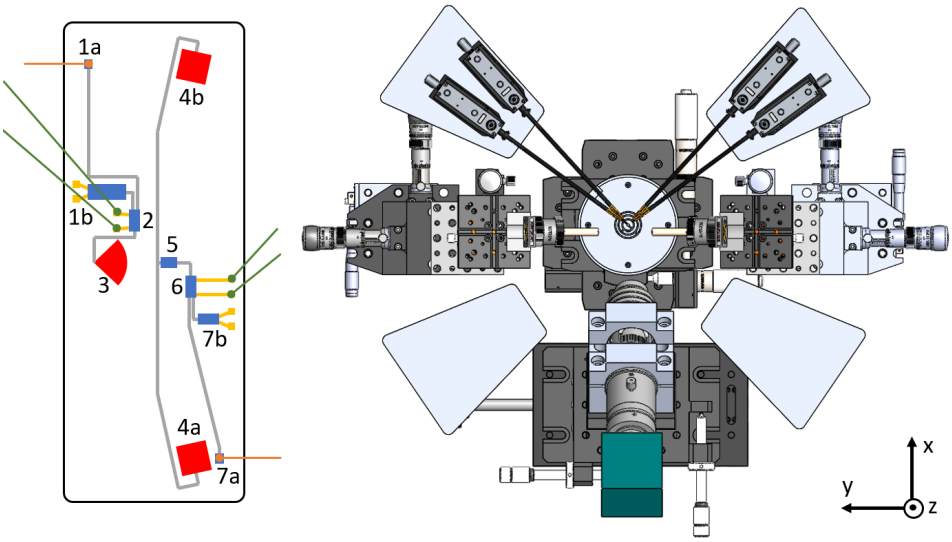

Figure 5.12: Top view of PIC orientation in experimental setup. Probes (green) brought in by positioners on upper platforms. Fibers depicted in orange. PIC component numbering complies to description in section 1.2.3.

A1 Coarse alignment of input fiber to input grating coupler (1a in fig. 5.12):

- During this step, the IR imaging system must be in an upper Z-position, with a Z-distance between the magnifying objective and the PIC greater than 20 mm. If the IR imaging system is close to the PIC, the objective is in the line of sight of the VIS imaging system, preventing a clear image of the fiber and its reflection.
- The desired AoI of the grating coupler is 9°. With equation 5.2, the correct tip angle ω of the fiber can be determined. The angle is realized by the goniometer stage and must be locked with its locking mechanism afterwards. The rotation mechanism that rolls the fiber over its axis is adjusted coarsely to the AoI of the grating coupler.
- With the use of the VIS imaging system, the fiber is coarsely aligned to the grating coupler. The method was visualised in figure 4.11. In the X- and Y-direction, the fiber is positioned roughly above the grating coupler. In the Z-direction, the fiber is brought close to its reflection from the PIC surface and is then locked in this degree of freedom. To prevent possible damage to the fiber or PIC structures, contact between the two must be avoided. The Z-distance from the PIC at which the fiber can be safely aligned using the VIS imaging system is expected to be below 15 µm.

* To conclude, the input fiber is now fixed in its rotational DoF's and its Z-translation. The coarse alignment in the X- and Y-translation is sufficient for a fraction of the light to be coupled into the waveguide and coupled out of the emitting grating coupler.

A2 Alignment of probes to probe pads of input switch (2 in fig. 5.12):

- The IR imaging system is still required to be in a raised position (z = >20 mm).
- The VIS imaging system is used to align the two probes to the two probe pads belonging to the input switch in X-, Y- and Z-direction. The probe tips must be in contact with the 50x50µm pads. The pads can handle small amounts of pressure, meaning that the tip should be translated over the Z-direction until it touches its reflection and shows no further movement when translating it downward a few additional micrometers.
* The two probes are now aligned to the input switch probe pads and require no further movement.

A3 Fine alignment of input fiber to input grating coupler (1a in fig. 5.12):

- The IR imaging system must be translated in X-, Y- and Z-direction and focused on (part of) the emitting grating coupler (3 in fig. 5.12). An IR LED illuminates the PIC and allows for the acquisition of an image by the IR camera. When the IR imaging system is positioned correctly, the IR LED is turned off.
- The laser source connected to the fiber and the current source (50 mA) assigned to the probes can be turned on. If coarse alignment has been done correctly, the emitting grating coupler couples light from waveguide to air, which is captured by the IR imaging system.
- Through adjustment of the current applied over the switch the intensity at the camera is maximized.
- Through displacement of the fiber over the X- and Y-direction the intensity at the camera is maximized. These DoF's are locked when the optimal location has been found.
* The input fiber has now been aligned and requires no further movement.

A4 Coarse alignment of output fiber to output grating coupler (7a in fig. 5.12):

- For this alignment step, the process described in step A1 can be repeated, but now with the second fiber at the output grating coupler.
* The output fiber is now fixed in its rotational DoF's and its Z-translation. It is coarsely aligned in the X- and Y-translation.

A5 Alignment of probes to probe pads of output switch (6 in fig. 5.12):

- Step A2 can be repeated for the output switch.
* The two probes are now aligned to the output switch probe pads and require no further movement.

A6 Fine alignment of output fiber to output grating coupler (7a in fig. 5.12):

- Step A6 is similar to step A3, but requires the following modification. The laser source that was initially connected to the input fiber, must now be connected to the output fiber. Thus, the capturing gratings will be used in reverse. The IR imaging system is focused on a part of capturing grating 4a or 4b (fig. 5.12). Their output is captured by the imaging system when the laser is turned on, since the fiber was coarsely aligned in step A4.
* The output fiber has now been aligned and requires no further movement.

5.2.2. Infrared imaging system

The infrared imaging system must be prepared for two purposes: intensity profile measurements and wafer sample to PIC alignment. For both objectives, the imaging system is aligned to the PIC, for which the steps are established in this subsection. The imaging system specifications listed in section 5 are essential in this process.

B1 Alignment of imaging system optical axis to PIC normal:

- The imaging system is first focused on a clear PIC structure. An IR LED illuminates the PIC surface and allows for the acquisition of an image by the IR camera. We assume that the orientation of the imaging system is not yet optimal w.r.t. the PIC, meaning that the image of the structure is only partly in focus.

- The imaging system optical axis will be aligned to the PIC normal by adjusting the imaging system rotation over the X- and Y-axis until everything in the FoV of the imaging system is in focus. Figure 5.13 schematically depicts the maximum alignment uncertainty to the PIC normal, represented by angle θ, which is a function of the Field of View (FoV) and Depth of Field (DoF) of the imaging system:

$$\theta = \pm\tan^{-1}(\text{DoF}/\text{FoV}) = \pm\tan^{-1}(0.65/154) = \pm 4.3\,\text{mrad} \tag{5.4}$$

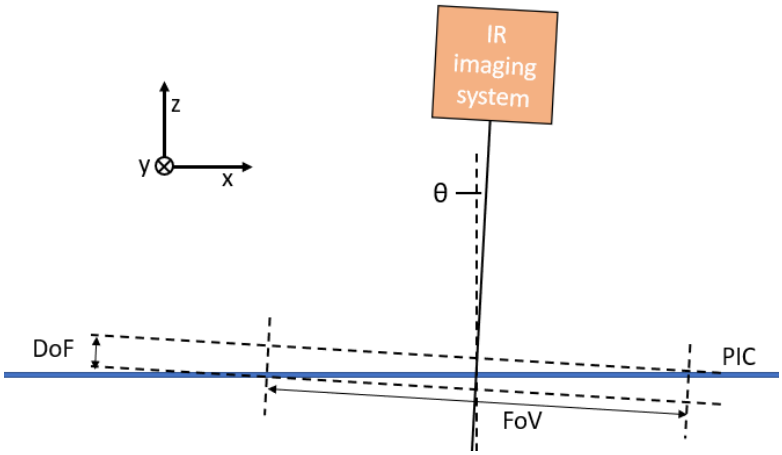

Figure 5.13: Schematic of alignment uncertainty between imaging system and PIC normal, where the DoF and FoV are applied in the alignment approach.

In order to align within ±4.3 mrad of the PIC normal, the imaging system needs adjustment around the X- and Y-axis with a resolution below this range. With shim stock, applied between the imaging system Z-stage and XY-stage combination (see figure 5.14) at the three bolting locations, tip and tilt of the imaging system can be accomplished. With a shim thickness of 50 µm and a distance dx of 25 mm between the shimming locations, the adjustment resolution around the Y-axis becomes approximately $\tan^{-1}(0.05/25) = 2$ mrad. For simplicity, we assume the adjustment range around the X-axis to be equal to that around the Y-axis.

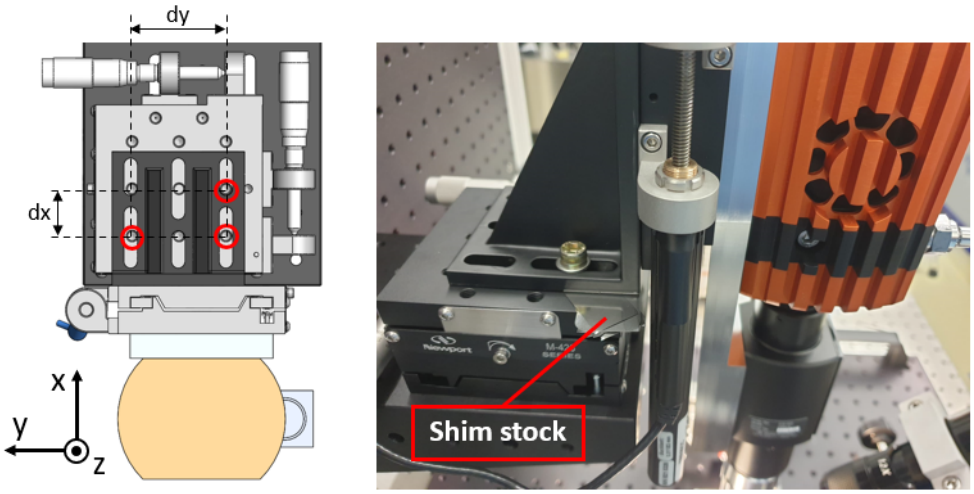

Figure 5.14: On the left: Top view of IR imaging system with bolt locations for shim stock. On the right: actual application of shim stock.

* This step of the alignment process is highly iterative. By repeatedly adding a layer of shim stock, bolting the imaging system down and refocusing it via Z-stage movement, imaging the full FoV in focus is achieved, meaning the optical axis is within 4.3 mrad of the PIC normal. It is supposed to be a stable, one-time alignment step, supporting measurements on the PIC for longer amounts of time.

B2 Alignment of imaging system focal point to PIC emitting and capturing grating focal point:

- First, the imaging system is focused on the PIC beam combiner structure (5 in fig. 5.12). This PIC Z-location is set to zero in the imaging system Z-stage. A first estimated position uncertainty contribution is caused by the depth of field of 0.65 µm. Another Z-position uncertainty contribution is the ±2 µm accuracy of the Z-stage.
- The beam combiner on the PIC is not in the center of the PIC. The focal point of the emitting and capturing gratings is in the XY-center of the PIC, at a Z-distance of 10 mm above the PIC. The imaging system must be coarsely translated 175 µm over the Y-axis to the center of the PIC. There are no features in the center to validate a potential error motion in the Z-direction. The estimated Z-uncertainty contribution is ±1 µm, originating from the alignment uncertainty from step B1.
- Next, the imaging system is translated in the upper Z-direction to a 10 mm read-out position of the motorized stage, ideally the exact location of the focal point of the PIC gratings. Due to the 4.3 mrad orthogonality alignment uncertainty, there is a possible misalignment in the X- and/or Y-direction of approximately ±40 µm. With a correctly functioning PIC, the spots emitted by either the emitting grating or capturing gratings are still within the FoV and they will not have to be searched for.

* The imaging system is now aligned to the PIC in the Z-direction. The Z-position uncertainty contributions mentioned will be combined with other contributions in section 5.3. The X- and Y-position are aligned sufficiently to image a spot from the PIC immediately. The center of the FoV of the imaging system must then be translated to the center of the spot. The imaging system is fixed in the X- and Y-direction through their stage locking mechanisms.

M1 Measuring intensity profiles and comparing the emitting and capturing grating spot locations:

The imaging system is now ready to do measurements concerning the characterization of gratings. If the emitting grating spot must be measured, the laser source is connected to the input fiber, coupled to the input grating (1a fig. 5.12). If the capturing grating spots must be profiled, the laser source is connected to the output fiber, coupled to the output grating (7a fig. 5.12). Lastly, if the spot of only one capturing grating must be profiled, the optical path of the beam from the second capturing grating must be obstructed. By inserting one of the four unused probe arms (with a diameter of 4 mm) without their probe needle above a capturing grating, as shown in the schematic of figure 5.15, one beam is

prevented from reaching the imaging system. Separate profiling is better for grating characterization and spot location comparison.

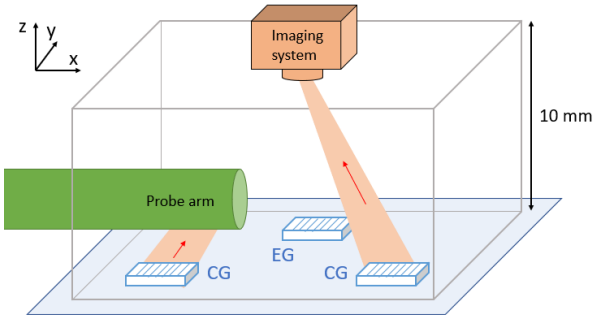

Figure 5.15: Schematic of capturing grating beam obstruction by a probe arm.

5.2.3. Alignment marker

If the intensity profile measurements performed by the IR imaging system show that the spots of emitting and capturing grating share the same location at Z is 10 mm, the alignment marker can be aligned in preparation for a scan. In appendix B, the alignment tolerances between an alignment marker and the PIC alignment sensor were elaborated on. Table 2.1 lists the fine alignment tolerances: the required tolerances that must be satisfied before performing an alignment marker scan. To achieve this, the alignment strategy is divided into two parts:

1. **Coarse alignment (C1-C5)**: with the use of the IR imaging system, the alignment marker is aligned within the coarse tolerances listed in table 5.3. Where the fine alignment tolerances are specified by the diffracted beam spots still being completely incident on the capturing gratings (section 2.2), the coarse alignment tolerances are defined by half of the spots being incident on the capturing gratings. Aligning within these tolerances will ensure a transmitted signal over the complete PIC system to the photodetector at the end of the output fiber.

2. **Fine alignment (C6)**: With a transmitted signal after coarse alignment, the alignment marker can be aligned within the fine alignment tolerances, through optimization of the signal strength.

marker alignment tolerances

	Coarse	**Fine**
Rotation X	±17 mrad	±6 mrad
Rotation Y	±15 mrad	±1.5 mrad
Rotation Z	±60 mrad	±20 mrad
Translation Z	±700 µm	±70 µm

Table 5.3: Alignment marker to PIC coarse and fine alignment tolerances around nominal position.

C1 : Locating the alignment marker w.r.t. the scale on the glass plate in the X- and Y-direction (one-time action):

- During the performance of a marker scan, the wafer sample that is glued underneath the glass plate faces downward, with its structures accessible to the light beam coming from the PIC. In this alignment step, the glass plate is mounted in reverse to the scanning stage subsystem. Figure 5.16 depicts the reversed mounting, with the chip structures facing upward, visible to the IR imaging system.

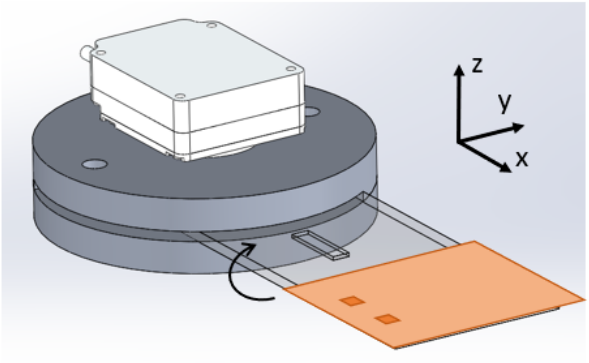

Figure 5.16: Glass plate with wafer sample (orange) mounted in the reversed position. The chip structures (alignment markers in dark orange) are now directed upward.

- The IR imaging system is stationary throughout this step and all movement is performed by the wafer sample stage configuration. The wafer sample is brought into the IR imaging system FoV. Similar to the process described in step B1, the wafer sample must be adjusted around the X- and Y-axis until the complete FoV is in focus. A clear structure on the wafer sample is to be used, while providing illumination with the IR LED.

- Now, the first alignment marker (80 µm - 160 µm) on the wafer sample that is to be scanned is positioned in the center of the FoV, our reference position. Using the high precision X- and Y-stages of the scanning stage configuration, one of the scale lines on the glass is brought into the FoV. The distances dx and dy, shown in figure 5.17, are determined accurately by the integrated displacement sensors.

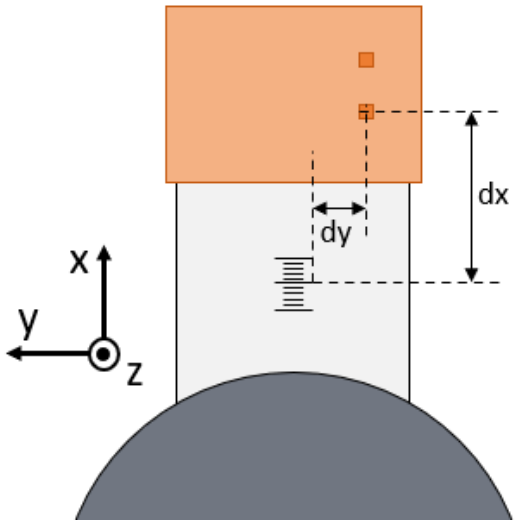

Figure 5.17: Schematic of top view of glass plate and wafer sample in reversed mounting orientation. The alignment marker location is related to a scale line and its angle.

- The glass scale line is still in the FoV and its angle around the Z-axis w.r.t. the camera FoV frame must be calculated. This scale line angle is determined by summing the length of the pixels vertically (P_v) and horizontally (P_h) in the image. The method is depicted in figure 5.18 and it is applied in future steps as well. The pixel size does introduce an uncertainty in the measured angle because of the pixel size (P_s). With a pixel array of 640x512, the uncertainty becomes $\pm\tan^{-1}(1/640) = \pm 2$ mrad, which will have an influence on step C5.

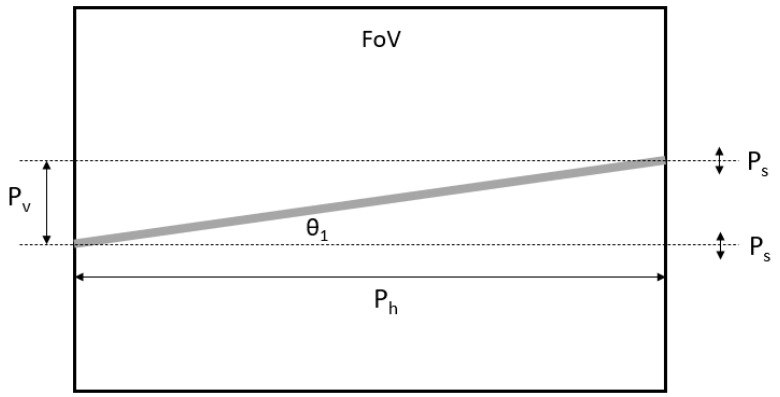

Figure 5.18: Schematic of IR camera FoV with scale line in grey. Its angle w.r.t. to the imaging system is determined by counting pixels, with an uncertainty introduced by the pixel size.

* The XY-distance between the alignment marker and a scale line, including the lines angle over the Z-axis w.r.t. the IR imaging system is known after this step. It is a one-time step and will only have to be repeated with a change of wafer sample. With this information, the marker can be aligned to the PIC in these two translations when the alignment marker is facing towards the PIC (step C5). The scale line angle uncertainty will affect this alignment accuracy. Other factors like stage error motions are negligible.

C2 : Coarse alignment over Rz of marker and PIC to scanning direction:

– For this step, the glass plate is mounted in the correct orientation, with the marker facing downward to the PIC. The scanning direction, which is the direction of the X-stage in the wafer sample stage configuration, can not be rotated around the Rz-axis, since there is no Rz-stage present between the X-stage and the fixed world. There are Rz-stages present between the X-stage and the wafer sample and underneath the PIC chuck. The IR imaging stage is positioned 20 mm above the PIC, its focal plane 10 mm above the PIC and the IR LED is on.

C2.1 First, the wafer sample is aligned to the scanning direction. Figure 5.19 shows the procedure. The edge of the wafer sample is inserted in the FoV of the IR imaging system. When translating the wafer sample over the scanning direction, the edge of the wafer sample will shift in the lateral direction of the FoV if the wafer sample is not correctly aligned to the scanning direction. By repeatedly applying rotations with the wafer sample Rz-stage and scanning over a distance of 10 mm until the lateral shift is smaller than 1 pixel (undetectable), the wafer sample is aligned to the scanning direction around the Z-axis. Similar to the uncertainty calculation of the scale angle in step C1, this Rz-alignment uncertainty is a function of the spatial resolution (corresponding to a pixel) and the scanned distance: $\pm\tan^{-1}(0.3/1 * 10^4) = \pm 0.03$ mrad, which is insignificant for our alignment tolerances. A contribution that ís significant, is the dicing uncertainty of the edge w.r.t. the structures on the chip. We are interested in the alignment of the marker to the scanning direction, but used the wafer sample edge. The dicing Rz-tolerance is expected to be ± 1.5 mrad over the 10 mm X-stage movement that was applied.

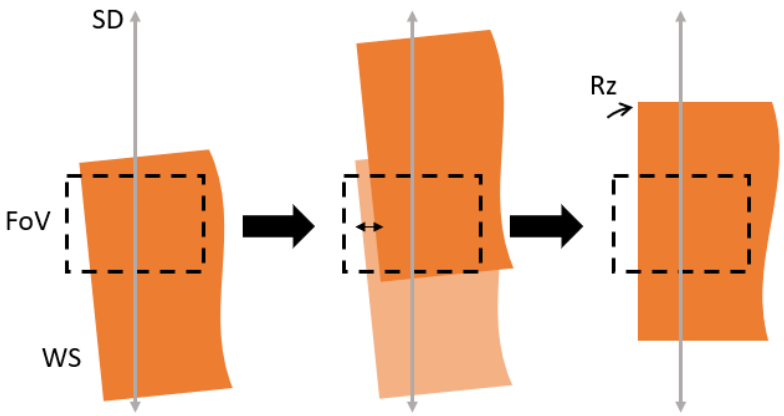

Figure 5.19: Schematic of alignment procedure of wafer sample (WS) to scanning direction (SD) around the Z-axis.

C2.2 Secondly, the PIC must be aligned in Rz to the marker and the scanning direction that were previously aligned to each other. For this, the angle of the wafer sample edge w.r.t. the IR camera is determined, after its alignment to the scanning direction (procedure in fig. 5.19). The method is identical to the one implemented for the glass plate scale line angle shown in figure 5.18. The IR imaging system is then translated down over the Z-axis and focused on a PIC structure that should be parallel to the scanning direction. This structure could be a piece of waveguide in between the beam combiner and the output switch, or the row of probe pads along the edge of the PIC. The angle that was deduced from the wafer sample edge before, must now be obtained between the chosen structure and the FoV of the camera, through rotation of the Rz-stage underneath the PIC chuck. Again because of the pixel size, the uncertainty contribution is ±2 mrad. After alignment of the PIC in Rz, the Rz-stage of the PIC chuck is locked.

* The alignment marker has now been coarsely aligned to the scanning direction in Rz with an uncertainty of ±1.5 mrad. The PIC is coarsely aligned to the alignment marker with two uncertainty contributions: 1.5 mrad (dicing tolerance) and 2 mrad (FoV and pixel method uncertainty). The error motions around the Z-axis of the both the IR imaging Z-stage and the stages in the wafer sample stage configuration are negligible. Step C2.2 is a one-time alignment step and the PIC is fixed afterwards.

C3 : Coarse alignment over Rx and Ry of marker to PIC:

- In step B1, the IR imaging system was aligned to the PIC surface in Rx and Ry. With the imaging system at a Z-distance of 20 mm from the PIC (focal plane at 10 mm) and the illuminating IR LED on, the wafer sample is brought into the FoV. The alignment method is similar to the one in step B1, but since there are no structures on the side of the wafer sample visible to the IR imaging system, the edges of the wafer sample are used
- In order to align in Rx, the wafer sample edge, approximately parallel to the Y-axis, is translated under the FoV (fig. 5.20 left). The Rx-stage of the wafer sample is rotated until the entire edge is in focus, while neutralizing additional Z-motion with the Z-stage of the wafer sample.
- In order to align in Ry, the wafer sample edge approximately parallel to the X-axis is translated under the FoV (fig. 5.20 right). The Ry-stage of the wafer sample is rotated until the entire edge is in focus, while neutralizing additional Z-motion with the Z-stage of the wafer sample.
- The alignment marker has now been coarsely aligned to the PIC in Rx and Ry, with two times the uncertainty contribution of ±4.3 mrad from equation 5.4 described in step B1, in both degrees of freedom.

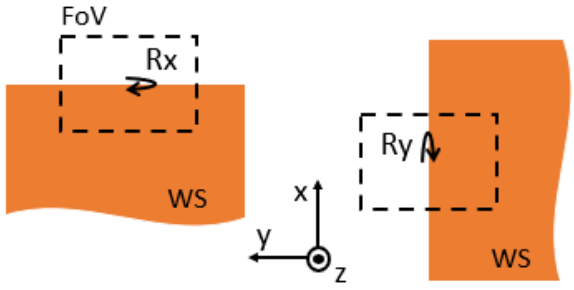

Figure 5.20: Schematic of alignment procedure of wafer sample to PIC in Rx and Ry, by bringing the edges fully into focus.

C4 : Alignment of marker Z-position to PIC focal point Z-location:

- The IR camera system is positioned at a Z-distance of 20 mm plus the wafer sample thickness of 500 µm. The focal plane of the imaging system will be at a Z-distance of 10.5 mm above the PIC surface.
- The wafer sample edge closest to the alignment marker, which is either the left or right one parallel to the scanning direction, must be brought into the FoV of the camera and focused by adjustment of the wafer sample Z-stage.

∗ Alignment of the marker w.r.t. the PIC in the Z-direction is now completed and the wafer sample Z-stage is fixed. There are several uncertainty contributions involved with this method. The accuracy of the IR imaging system Z-stage (±2 µm) and the depth of field (0.65 µm), play a role at both the Z-location measurement of the PIC in step B2 and the Z-location determination of the marker. Another contribution emerges from the alignment uncertainty in Rx of the wafer sample w.r.t. the IR imaging system (±4.3 mrad), in combination with the distance from the focused edge and the marker. The schematic in figure 5.21 explains this contribution. The distance between the edge and the marker of interest is approximately 5 mm and it introduces an extra Z-uncertainty of the marker (dz_m) of ±22 µm maximally. A last contribution would be the thickness tolerance of the wafer sample, which is ±15 µm.

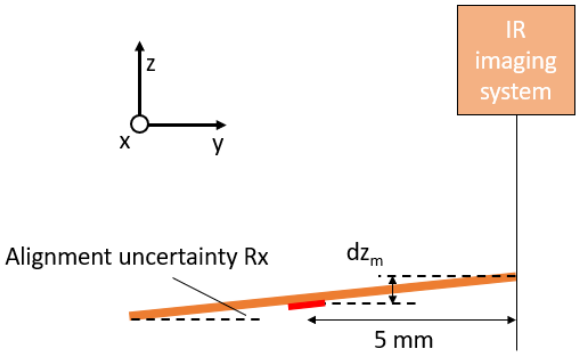

Figure 5.21: Schematic of marker Z-direction alignment uncertainty contribution from edge focusing method with alignment uncertainty Rx.

C5 : Alignment of marker X- and Y-position to PIC focal point X- and Y-location:

- The X- and Y-position of the marker w.r.t. a glass plate scale line and the scale line angle w.r.t. the IR imaging system in Rz were determined in step C1. Since the scale lines are visible from both directions of the glass, the marker position can be deduced from the particular scale line and its new angle.
- With the use of the wafer sample X- and Y-stage and the imaging system Z-stage, the scale line used in step C1 is brought into the FoV. The angle is again determined by counting pixels (method of figure 5.18).

– Figure 5.22 depicts the marker location determined in step C1 (left) and the to be calculated location in this step (right). We are interested in the angle difference $d\theta$ between the angle in step C1 (θ_1) and the angle now (θ_2). It is defined by $d\theta = \theta_1 - \theta_2$ since the glass plate, and thus the initial marker location and scale line angle have been flipped over the X-axis. The presumed marker location then follows from a rotation matrix as follows:

$$\begin{bmatrix} dy_2 \\ dx_2 \end{bmatrix} = \begin{bmatrix} \cos(d\theta) & \sin(d\theta) \\ -\sin(d\theta) & \cos(d\theta) \end{bmatrix} \begin{bmatrix} -dy_1 \\ dx_1 \end{bmatrix} \tag{5.5}$$

– Through translation of its X- and Y-stage, the wafer sample is moved to the deduced marker location (dx_2, dy_2).

∗ The marker is now positioned close to the PIC focal spot location in the X- and Y-direction. There is one uncertainty contribution, which originates from the scale line angle calculation uncertainty. It adds a maximum error in the deduced marker position of approximately 60 µm, due to a double 2 mrad uncertainty in $d\theta$ and the distance between scale line and marker of 15 mm.

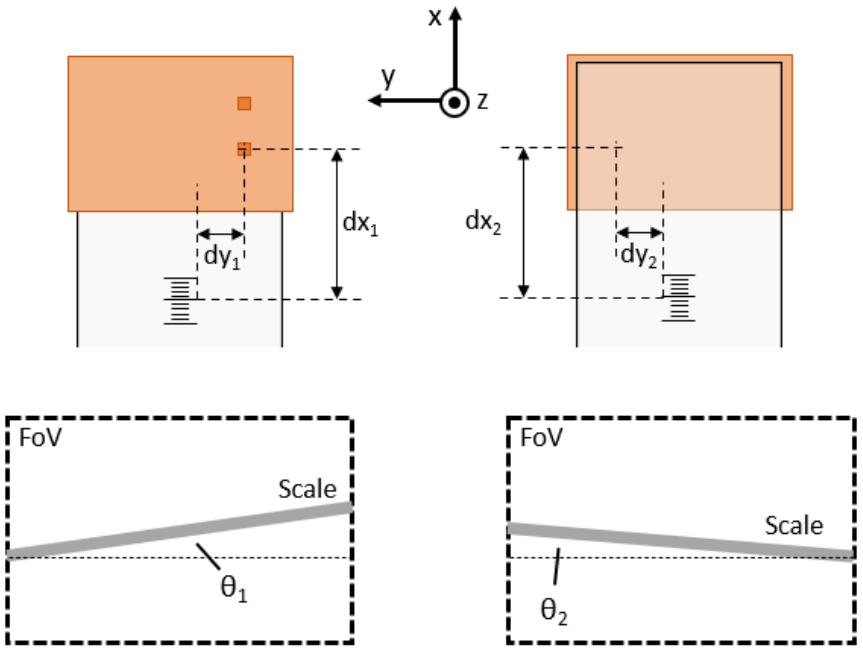

Figure 5.22: Schematic of marker X- and Y-location with scale angle from step C1 (left) to step C5 (right)

.

Coarse alignment uncertainties

The alignment marker has been coarsely aligned to the PIC, in orientation and position. The different uncertainty contributions, arising from the IR imaging system specifications and certain tolerances, are assumed to have a rectangular probability distribution. After linear addition of their impact per degree of freedom, we arrive at the table below with the coarse alignment standard uncertainties (2σ) including a safety factor of 0.5.

marker coarse alignment uncertainties

Rotation x	±15 mrad
Rotation y	±15 mrad
Rotation z	±6 mrad
Translation z	±46 µm

Table 5.4: Alignment marker to PIC alignment uncertainties after coarse alignment.

These values are within the coarse alignment tolerances of table 5.3 and expectedly provide a sufficient transmission for a measurable optical signal at the photodetector. That is, if the marker is positioned correctly

in the X- and Y-direction w.r.t. the PIC focal point. With a spot diameter of 40 µm, a marker with dimensions of 160 µm by 80 µm and a marker position uncertainty in the focal plane of ±60 µm (step C5), the spot might not be incident on the marker. During the fine alignment procedure described below, these and the other degrees of freedom are aligned to within the fine alignment tolerances, preparing for the alignment marker scan.

C6 : Fine alignment of alignment marker in all degrees of freedom by transmission optimization:

- To be able to align by optimization of the signal at the photodetector, one of the capturing gratings must be blocked by an unused probe arm, as depicted in figure 5.23. It prevents interference from the second diffraction order, which could decrease the optical power at the photodetector when the alignment actually improved. Also, the laser source is turned on.

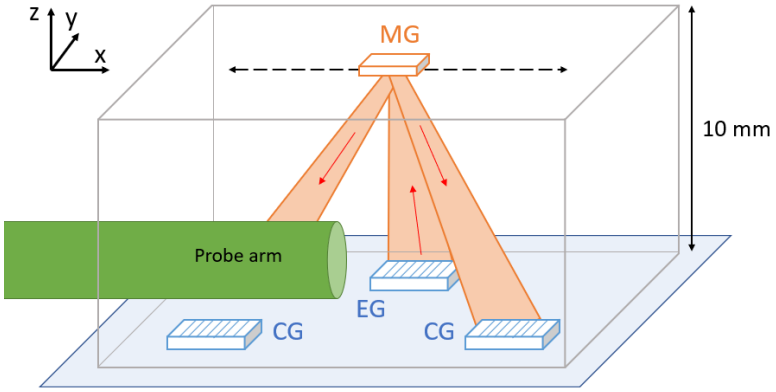

Figure 5.23: Schematic of diffraction order beam obstruction by a probe arm.

- Next, the marker must be correctly positioned in the X- and Y-direction. As was concluded after the coarse alignment, the marker (160 µm by 80 µm) is within an approximate 60 µm radius of its ideal position. It is highly probable that the spot from the emitting grating already overlaps with the marker sufficiently for a signal a the photodetector. Through translation over the Y-direction, the center of the 80 µm width marker can be found. With the spot size being 40 µm, the transmission function over this direction will have a near-flat 40 µm region. Then, by wafer sample translation over the X-axis, the edges of the marker over the scanning direction can be identified. For the rest of the procedure, the presumed center of the marker is positioned coincident with the spot center.
- The expected alignment uncertainty in Rz is already below the fine alignment tolerance. The wafer sample Rz-stage remains untouched.
- Fine alignment over Rx of the marker is an iterative process in combination with Y-stage alterations. Figure 5.24 shows that the distance between the marker and the Rx rotation axis of the stage configuration is approximately 40 mm in the Z-direction, which results in additional Y-movement of the marker with a rotation over the X-axis. By rotation steps of 1 mrad, the shift over the Y-axis of 40 µm will still ensure an overlap of half the spot on the marker and thus a captured signal. The shift can in turn be removed by maximizing the signal with wafer sample Y-stage movement. If one iteration of a rotation in Rx and shift over Y leads to a higher intensity at the photodetector, the alignment has improved. The additional motion in the X-direction with Ry rotations is negligible.
- Fine alignment over Ry of the marker is also an iterative process in combination with Z-stage alterations. The distance between the marker and the Ry rotation axis of the stage configuration is approximately 150 mm in the X-direction, which results in additional Z-movement of the marker with a rotation over the Y-axis. By rotation steps of 1 mrad, the shift in Z of 150 µm will still ensure a captured signal (table 5.3) and this shift can in turn be removed by maximizing the signal with wafer sample Z-stage movement. If one iteration of a rotation in Ry and shift over Z leads to a higher intensity at the photodetector, the alignment has improved. The additional motion in the

X-direction with Ry rotations is negligible. The discussed procedure for Ry simultaneously finely aligns the marker in the Z-direction.

* The alignment marker is now aligned finely to the PIC.

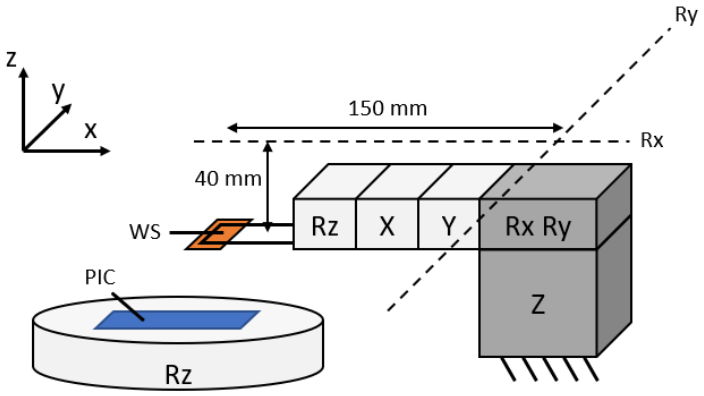

Figure 5.24: Schematic of wafer sample stage configuration with axis of rotation.

M2 Performing an alignment mark scan:

The wafer sample must be translated over the X-direction to the point where the emitting grating spot is right before the edge of the marker, meaning minimal transmission at the photodetector. After removing the probe blocking one of the capturing gratings, the experimental setup is ready for a series of alignment marker scans.

5.2.4. Chronological overview

In the previous section, the alignment strategy was presented structured per subsystem, to provide clarity of the different steps involved. For the strategy to reach the objective of performing an alignment mark scan, the steps follow a different chronological order. The overview of this chronological alignment strategy is presented below.

1. **B1** Alignment of IR imaging system optical axis to PIC normal. The tip/tilt of the imaging system is now fixed. It is a one-time step and can easily be checked at another time by focusing on an FoV filling PIC structure.
2. **C1**: Locating the alignment marker w.r.t. a scale line on the glass plate in the X- and Y-direction. This is a one-time action, if the wafer sample and glass plate combination is not replaced.
3. **C2**: Coarse alignment over Rz of marker and PIC to the scanning direction. The PIC is now fixed in all degrees of freedom.
4. **A1-A6**: Alignment of fibers and probes to the PIC. Fibers and probes are fixed in all degrees of freedom.
5. **B2**: Alignment of IR imaging system focal point to PIC emitting and capturing grating focal point. The imaging system is fixed in the X- and Y-direction.
6. **M1**: First experimental objective of the setup: measuring intensity profiles and comparing the emitting and capturing grating spot locations.
7. **C2.1**: Alignment over Rz of marker to the scanning direction. This step was already conducted (C2). However, if a large amounts of time have been spent on extensive M1 measurements, this part of step C2 should be repeated.
8. **C3**: Coarse alignment over Rx and Ry of marker to PIC.
9. **C4**: Alignment of marker Z-position to PIC focal point Z-location.
10. **C5**: Alignment of marker X- and Y-position to PIC focal point X- and Y-location.
11. **C6**: Fine alignment of alignment marker in all degrees of freedom by transmission optimization.
12. **M2**: Second experimental objective: performing an alignment mark scan.

5.3. Error budget

The most important requirements around the experimental setup objectives, influenced the most by the design choices, are the Z-accuracy of the intensity profile measurements and the repeatability of the alignment marker scan. Their error budgets were formulated and utilized during the design process. These budgets are expanded on below, containing the values that eventually composed the definitive detailed design. Some uncertainty contributions have been mentioned and explained earlier, a few are added in this section.

5.3.1. Infrared imaging

The error budget for the Z-accuracy performance of intensity profile measurements is provided in table 5.5. It incorporates the significant uncertainty sources, their expected probability distribution (with the complying divisor) and their sensitivity. The sensitivities are the effects on performance, determined by taking the derivative of the relation between error source and performance. The standard uncertainty is then calculated by dividing the 2σ estimated uncertainty by the divisor and multiplying it with the sensitivity. The contribution by the depth of field is introduced in alignment *step B2*, where the IR imaging system is calibrated to the PIC surface location. The IR imaging Z-stage accuracy contributes to both the PIC surface calibration and the intensity profile measurements, translating to a sensitivity of 2. The two remaining uncertainty sources, although small, are the thermal stability of the PIC chuck and the imaging system. The chuck temperature change over the time of a measurement (below 1 hour), is assumed to be 0.1 °C. That of the imaging system is assumed to be higher, due to the cooling elements in the camera, reducing the sensor temperature to −20 °C. Their sensitivity is equal, since the subsystems are both assumed to be made from only aluminium and the distance to their thermal center is roughly the same. The contributions resulting from the alignment uncertainty between the imaging system optical axis and the PIC normal, or from stage error motions, are insignificant. The first two uncertainty contributions in table 5.5 are added linearly to the root sum square of the thermal stability contributions, resulting in a 2σ total Z-accuracy of 6 µm.

Contributor	**Estimated uncertainty** (2σ)	**Unit**	**Probability function**	**Divisor**	**Sensitivity**	**Standard Uncertainty** (µm)
Depth of Field	0.65	µm	Rectangular	1.73	1	0.38
Z-stage accuracy	2	µm	Rectangular	1.73	2	2.31
Thermal stability PIC chuck	0.1	°C	Normal	2	2.36	0.12
Thermal stability IR imaging system	0.25	°C	Normal	2	2.36	0.3
Total standard uncertainty (TSU) (1σ)						3.01
TSU (2σ)						6.01

Table 5.5: Intensity profile Z-position error budget.

5.3.2. Alignment marker scan

The different error sources in the position measurement of a single alignment marker have been explained in section 3.2. They consist of the signal quality contributions and the marker orientation errors. The periodic error of the displacement sensor was proven insignificant in section 5.1.2. The SNR is sufficiently high and does not contribute to the measurement repeatability (section 5.1.3). The relevant marker orientation errors, will have an impact on the position measurement of an alignment marker. Since the setup will perform a scan over two alignment markers 10 mm apart, the marker orientation differences will affect the distance measured between them. The requirements state that only the repeatability of this distance measurement is of importance, which translates to the variation of the orientation differences between the markers over multiple wafer sample scans. The origins of the relevant orientation differences and their impact on distance measurement are explained first. From there, the sensitivities of certain contributions are used and combined with the expected orientation difference variation, for an estimation of the repeatability performance.

The relevant degrees of freedom in marker orientation/location deviations impacting marker position measurement accuracy, came in two combinations: rotation Ry with translation Z and rotation Rz with translation Y. The distance measurement error contributions from the differences between the two markers in the first combination (Ry & Z) are introduced in the setup by:

A. A misalignment in Ry between wafer sample and scanning direction, leading to:

   (1) A difference in Z-location between the markers.

   (2) An incorrect travel distance recorded by the scanning stage (X) displacement sensor.

B. The scanning stage error motions in Ry and Z over the 10 mm scan length.

The first error source, the misalignment in Ry between wafer sample and scanning direction, is visualized in figure 5.25. Since the Ry-stage of the wafer sample is located between the scanning X-stage and the fixed world (see fig. 5.24), any Ry deviations between the wafer sample and the scanning direction due to mounting, can not be neutralized. The mounting from wafer sample to X-stage, consists of: glue between the sample and the glass plate, clamping of the plate with two aluminium components, bolting that clamp to the Rz-stage and mounting it altogether to the X-stage. This estimated Ry uncertainty is 2 mrad and in figure 5.25 all its contributions have been compiled in θ_{glue} for simplicity. The resulting Z-location difference dZ will add a distance measurement error dX_1 together with the added stage error motions in Ry (Ry_e) and Z (Z_e), contribution B in the enumeration, according to equation 3.6, resulting in:

$$dX_1 = 2(Ry_e)(dZ + Z_e), \qquad \text{with} \quad dZ = \theta_{glue} * 10\,\text{mm} \tag{5.6}$$

A second implication of the misalignment between wafer sample and scanning direction is the travelled distance of the scanning stage from marker to marker, also shown in figure 5.25. It adds a distance measurement error dX_2:

$$dX_2 = \frac{10\,\text{mm}}{\cos(\theta_{glue})} - 10\,\text{mm} \tag{5.7}$$

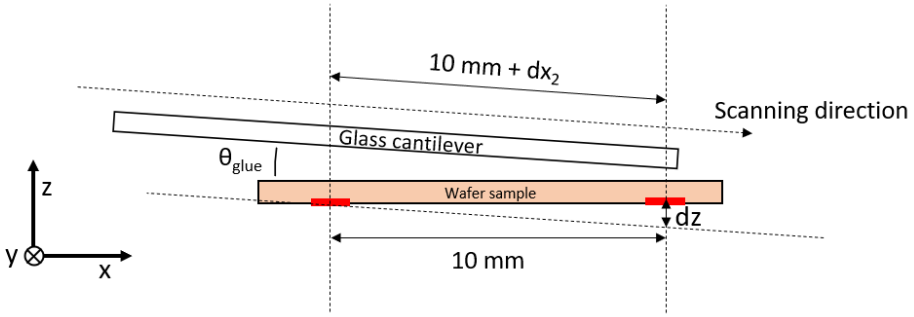

Figure 5.25: Schematic of error effects by mounting misalignment between wafer sample and scanning direction in Ry.

The distance measurement error contributions from orientation/location differences between the markers in Rz and Y originate from:

C. The alignment uncertainty in Rz between the alignment markers and the scanning direction, resulting in:

   (3) A difference in Y-location between the markers.

   (4) An incorrect travelled distance recorded by the scanning stage (X) displacement sensor.

D. The scanning stage error motions in Rz and Y over the 10 mm scan length.

The build-up of these Rz and Y combination error contributions is very similar to those of the Ry and Z combination. Figure 5.26 shows the result of the alignment uncertainty in Rz (Rz_u) between marker and scanning direction. Alignment strategy step C2.1 elaborated on an expected uncertainty of 1.5 mrad. It leads to a difference in Y-location (dY) between the markers, which will, in combination with scanning stage error motions in Rz (Rz_e) and Y (Y_e), add a distance measurement error dX_3 according to equation 3.7, translating to:

$$dX_3 = (Rz_e)(dY + Y_e), \qquad \text{with} \quad dY = Rz_u * 10\,\text{mm} \tag{5.8}$$

A second implication of the misalignment between markers and scanning direction is the travelled distance of the scanning stage from marker to marker, which is depicted in figure 5.26. It adds a distance measurement error dX_2:

$$dX_4 = \cos(Rz_u) * 10\,\text{mm} - 10\,\text{mm} \tag{5.9}$$

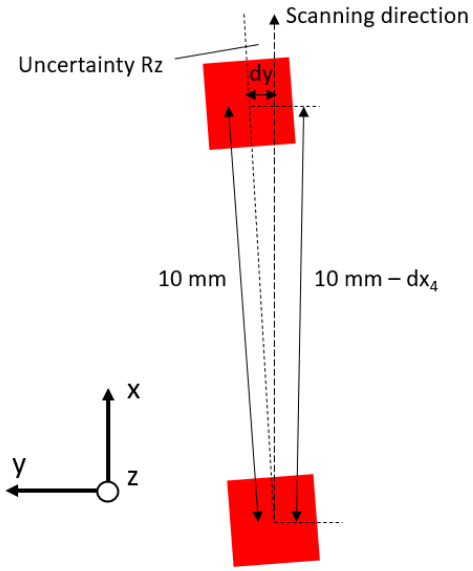

Figure 5.26: Schematic of error effects by alignment uncertainty between the markers and the scanning direction in Rz.

All the mentioned contributions to an error in the distance measurement between two markers have been compiled in the error budget of table 5.6, filled with the estimated uncertainties of the contributions. The standard uncertainty components are added linearly and they result in a total distance measurement uncertainty 2σ of 35 nm. Since we are interested in the repeatability and not in the distance measurement error, mainly the sensitivities of certain contributions are of importance. In other words, the variation of the contributions between different scans will impact the repeatability. The angle θ_{glue} and the alignment uncertainty of the wafer sample in Rz to the scanning direction, are assumed to be stable after over a series of scans. The sensitivities of the translational error motions are considered to be insignificantly small. The two rotational error motion sensitivities remain, with 40 nm/mrad and 15 nm/mrad in Ry and Rz respectively. Unfavorable behaviour of these error motions was shortly described in subsection 5.1.2. Assuming a worst case, the error

motions, each specified at 45 µrad, could lead to a repeatability of 4.3 nm. In order to prove that the contribution from the scanning stage error motions is lower, the two rotational error motions are investigated in chapter 6.

Contributor	**Estimated uncertainty** (2σ)	**Unit**	**Probability function**	**Divisor**	**Sensitivity**	**Standard Uncertainty** (nm)
θ_{glue}	2	mrad	Rectangular	1.73	20	23.1
Error motion Z	0.1	µm	Rectangular	1.73	$9 * 10^{-5}$	$5.2 * 10^{-3}$
Error motion Ry	45	µrad	Rectangular	1.73	40	35
Alignment uncertainty Rz	1.5	mrad	Rectangular	1.73	-15	-13
Error motion Y	0.1	µm	Rectangular	1.73	$1.5 * 10^{-3}$	$8.7 * 10^{-2}$
Error motion Rz	45	µrad	Rectangular	1.73	15	0.4
Total standard uncertainty (TSU) (1σ)						11.16
TSU (2σ) 0.5 safety factor						35

Table 5.6: Marker distance measurement error budget

6
Setup verification

The experimental setup was designed to satisfy the requirements stated in chapter 2. It is expected to do so with the specifications and expected uncertainties elaborated on in chapter 5. In this chapter, certain values and working principles concerning the most important setup functions (grating output characterization, fiber coupling and marker scanning) are verified.

6.1. IR imaging system

The main requirement of the infrared imaging system is the Z-position measurement accuracy, which must be below ±25 µm. In section 5.3, an expected accuracy of ±6 µm was deduced. In order to determine if the requirement is met, the accuracy is verified with the method described in this section. Aside from the Z-accuracy, other parameters like orthogonality of the optical axis and stability of the imaging system are discussed shortly as well.

Verification of the Z-accuracy is done by placing a gauge block with a known thickness on the PIC chuck and using the infrared imaging system to measure the distance between the chuck surface and the top surface of the gauge block. The approach is depicted in figure 6.1. The gauge block has dimensions of 24x75x50mm. In the direction of its thickness (24 mm), it fits within the range of the imaging system Z-stage. The thickness tolerance is 13 µm over the complete block. Although the method for a distance measurement with the imaging system (using its depth of field and Z-stage) has been explained previously in section 5.2, it is clarified once more for this particular verification procedure:

1. The imaging system is focused on the PIC chuck surface through its motorized Z-stage motion. With the IR LED illuminating the chuck, the slight inconsistencies in the surface become imageable for the IR camera.

2. The imaging system is translated upward to a relative 24 mm Z-position.

3. The gauge block is placed on the chuck, at a position where one of its edges is in the FoV.

4. The imaging system is focused on the edge of the gauge block by translation over the Z-axis.

5. The relative distance between the two objects reported by the motorized Z-stage actuator is noted.

This distance measurement was conducted 15 times, at different PIC chuck surface locations and different gauge block edges. The mean error of the series was −3.9 µm, meaning that the relative distance measurement averaged 24 m − 3.9 µm. The 2σ standard deviation, or repeatability, of this error was 1.9 µm. Together with the gauge block tolerance of 13 µm, the verified performance of IR imaging system Z-position measurement accuracy becomes 18.8 µm at maximum. The additional observation that the entire FoV was in focus at both the PIC chuck surface and the gauge block top surface, led to the presumption that the 4.3 mrad uncertainty between the PIC chuck normal and the imaging system optical axis (equation 5.4) is maintained over the entire Z-stage range. However, this remains an assumption, since this observation was only made at two Z-locations and nowhere in between those locations. The short and long term stability of the imaging system was also examined. There is some vibration present in the imaging system, apparent from the image captured by the camera. The image oscillates with a frequency around 15 Hz and an amplitude no more than ±1 pixel around a nominal position over the X-axis (coordinate system fig. 5.1), which equals ±0.3 µm through the spatial resolution. The source of this vibration around the setup, which is built on a vibration isolating optical table, has not been found. The relatively heavy imaging system mounted to the overhanging bridge

proves to be susceptible to vibrations. The small vibration has no significant influence on the system performance. The drift of the imaging system over 30 minutes was investigated, also by observing the image. No shift of the object in the image could be confirmed, meaning the drift is below 0.3 µm, a negligible amount.

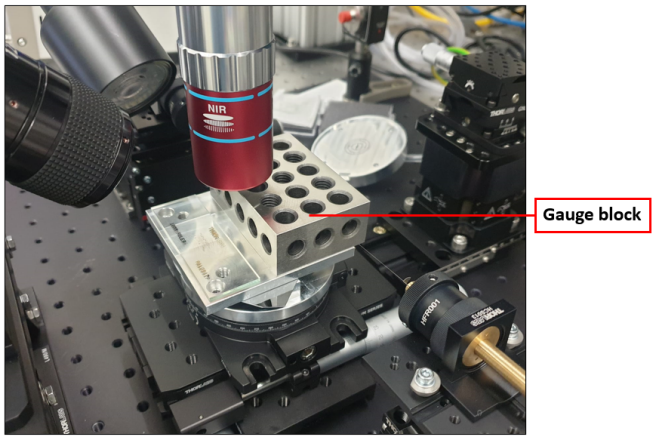

Figure 6.1: Picture of gauge block placement under the IR imaging sytem.

6.2. Fiber-to-chip coupling

This section is concerned with the verification of multiple aspects regarding the coupling of light between the angle polished fiber and a 15x15µm grating coupler. First, the output of the fiber is characterized and compared to the model of the expected output (appendix C). Then, light is coupled into a grating coupler to examine the coupling efficiency and the alignment tolerances of the fiber w.r.t. the grating coupler. Since the PIC alignment sensor experienced delays in the manufacturing process and was not delivered in time, an alternative PIC was used, containing short waveguide and grating coupler structures. During the verification of fiber-to-chip coupling only one angle polished fiber was available to us, affecting certain verification methods and their uncertainties.

For the characterization of the fiber output, the fiber was brought in under the IR imaging system parallel to the focal plane, as depicted in figure 6.2. By imaging 2D intensity profiles of the beam at different Z-locations from the fiber, a 3D representation of the beam could be made. Figure 6.3 (right) shows a fiber intensity profile measurement at $Z = 100\,\mu m$. Figure 6.3 (left) shows a 3D plot of the intensity profiles imaged between 0 µm and 100 µm from the cladding-to-air interface of the fiber, with 5 µm steps. The edges of the spots are defined by the $1/e^2$ of their maximum. The output angle of the fiber was determined by fitting a line through the centers of all spots, resulting in an angle of 18.05°. According to the expected behaviour of angle polished fiber, discussed in appendix C, this output angle corresponds to a polishing angle of 38.8±0.4°. The uncertainty in this angle originates from a measurement uncertainty of the output (fiber parallelity to focal plane) and a calculation uncertainty in the APF output model. The fiber was ordered with a polishing angle of 40.5° and the supplier specified a tolerance of ±1.5°. Since there is an overlap between the specified polishing angle and the measured/calculated polishing angle, the fiber is considered to be just within the supplier's qualifications.

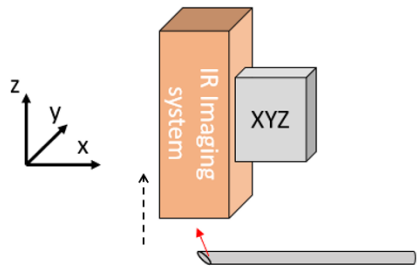

Figure 6.2: Schematic of fiber and imaging system orientation for fiber output measurement.

The 18.05° output angle is larger than the intended 13.1° with a 40.5° polishing angle (section 4.2). The difference is the result of double the polishing angle error 1.7° and the increased refraction at the cladding-to-air interface. A larger insertion angle *omega* of approximately 18.3° (equation 5.2) will be required. With respect to the space restriction of the fiber, the larger angle ω poses no problem. However, the goniometer stage, with a range of ±17°, is not able to reach the 18.3° angle. Figure 6.4 shows the resulting error ϵ introduced at the grating coupler, which is a rotation over an axis orthogonal to the gratings lines of approximately 1.3°. Considering previous research into fiber alignment tolerances, this error is expected to decrease the coupling efficiency by 20% at most [14].

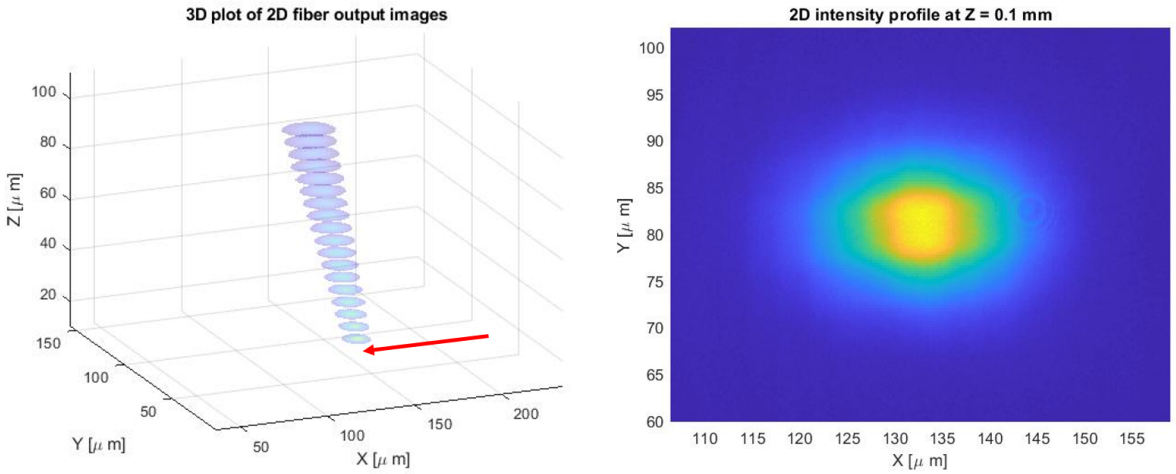

Figure 6.3: Left: 3D plot 2D intensity profiles measured at Z-locations between 0 µm and 100 µm from the cladding to air interface. The fiber direction is illustrated by the red arrow. Right: 2D intensity profile measured at $Z = 0.1$ mm.

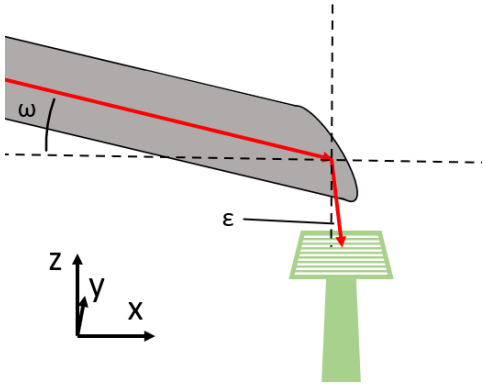

Figure 6.4: Schematic of rotational error ϵ as a result of deviating fiber output angle and limiting goniometer stage angle ω.

The $1/e^2$ spot diameters of the measured output and the expected output of the fiber over the output propagation axis are compared in figure 6.5. In the Y-direction, the divergence is reduced by the cylindrical shape of the cladding-to-air interface, while the beam expands in the X-direction, as expected. The measured output in the X-direction closely matches the expected output below a 50 µm distance from the fiber, which is deduced in appendix C. The distance between fiber and grating will be lower than 50 µm, so the model provides a good approximation of the spot size on a grating in this X-direction. In the Y-direction, there is a slight discrepancy in the divergence between the measured and modelled output divergence. The lower divergence of the measured output could be attributed to refraction at the core-to-cladding interface (also cylindrical), which was not considered in the model. However, a refractive contribution at that interface would also lead to a smaller measured spot size versus the predicted spot size at the cladding-to-air interface, which is not the case. Nevertheless, the predicted angle polished fiber output is comparable to the measured output.

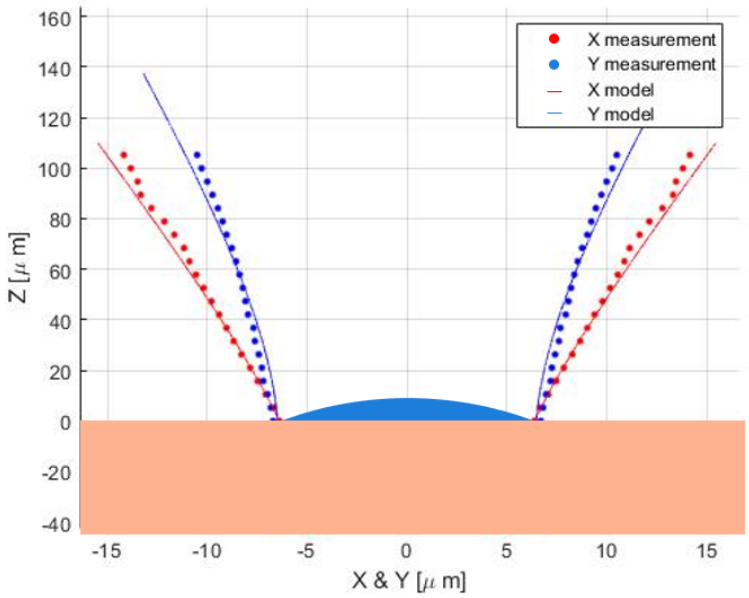

Figure 6.5: The $1/e^2$ beam outline of the measured and the expected fiber output, in both the X- and Y-direction.

Next, the coupling of light between the angle polished fiber and a grating coupler was investigated. The PIC structure used for this purpose is depicted in figure 6.6. It consists of two 15x15µm grating couplers at each end, connected through their tapered waveguides and a single-mode waveguide in between.

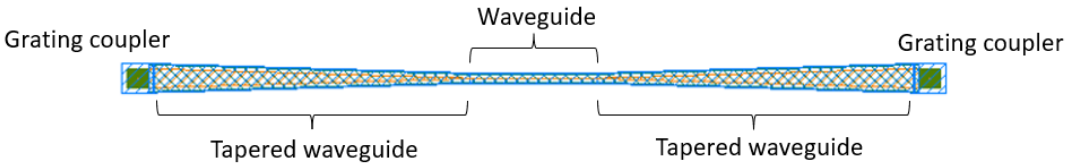

Figure 6.6: The PIC structure used for coupling efficiency and fiber alignment tolerance investigation.

First, the coupling efficiency was determined, which is defined as the transmission of light between the fiber and the central waveguide. Since only one fiber was at our disposal, the method that was used follows these steps:

1. The fiber output is captured with the IR imaging system.

   (a) The exposure time of the camera is set to a value at which no pixel saturation occurs.

(b) By summing all pixel intensities, the total intensity of the fiber output beam can be determined. Only pixels within the $1/e^2$ diameter of the spot are considered, removing dark current contributions as much as possible.

2. The fiber is then optimally coupled to one of the grating couplers, by following the appropriate fiber alignment steps of the alignment strategy in section 5.2. Figure 6.7 contains an image from the VIS imaging system of a correctly aligned fiber. The schematic in figure 6.8 shows the components and their location w.r.t. each other after this step. The transmission is presumed to be optimal after the fiber alignment steps.

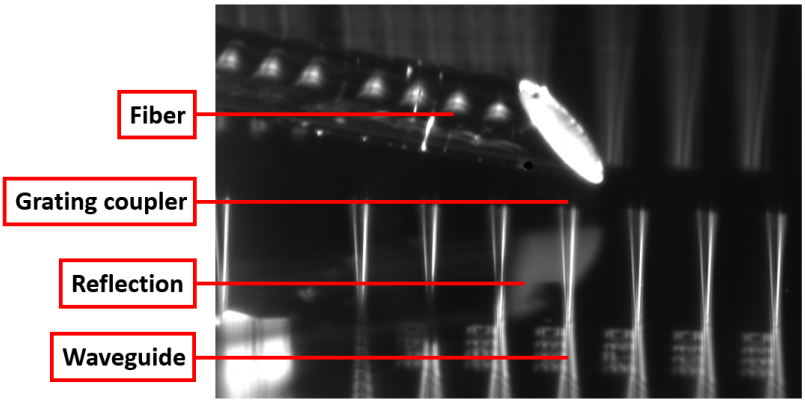

Figure 6.7: VIS camera system image of fiber that is correctly aligned to a grating coupler.

3. The output beam of the grating coupler at the other end is now captured by the IR imaging system

   (a) The pixel intensities of the grating output are summed for a total intensity of the grating output, while maintaining the exposure time of the camera that was used for the fiber output. Only pixels with a value of $1/e^2$ of the maximum are considered, removing dark current contributions as much as possible.

   (b) By dividing the total intensity of the grating output by the total intensity of the fiber output, the transmission over the complete system is calculated, resulting in a transmission T of 9.1%.

4. With a few assumptions, the coupling efficiency between the fiber and the waveguide can be calculated by decomposition of the transmissions in the system. By defining transmissions F, G and C in the system of figure 6.8, the equation for the total transmission T becomes:

$$T = FGGC \tag{6.1}$$

   (a) F is the unknown in the equation. It represents the mode overlap between the fiber output and the ideal field accepted by the grating coupler.

   (b) G is the transmission of the light captured by the grating coupler into the waveguide. It differs from PIC to PIC, depending strongly on the manufacturing process. G is expected to be in between 40% and 60%.

   (c) C is a result of the losses in the imaging system and at the detector. Only the camera detector efficiency specified by the supplier is considered, resulting in a G of 85%

   (d) The waveguide losses in the small PIC structure are insignificant.

5. The coupling efficiency was defined as the transmission between fiber and waveguide, which is F multiplied by G. Implementing the values mentioned above, the estimated coupling efficiency FG becomes 21.4±3.6%.

The uncertainty in this estimation is rather high. The measurement could be improved by replacing the IR camera with another fiber, removing imaging system loss uncertainties and making the system symmetrical. However, at the time of performing this verification step, only one fiber was available. Another solution for improvement of the estimation would be the use of a photodiode with a power meter instead of the imaging system, as that would provide more accurate intensity measurements compared to the IR camera. Despite the uncertainty in the estimation, the coupling efficiency is sufficient for coupling light to and from the PIC alignment sensor during an alignment marker scan.

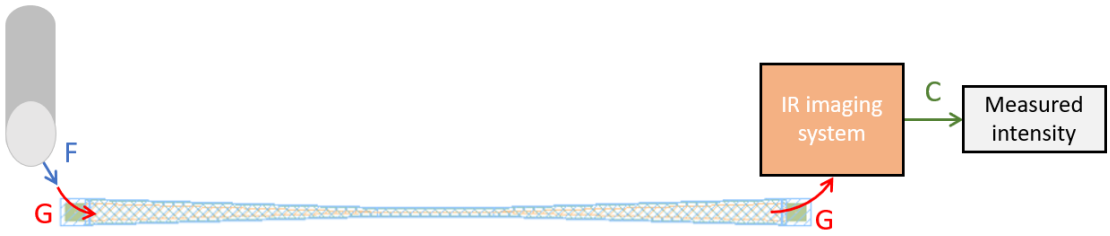

Figure 6.8: Schematic of system components and their transmissions involved in the coupling efficiency estimation method.

With the fiber still in its presumed optimal position and the IR camera focused on the grating at the other end like in figure 6.8, the alignment tolerances between fiber and grating coupler were examined. This was carried out by adjusting the fiber in several degrees of freedom w.r.t. the grating coupler, while monitoring the output intensity of the other grating coupler at the IR camera detector. All three manual translation stages of the fiber coupling stage configuration contain adjustment screws with 1 µm scale increments. The rotation mechanism responsible for rotating the fiber over its propagation axis is not equipped with a scale. By adjusting this rotation mechanism, the optimal position can be found for maximum transmission, but the orientation can not be quantified correctly. That is why measurements on the fiber alignment tolerances have only been conducted in the translational degrees of freedom. A schematic of the angle polished fiber with the coordinate system used is provided in 6.9.

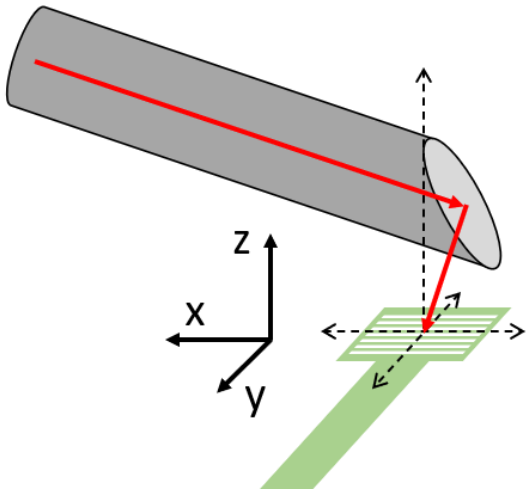

Figure 6.9: Schematic of fiber position w.r.t. the grating coupler. The alignment tolerances are determined in the X-, Y- and Z-direction.

The graphs of the normalized intensities as a result of fiber deviations from its initial position, are presented in figure 6.11. For the X- and Y-translations, steps of 1 µm were applied. In the Z-direction, 2 µm steps were applied. The error margin in these translations is 0.5 µm, as a result of the 1 µm scale increments. The uncertainty in the intensity is a consequence of light that is not captured by the grating and creates unwanted reflections reaching the IR camera detector. This uncertainty was determined by comparing the total intensity of an image with the laser source turned off (noise), with the total intensity of an image with the laser turned on, while the fiber was misaligned and its output was incident just outside the gratings. The difference

between the noise and the reflections at the camera detector was chosen as the error margin. The alignment tolerances in the X- and Y-direction differ from each other, because of the elliptical fiber output profile, and because the grating coupler behaves differently in these directions. The image in figure 6.10 of the output of the grating coupler at the other side of the waveguide shows this difference in behaviour. The grating coupler output intensity profile is approximately uniform over the X-direction, but emits an exponential profile in the Y-direction according to equation 1.3. Due to reciprocity, this coupling behaviour is similar at the input grating. It results in a tighter fiber alignment tolerance over the Y-direction compared to the X-direction.

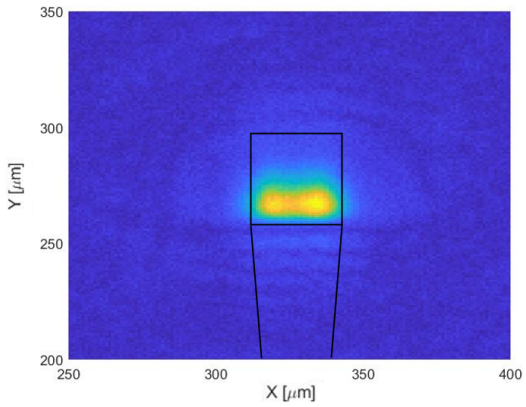

Figure 6.10: 2D intensity profile of grating coupler output at $Z = 10\,\mu m$.

Another observation from figure 6.11 is that in the X-direction, the intensity drops faster in the positive direction compared to the negative direction. This could originate from the rotational error ϵ around the Y-axis depicted in figure 6.4. In the right graph of figure 6.11, the intensity over the estimated distance between the fiber and the grating in the Z-direction is depicted. The distance is defined by the distance between the cladding-to-air interface and the grating coupler. This distance of the data points was estimated by fitting a Gaussian profile through the data points, and then shifting the profile and points over the horizontal axis until the center of the Gaussian was located at 0 µm. The assumption that this alignment tolerance profile resembles an approximate Gaussian, arised from previous research [14]. The flattening of the curve close to the grating could be attributed to the low divergence of the fiber output. The shortest distance of the series (presumably 22 µm) belongs to the fiber position in the picture of figure 6.7. By roughly comparing the distance between fiber and grating to known dimensions in the picture, it is indeed approximately 25 µm. A flaw in the alignment tolerance measurement over the Z-direction, is that only translation in this degree of freedom was applied. Because of the AoI of the grating, the Z-direction is not coincident with the fiber output propagation axis. When translating over the Z-direction, the spot also moves over the grating in the Y-direction (and X-direction as a result of error ϵ in fig. 6.4). Thus, the experiment would improve if after every translation step in the Z-direction, the output intensity at the other grating is maximized by translating the fiber over the X- and Y-direction.

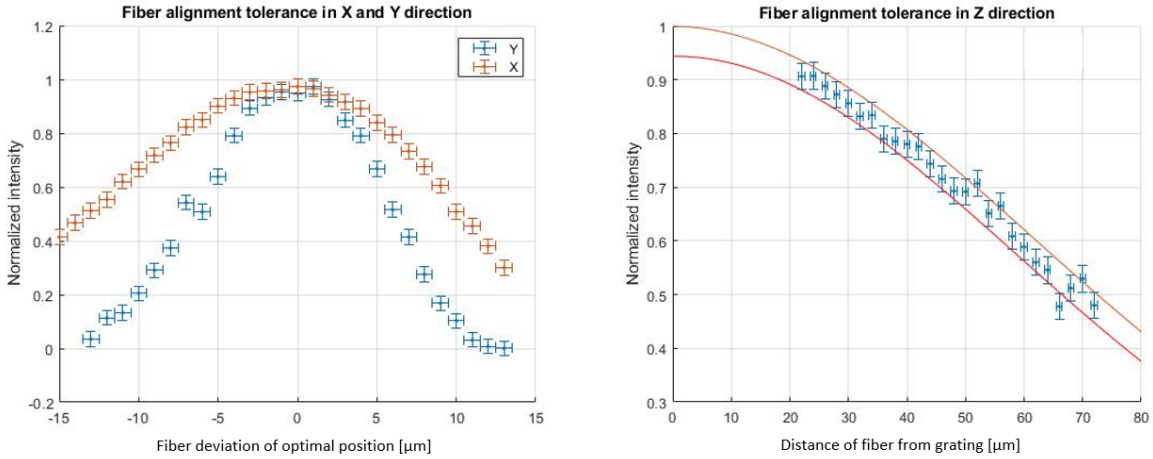

Figure 6.11: The fiber alignment tolerances. Left: normalized intensity at output grating over in the X and Y fiber deviations. Right: normalized intensity at output grating as function of Z-distance between fiber and input grating.

6.3. Alignment marker scanning error motions

During chapter 5 the sensitivity of the repeatability of the alignment marker scan to error motion variations over Ry and Rz was elaborated on. Their expected sensitivities were 40 nm/mrad and 15 nm/mrad respectively. In order to verify a repeatability below the required ±5 nm, the variation of these two error motions was investigated. The method and the results are described in this section.

The method makes use of the concept depicted in figure 6.12. A collimated light beam is incident on a mirror that is mounted to the wafer sample scanning stage (X-direction), which reflects the light to a relatively faraway plane at a distance D. With a rotation Ry of the scanning stage and thus of the mirror, the spot location at the that plane will shift over the Z-direction with

$$\Delta z = 2 * Ry * D \tag{6.2}$$

Similarly, a rotation Rz will result in a shift Δy of the spot. By measuring the shift of the spot, the rotation of the scanning stage can be determined. In the setup, the mirror plane is not perfectly aligned to the scanning direction. The incoming and outgoing beam at the mirror are also not coincident with the normal of the mirror. It implies that the spot will shift over the Y- and Z-direction during a scan in the X-direction, even in the absence of rotations Ry and Rz. However, since we are interested in the variation of the rotations, the variation of the shift over the two axes between a series of scans is important.

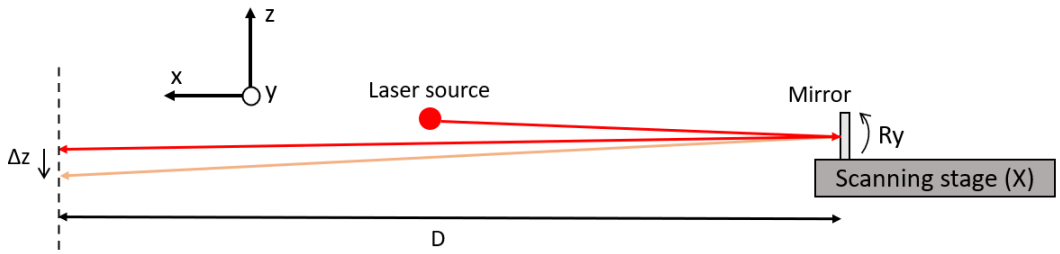

Figure 6.12: Schematic of setup for error motion measurements.

Figure 6.13 contains pictures of the setup and the components that were used for these measurements. Light from a 635 nm wavelength laser source is collimated and directed to a mirror that is mounted to the wafer sample X-stage. The reflected beam is eventually captured by the VIS imaging system, which is also used for fiber and probe alignment (section 5.1.7). The beam waist of the collimated beam is approximately 3.5 mm. With an FoV of the VIS imaging system of 0.78 mm, a focusing lens is needed in between the mirror and the imaging system to reduce the spot size. Distance D between the mirror and the lens is 1 m.

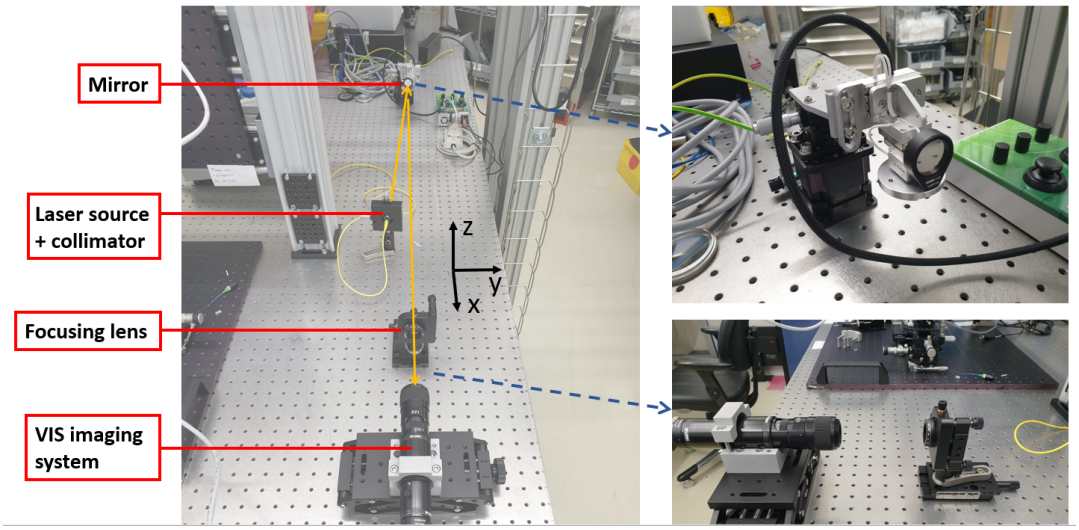

Figure 6.13: Pictures of setup for error motion measurements. On the left the complete setup. The wafer sample stage configuration with mirror in the top right corner. The VIS imaging system and focusing lens in the bottom right corner.

The position of the imaging system relative to the focusing lens is schematically depicted in figure 6.14. The focal length F of the lens is 30 mm, resulting in a spot size in the focal plane of 11 µm. The plane at the working distance WD of the imaging system is not coincident with the focal plane of the lens, with a separation of Δx. This way, the spot size w of 3.5 mm is reduced, while still ensuring a measureable shift in the image. The shift of the spot measured by the camera detector Δz_i relates to a shift of the collimated beam before the lens Δz_o according to:

$$\Delta z_i = \Delta z_o * \frac{\Delta x}{F}, \qquad \text{with} \quad \Delta z_o = 2 * Ry * D \tag{6.3}$$

The larger the distance Δx is chosen, the higher the Ry measurement resolution becomes, as a consequence of the constant spatial resolution of the imaging system. A larger Δx also leads to a larger spot size, which must remain within the FoV of the imaging system, taking into account the spot movement during a scan as well. A distance Δx of 10 mm was selected. The resulting spot size captured by the camera is approximately 200 µm. The Ry measurement resolution is then obtained by solving equation 6.3 for Ry, entering the imaging system spatial resolution of 0.25 µm for Δz_i. The smallest measurable rotation Ry becomes 0.75 µrad. For a rotation Rz of the scanning stage and thus a spot shift in the Y-direction, the same method applies.

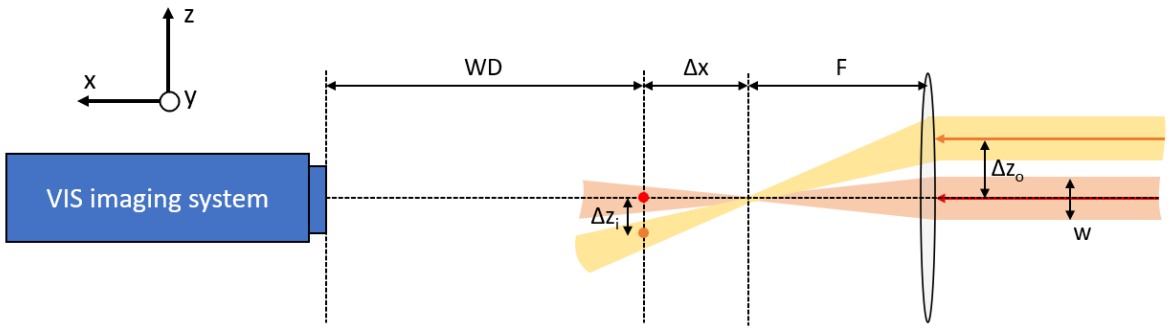

Figure 6.14: Schematic of VIS imaging system and lens, visualising spot size reduction and the relation between initial spot shift Δz_o and measured spot shift Δz_i. WD is the working distance of the imaging system. F is the focal length of the lens. Δx is the defocus chosen for a shift of the spot.

Knowing the relation between spot shifts in the camera image and the rotations over Ry and Rz of the scanning stage, a measurement could be conducted. Three scans were performed over a range of 10 mm, capturing spots on the camera detector with scanning stage steps of 0.5 mm. Figure 6.15 shows two graphs: on the left, the Z-location of the spot on the detector is plotted for each scanning stage location; on the right,

the same is done with the Y-location of the spot. To recover the variation of the spot locations, and thus the variation of the error motions in Ry and Rz, the difference of each point in Z and Y w.r.t. to the mean of the three data points at a particular scanning stage location was calculated. The 2σ standard deviation of these differences is 6.0 µm in the Z-direction and 8.3 µm in the Y-direction. Through the relation in equation 6.3, these translational variations correspond to rotational variations 18 µrad in Ry and 25 µm in Rz. The graphs show that the rotational error motions are rather arbitrary per scanning stage location over the 10 mm scanning range, which would have an insignificant effect on the repeatability. Assuming that the error motions could occur with a constant value over an alignment mark and with altering extremes per alignment mark, an estimation of the influence on the repeatability can be made. Multiplying the error motions with their repeatability sensitivities derived in section 5.3, results in a combined repeatability contribution of ±1.1 nm. Behaviour of the error motions that was not examined, but that would affect the repeatability, is periodic behaviour with a period equal to a harmonic of alignment signal period (1.6 µm). The explanation for this contribution corresponds to the description of the hypothetical periodic error contribution of the displacement sensor in section 3.2. Such periodic behaviour of the error motions is not likely to occur and its verification was not prioritised.

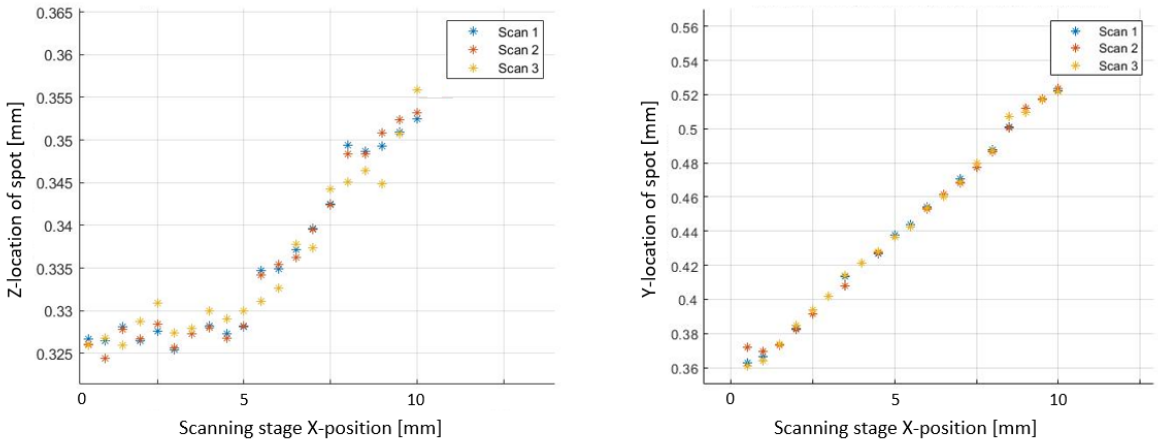

Figure 6.15: Graphs of the spot location on the detector of the VIS imaging system over the scanning stage position. Z-location on the left, Y-location on the right.

7
Conclusion & recommendations

In this report, the development of an experimental setup for photonic integrated circuits (PIC's) has been presented. The setup must contribute to the feasibility study on PIC alignment sensors for ASML lithography machines. To begin with, the requirements of the setup were defined by identifying and quantifying the crucial behaviour of the PIC alignment sensor that was designed by J.P. de Graaf [13]. These requirements were categorised into three groups: grating output characterization, alignment mark scanning, and signal insertion and extraction. The categorization is also applied in the structure of the conclusion. In section 7.2, recommendations concerning experimental setup improvements are addressed and possible future research on photonic integration is proposed, following from the experiences gained during this thesis project.

7.1. Conclusion

First, the conclusions regarding the characterization of the output of the emitting and capturing gratings are treated. Acquisition of their 2D beam intensity profiles at different locations will provide more insight in grating design properties. The most important requirements and their related performances are listed in table 7.1. The intensity profiles emitted by the gratings can be imaged by a camera-based infrared imaging system, with its focal plane parallel to the PIC surface. The spatial resolution of the system is 0.3 µm, which is below the required value (table 7.1). The field of view (FoV) is 192 µm × 154 µm and thus a spot diameter higher than the required 100 µm can be measured. With a numerical aperture of 0.65, the output angles of all gratings on the PIC are covered (30° maximum from the capturing gratings), without having to rotate the imaging system.

The imaging system can be positioned with respect to the PIC in the Z-direction with a motorized stage. Over its 25 mm range, it maintains a tip/tilt uncertainty of ±4.5 mrad w.r.t. the normal of the PIC. The range exceeds the required 7 mm, because the imaging system is also used in the alignment of the wafer sample. Over an exclusive Z-translation of ±125 µm around the PIC focal distance, the beams emitted from the PIC are retained within the FoV of the imaging system and a 3D representation of the beam can be retrieved by combining the 2D intensity profiles imaged at different Z-locations. The required accuracy for the Z-distance measurement between an intensity profile above the PIC and the PIC plane itself is ±25 µm (table 7.1). The calculated accuracy performance is ±6 µm, which is elaborated on in chapter 5. The verified performance is ±18.8 µm and shows a repeatability of ±1.9 µm (2σ). PIC's over the entire wafer can be reached by the imaging system, through the PIC chuck translation stages in combination with the imaging system translation stages.

The subsequent setup category is the alignment marker scan. The scan of a wafer sample over the PIC is conducted by the actuation of a translation stage with an integrated high precision displacement sensor, after alignment with a 6 degree of freedom stage configuration. The performance of the PIC alignment sensor will be quantified by the repeatability of the distance measurement between two standard markers, 10 mm apart from each other. As stated in the alignment strategy (section 5.2), the wafer sample is first coarsely aligned to the PIC (within the values in table 5.3), using the infrared imaging system, after which it is finely aligned by maximizing the transmission over a single capturing grating. The process is expected to satisfy the installation requirement of 30 minutes. The repeatability of the distance measurement between the two markers was approached by regarding the PIC alignment sensor working principle equal to the Athena alignment sensor working principle. This repeatability is influenced by three main factors: the error motions of the scanning stage, the SNR of the alignment signal and the error properties of the displacement sensor. The displacement sensor properties were proven to have an insignificant impact. The SNR of 310 of the alignment signal also does not significantly contribute to the repeatability. The Ry and Rz error motions do affect the repeatability. Their expected sensitivities are 40 nm/mrad and 15 nm/mrad respectively, assuming linear behaviour due

to the small angle variations. Using the error motions of the scanning stage specified by the manufacturer, the calculated repeatability becomes ±4.3 nm (table 7.1). However, this would be the result of a worst case scenario of the error motion behaviour (see sections 5.1.2 and 5.3). The error motions in Ry and Rx were investigated with the test setup described in section 6.3, resulting in a 2σ rotational deviation, or variation of ±18 µrad in Ry and ±25 µrad in Rz of the wafer sample during a scan over 10 mm. In the unlikely worst case scenario, this could lead to a repeatability contribution of 1.1 nm.

Lastly, inserting and extracting both optical and electrical signals to and from the PIC is enabled with the experimental setup. Electrical voltages and currents are applied over active components on the PIC via 8 coaxial probes. They allow for the transfer of radio frequency signals, which is not required for components on the PIC alignment sensor, but which does provide versatility for future research. The optical signals are coupled in and out of the PIC through the use of polarization maintaining, single-mode, angle polished fibers (APF). Polarization maintaining fiber supports either TE or TM linearly polarized light. Switching between can be achieved with a polarization converter, thus the polarization requirement is met. The fiber stage configuration allows for adjustments of the angle of incidence between fiber output and grating coupler, by rotating the fiber over its axes. It makes switching between gratings of different designs a time efficient process, over an Angle of Incidence (AoI) range that satisfies the requirement (table 7.1).

The coupling efficiency from fiber to waveguide was not among the initial requirements, but it is included in table 7.1, since it influences the SNR and thus the repeatability of the marker scan. Both an estimation and verification of the coupling efficiency of the angle polished fiber was necessary. The expected coupling efficiency from fiber to waveguide via grating couplers, deduced from literature, was 18.5%. The measured and calculated coupling efficiency is 21.4±3.6%. The wavelength of the laser source has a tunable range of 1260 nm to 1680 nm, greater than the necessary ±15 nm around the PIC design wavelength. This extended tuning range facilitated experiments with interesting results, which is elaborated on in section 7.2. The spectral bandwidth of the laser is 1.6×10^{-3} pm. In combination with a wavelength accuracy of 15 pm, the gratings can be characterized with high precision and the optimal working wavelength of the PIC alignment sensor can be identified.

Due to a delay in the manufacturing process of the first PIC alignment, it was not delivered in time, which has withheld us to some extent from verifying the alignment strategy and from performing an alignment mark scan. However, the experimental setup satisfies all requirements and the project goal has been realized, by completing the design and construction of an experimental setup for photonic integrated circuit alignment sensors.

			Performance	
Category	**Property**	**Requirement**	**Calculated/Specified**	**Verified**
Grating output char.	Spatial resolution	< 2 µm	0.3 µm	-
	Z travel	> 7 mm	25 mm	-
	Z accuracy	±25 µm	±6 µm	±19 µm
Alignment marker scan	Scan travel (X)	> 10 mm	16 mm	-
	Repeatability	< ±5 nm	< ±4.3 nm	< ±1.1 nm
Signal insertion & extraction	Wavelength	1535-1565 nm	1260-1680 nm	-
	AoI	5° – 15°	0° – 18°	-
	APF coupling efficiency	-	18.7%	21.4±3.6%

Table 7.1: Overview of important requirements and their calculated or specified and verified performance

7.2. Recommendations

A first recommendation for improvement of the setup concerns the alignment strategy of the wafer sample to the PIC. It consists of multiple steps, all manually performed, and the process is expected to take 30 minutes. Part, or all of the steps could be automated, speeding up the process and increasing reproducibility. However, one should consider the extent of automation in light of time efficiency as a trade-off. The intention of the experimental setup is to study the feasibility of a PIC design. If its performance is remotely promising after a

series of scans in the setup, the next step is testing in the actual alignment stage of a lithography machine. As a result, one PIC does not have to endure the alignment process endlessly, but most likely only a few times, possibly making the effort of full automation a redundant and time consuming activity.

The experimental setup was in part designed around the assumption that the PIC alignment sensor behaves similarly to ASML's Athena alignment sensor. Although this approach is valid for an estimate of the performance in lithography machines, the differences in working principle must not be forgotten and taken into account in future PIC design. In Athena for example, a marker rotation over the Y-axis alone (as described in section 3.2.2) has no influence on the marker position measurement because the optical path lengths of the positive and negative diffraction order to the reference grating do not change. In the current PIC alignment sensor that is not the case between the marker and capturing gratings with a marker Ry rotation: one diffraction order is incident on its capturing grating further away from the waveguide and the other order is incident closer to its waveguide inlet, changing the path lengths in opposite directions. Since this working principle difference is also concerned with the primary contrast between the two sensors, namely grating couplers, the question remains what the resulting phases are in the waveguides after these small wavefront alterations. Secondly, there is the spectral bandwidth applied in both alignment sensors. Athena makes use of a light source with a bandwidth of around 10 nm, in order to avoid speckle, which has a significant influence on the overlay error. Speckle is the result of unwanted reflections in the surroundings in combination with the long coherence length that is paired with a short spectral bandwidth. For the PIC alignment sensor, or at least the version that will be studied first, a short spectral bandwidth might be necessary, because the output angle of grating couplers is sensitive to wavelength. However, the directionality of the gratings could also act as a filter: scattered light from unwanted reflections is not, or to a lower extend, coupled into the waveguide.

Another recommendation for setup improvement concerns the alignment between fiber and grating. For the measurements to be conducted on the PIC alignment sensor, the fiber is aligned by maximizing the output power at the other end, meaning that the exact orientation of the fiber relative to the grating is not known. It is only important that light is sufficiently coupled. We have seen that, for this PIC alignment sensor, the coupling efficiency is satisfactory for a useful alignment signal at the detector. However, for future research on photonic integration, it could meaningful to study the coupling behaviour between fiber and grating in more detail. Knowing the fiber orientation more accurately would be necessary for this. The experimental setup currently lacks read-out resolutions. The translational fiber stages could be improved by replacing the micrometer screws with piezo actuators. The component responsible for rotating the fiber over its propagation axis does not have an incorporated scale, which is something that should be added within a similar replacing component.

Lastly, a finding is shared that is not directly relevant to the project goal. It does demonstrate the capabilities of the setup and might be a subject for thought, being a phenomenon in photonic integration that diverges from the expected. An experiment was conducted in which the output of several fiber grating couplers was imaged as a function of wavelength over a range between 1525 nm and 1575 nm. The gratings were part of the same tapered waveguide structures described in section 6, displayed in figure **??**. The output of the uniform grating was expected to have an exponential profile (see equation 1.3) over the Y-axis and should be symmetrical over the X-axis. The results indeed show an exponential profile, but the symmetry over the X-axis changes with the wavelength. In the figure below, a top view of the intensity profiles corresponding to three different wavelengths is depicted.

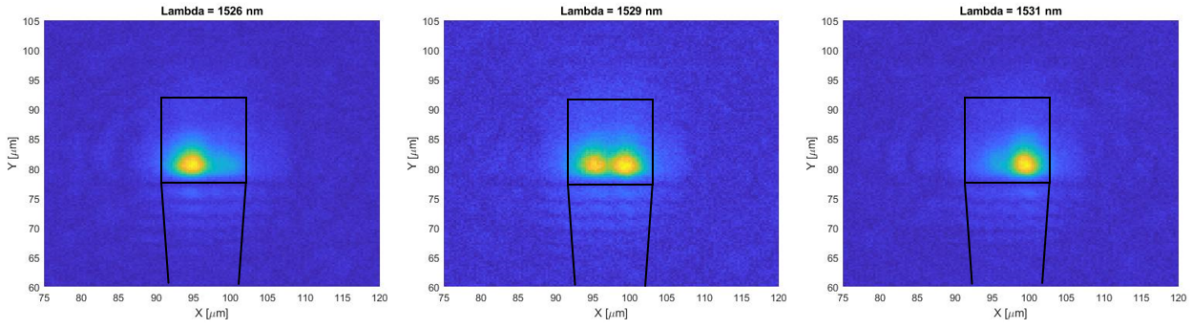

Figure 7.1: Top view intensity profiles of grating coupler (15 µm × 15 µm, black square) output with different input wavelengths. Tapered waveguide comes from below.

Multiple spots or asymmetry in the X-direction in the output profile suggests the induction of higher-order modes somewhere in the structure, apart from the fundamental mode. This should not be the case, since the waveguide only allows for a single mode, and the tapered waveguide expanding the mode to the grating is designed to be adiabatic. It is likely that a defect in the taper is the cause, but pinpointing this defect is complex and out of the scope of this project. Either way, it could help in the characterization of the output of the larger gratings on the PIC alignment sensor, whose performance is more vulnerable to certain defects in the structure.

With the different subjects in the recommendations, an attempt is made to demonstrate that the setup is not only qualified to characterize gratings and perform alignment mark scans. With improvements, it could also aid in the research of more fundamental subjects within integrated optics.

A

PIC alignment sensor specifications

This appendix consists of an overview of the relevant PIC specifications. In figure A.1 the complete PIC system flow is depicted, with indexing corresponding to the subsystem locations in the top view of the PIC in figure A.2. Blue blocks are components on the PIC and the orange block is a marker grating on the wafer sample. The transfer of optical signals through the PIC via waveguides is represented by the continuous arrows and transmission through air by the dashed arrows. The expected transmissions of the PIC components, including angle polished fibers (APF), are listed in A.1.

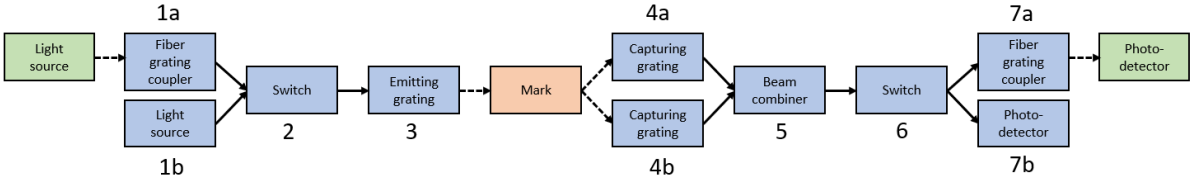

Figure A.1: PIC system flow schematic. On-chip components indicated with blue.

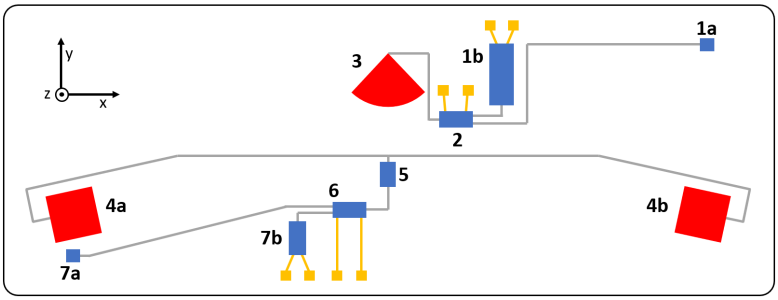

Figure A.2: Top view of the PIC alignment sensor (4 mm × 20 mm), fifth order system.

Component	Name	Loss (dB)	Transmission (%)
1a	Input grating coupler (APF)	7.2	19
2	Switch	1.5	71
3	Emitting grating	11	8
-	Alignment marker 5^{th} order	43	0.5
4a	Capturing grating	11	8
	Gap coupler	0.5	90
5	beam combiner	0.6	87
6	Switch	1.5	71
7a	Output grating coupler (APF)	7.2	19
-	Waveguides	1.7	68
-	**Total**	**85.2 dB**	$3.1 * 10^{-5}$**%**

Table A.1: Passive/optical PIC operation transmission.

B

Marker alignment tolerances

In this appendix, the calculation of the tolerances of an alignment marker with respect to the PIC alignment sensor is expanded on. First, the formulas behind the spot locations and sizes are explained. From there, a position or orientation alteration of the alignment mark can be translated to a shift of the spots with respect to their nominal positions on the capturing gratings. The limits of these shifts that we allow, form the tolerances on the wafer sample to PIC alignment.

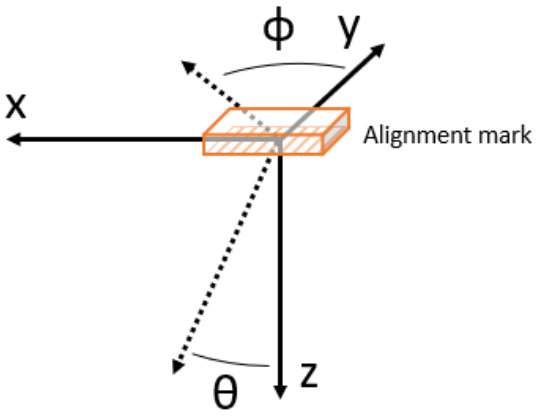

Figure B.1: Coordinate system with respect to alignment mark (grating on bottom side).

B.1. Spot location and size calculation

The coordinate system used for the conical diffraction and spot location calculations is displayed in figure B.1. X and Y are in plane of the alignment mark, where z is defined out of the grating. The angles are defined by using θ for all out of plane angles and ϕ for all in plane angles. The directions of the reflected diffraction orders of the alignment marker (placed at (0,0,0) in the coordinate system) and thus the locations of the spots on the PIC are calculated with the conical diffraction formulas, because of the oblique incidence angle on the marker grating from the emitting grating beam. The X and Y spot coordinates of the m^{th} diffraction order from the alignment marker on the PIC (where PIC plane and marker plane are parallel) at a Z-distance z_1, become a function of the incidence angles at the marker grating (θ_i and ϕ_i) as follows (I. Setija, personal communication, December 2020 and [31]):

$$x_1 = z_1 \frac{\sin(\theta_i)\sin(\phi_i) - \frac{m\lambda_0}{n\Lambda}}{\sqrt{1-(\sin(\theta_i)\cos(\phi_i) - \frac{m\lambda_0}{n\Lambda})^2 - (\sin(\theta_i)\sin(\phi_i))^2}} \tag{B.1}$$

$$y_1 = z_1 \frac{\sin(\theta_i)\sin(\phi_i)}{\sqrt{1-(\sin(\theta_i)\cos(\phi_i) - \frac{m\lambda_0}{n\Lambda})^2 - (\sin(\theta_i)\sin(\phi_i))^2}} \tag{B.2}$$

With λ_0 the wavelength in vacuum, n the refractive index of air and Λ the alignment marker pitch. In an ideal, nominal case, the beam from the emitting grating is incident on the marker along the grating lines, resulting in an angle ϕ of 90. With the relevant angles, positions and distances known, the spot sizes on the PIC

can be calculated. The beam diameter on the marker grating $2w_{0(M)}$ is designed to be 40 µm (circular) in the marker plane ($1/e^2$ of maximum), implying that both the incoming beam and the outgoing diffraction orders are elliptical along their propagation direction. The major axis of a diffracted beam just after the marker has a diameter ($2w_{0,b}$) equal to the spot on the marker ($2w_{0(M)}$). Their minor axis diameter is smaller, which is shown in figure B.2. ϕ_o in the coordinate system is the output angle over the Z-axis of a diffracted beam. This minor axis beam diameter ($2w_{0,a}$) then follows from:

$$2w_{0,a} = \cos(\theta_o) 2w_{0(M)} \tag{B.3}$$

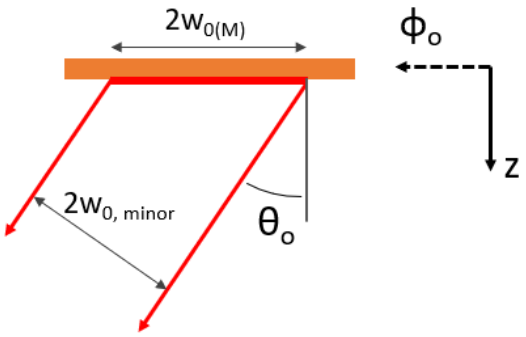

Figure B.2: Schematic of diffraction order minor diameter $2w_{0,a}$ under output angles θ_o and ϕ_o. Marker is depicted in orange.

The beam diameters along the propagation direction at the capturing grating $2w_{CG,a}$ and $2w_{CG,b}$, for both initial diameters $2w_{0,a}$ and $2w_{0,b}$ respectively, are calculated with the Gaussian propagation equation:

$$2w_{CG,a/b} = 2w_{0,a/b}\sqrt{1+(\frac{P}{z_0})^2} \tag{B.4}$$

Where P is the propagation distance between alignment marker and capturing grating, with Rayleigh length z_R:

$$z_R = \frac{\pi w_{0,a/b}^2}{\lambda} \tag{B.5}$$

For the beam diameter on the capturing grating orthogonal over its grating lines ($2w_{CG,a(\theta)}$), in the plane of the PIC, angle θ_o is applied once more:

$$2w_{CG,a(\theta)} = \frac{2w_{(CG,a)}}{\cos(\theta_o)} \tag{B.6}$$

The beam diameter on the capturing grating in the other direction remains equal to the diameter $2w_{CG,b}$ over the propagation direction. In the nominal position and orientation of the wafer sample, a spot of the fifth diffraction order from the marker is incident on the capturing grating as shown in figure B.3. An important feature that will be used for the alignment tolerances of the wafer sample, is that the capturing gratings are larger than the spot.

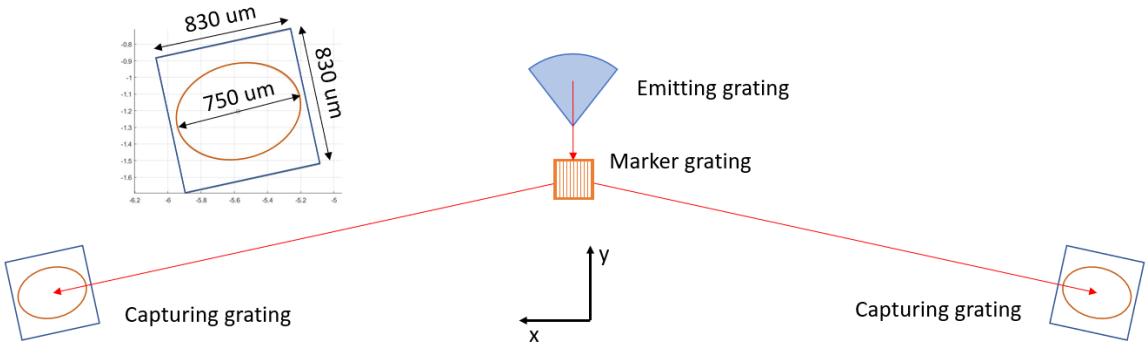

Figure B.3: Top view schematic of a marker and PIC alignment sensor system in nominal position, with spots relative to the capturing gratings.

B.2. Wafer sample alignment tolerances

A deviation in any of the three rotational degrees of freedom or a translation over the z-axis of the wafer sample will lead to a change of location and size of the spots relative to the capturing gratings on the PIC. The tolerances of these deviations are defined at the point where the resulting spots are not completely incident on the capturing gratings. The method for calculating the transformation of a spot on the PIC is similar for the degrees of freedom mentioned and thus, only one will be demonstrated: a rotation ρ of the alignment mark around the X-axis. The process is depicted in figure B.4. First, the rotation is converted to new input angles ϕ_i and θ_i. For a rotation around the X-axis, ϕ_i remains constant and θ_i increases by ρ. The new angles are applied to the conical diffraction equations (B.1). It provides us with location $(x_1, y_1, z1)$ of a spot on the surface of the chip, which is depicted in the left schematic of the figure. The effect of conical diffraction has now been taken into account. However, we are interested in a rotation of the marker. The system, consisting of the incoming beam, alignment mark and outgoing beams, is in the wrong orientation. It must be rotated around the X-axis with angle $-\rho$ in order to retrieve the correct directionality of the incoming and outgoing beams, shown in the middle schematic of the figure. The spot location (x_2, y_2, z_2) is now just above the PIC and follows from the equation:

$$\begin{bmatrix} x_2 \\ y_2 \\ z_2 \end{bmatrix} = \begin{bmatrix} 1 & 0 & 0 \\ 0 & \cos(-\rho) & \sin(-\rho) \\ 0 & -\sin(-\rho) & \cos(-\rho) \end{bmatrix} \begin{bmatrix} x_1 \\ y_1 \\ z_1 \end{bmatrix} \tag{B.7}$$

Now we have obtained the correct orientation. The diffracted beam originates at $(0,0,0)$ and location (x_2, y_2, z_2) can be extended over its propagation direction to find the correct spot location (x_3, y_3, z_3) in the plane of the PIC ($z_3 = 10\,\text{mm}$). The spot size is deduced with the equations discussed in the previous section.

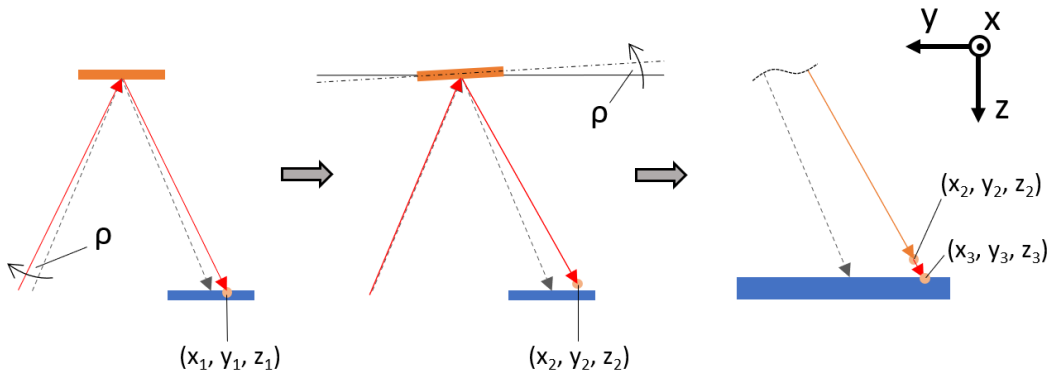

Figure B.4: Side view of method for spot shift calculation as a result of an alignment mark rotation over the X-axis (ρ). The dashed grey arrows are the nominal beam positions.

The maximum allowable rotation ρ around the X-axis for the diffraction orders to be completely incident on the capturing gratings is $\pm 6\,\text{mrad}$, which is illustrated by figure B.5. As mentioned, the tolerances for the

other three degrees of freedom (Ry, Rz and Z) are determined in a similar fashion. They are listed in the table below.

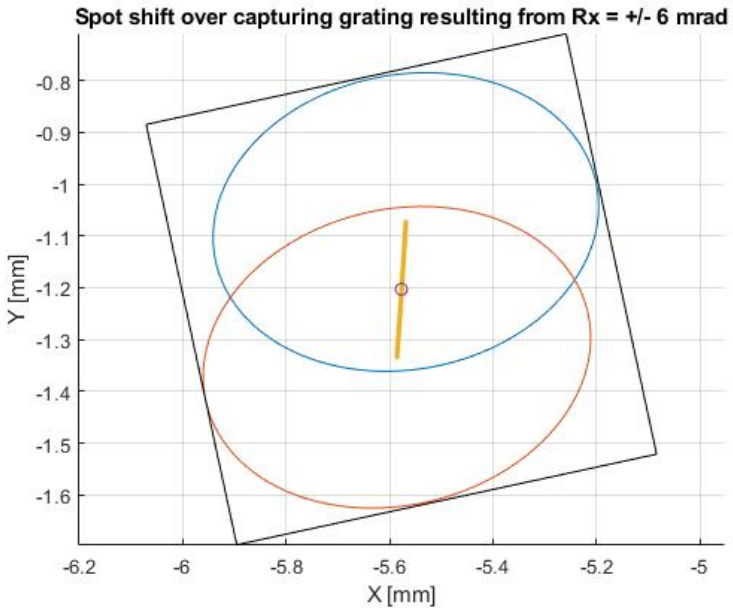

Figure B.5: Top view of spot shift of negative fifth diffraction order over the left capturing grating, as a result of a ±6 mrad rotation around the X-axis of the alignment marker.

Marker alignment tolerances

Rotation x	±6 mrad
Rotation y	±1.5 mrad
Rotation z	±20 mrad
Translation z	±70 µm

Table B.1: Alignment marker to PIC alignment tolerances around nominal position.

C
Angle polished fiber output model

The output of an angle polished fiber is estimated in the simplified model described in this appendix. The model was used to evaluate the information discovered in literature and for a comparison with the measured output. In section 6.2, the output beam data of an angle polished fiber is collected and compared to this model.

The path taken by the light from fiber core to grating in an angle polished fiber is proposed to occur in the following steps:

1. Reflection at polished face.
2. Gaussian propagation through the fiber cladding.
3. Refraction at the cladding to air interface.
4. Gaussian propagation through air.

The MFD (mode field diameter) of the fundamental mode travelling through the single mode fiber is 10.4 µm. The intensity profile of the fundamental mode is Gaussian and the MFD is defined at $1/e^2$ of the maximum intensity. After total internal reflection at the polished face, the light is directed into cladding with a certain angle, dependent on the polishing angle. The beam is no longer confined by the core and is expected to behave like a Gaussian beam, according to the Gaussian propagation formulas:

$$w(z_C) = \frac{\text{MFD}}{2}\sqrt{1+\left(\frac{z_C}{z_R}\right)^2} \tag{C.1}$$

With the Rayleigh length:

$$z_R = \frac{\pi\left(\frac{\text{MFD}}{2}\right)^2 n_{\text{clad}}}{\lambda_0} \tag{C.2}$$

Where n_{clad} is the index of the cladding material, z_C is the propagation axis through the cladding (see figure C.1) and λ_0 is the wavelength in vacuum. The cladding index of single-mode fiber is 1.444 and the core index is 1.449; refraction at the core to cladding interface is neglected. At the interface of cladding and air, refraction is taken into account and a distinction between the X- and Y-direction is made, since the difference in angle of incidence and surface shape. Figure C.1 depicts the effect in the X-direction and figure C.2 shows the refraction over the Y direction, all according to Snell's law, with incidence angles θ_1 and exit angle θ_2:

$$\theta_2 = \arcsin(\frac{n_{clad}}{n_{air}})\arcsin(\theta_1) \tag{C.3}$$

At the cladding-to-air interface, the incidence angle of the chief ray of the beam propagating through the cladding is retrieved. The exit angle of the beam through air follows from equation C.3. The same equation is applied to the outer diameter rays of the Gaussian beam, in the X-direction and in the Y-direction. The spot size and the divergence in air at the cladding-to-air interface are now known. The divergence in X-direction increases after refraction. In the Y-direction it decreases, with income angle α being smaller than β (fig. C.2), due to the lens-like behaviour of the cylindrical interface shape. With a known chief ray output angle, divergence and spot size, the Gaussian propagation for both planes (XZ and YZ) of the beam through air can be defined. There is only one possible Gaussian propagation function per plane that fits these known parameters. These Gaussian beams are fitted in both directions by manually searching for the remaining two fit

parameters: the spot size at focus and the location of the spot at focus along the propagation direction. Figure C.1 shows the beam propagation through the cladding in blue, and the manually positioned Gaussian beam through air in red. Its spot size at focus is located in the cladding and can be considered as the projection of the output beam.

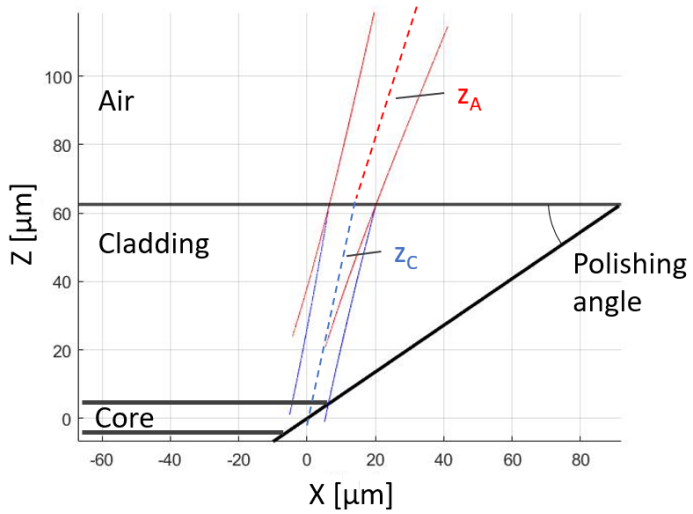

Figure C.1: Modelled light propagation of angle polished fiber in XZ-plane.

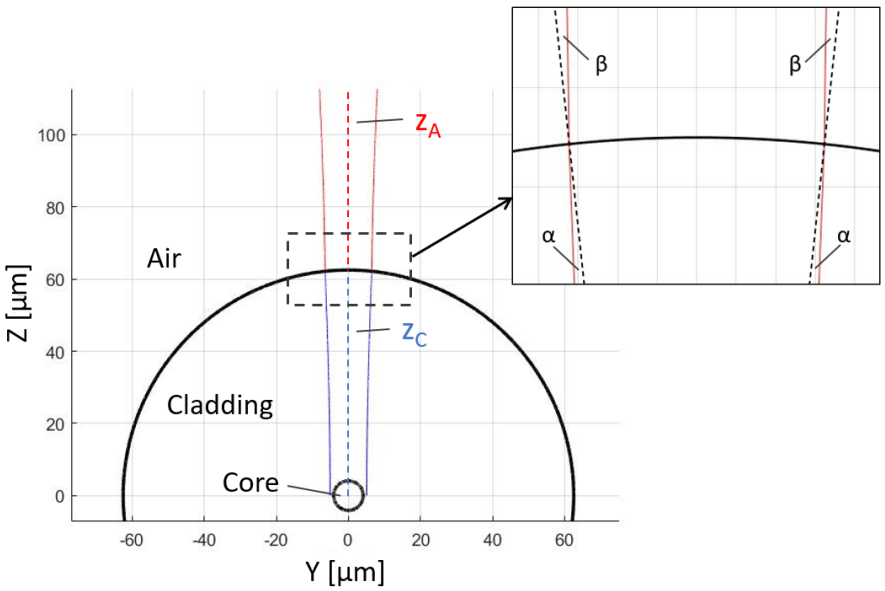

Figure C.2: Modelled light propagation of angle polished fiber in YZ-plane.

D

Experimental setup pictures

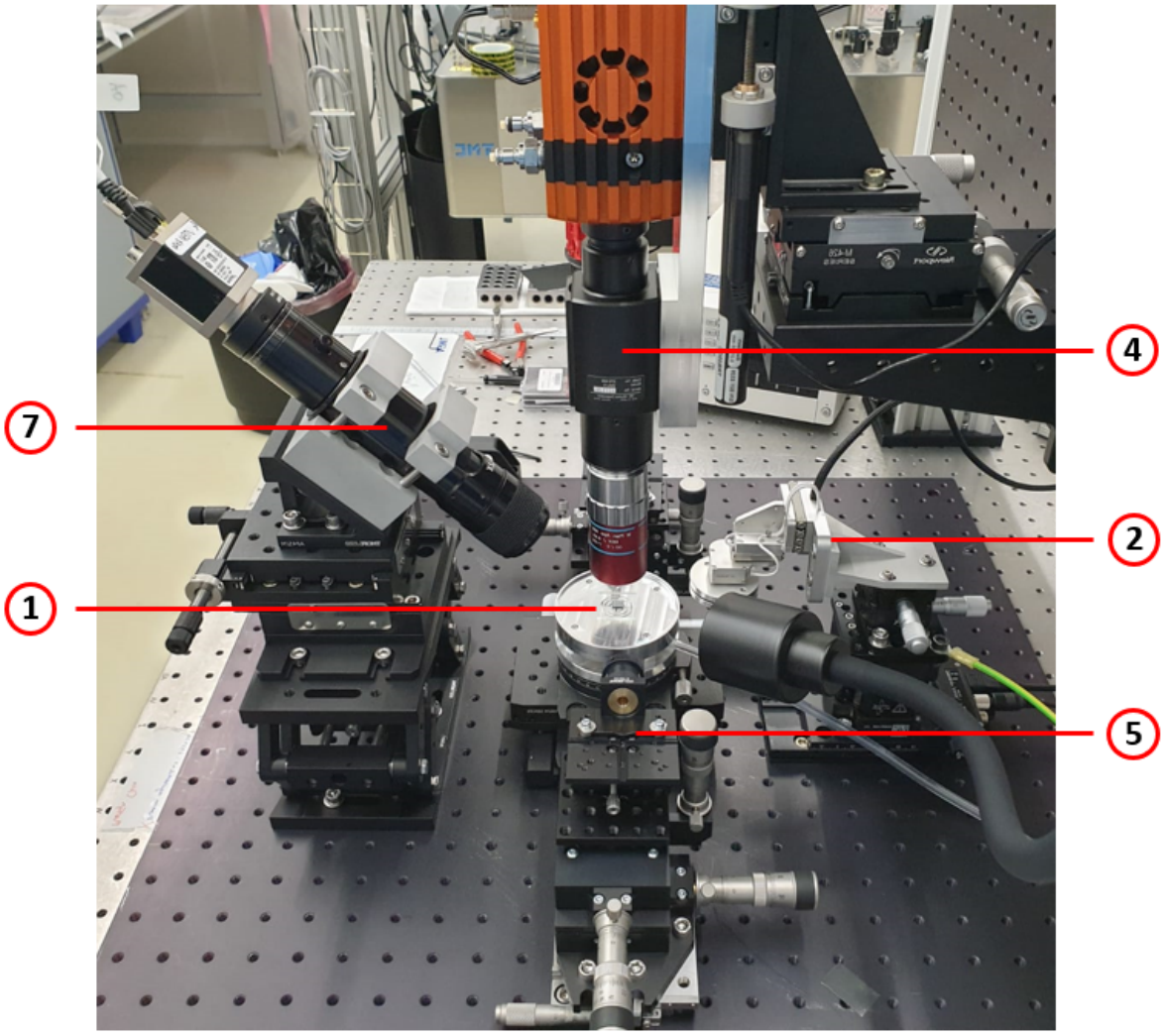

Figure D.1: Picture of experimental setup. Indexing corresponds to subsection numbering of section 5.1. 1: PIC chuck, 2: Wafer sample stage, 4: IR imaging system, 5: Fiber coupling, 7: VIS imaging system. The probe coupling subsystem is not present in the assembly, due to the delay of certain components.

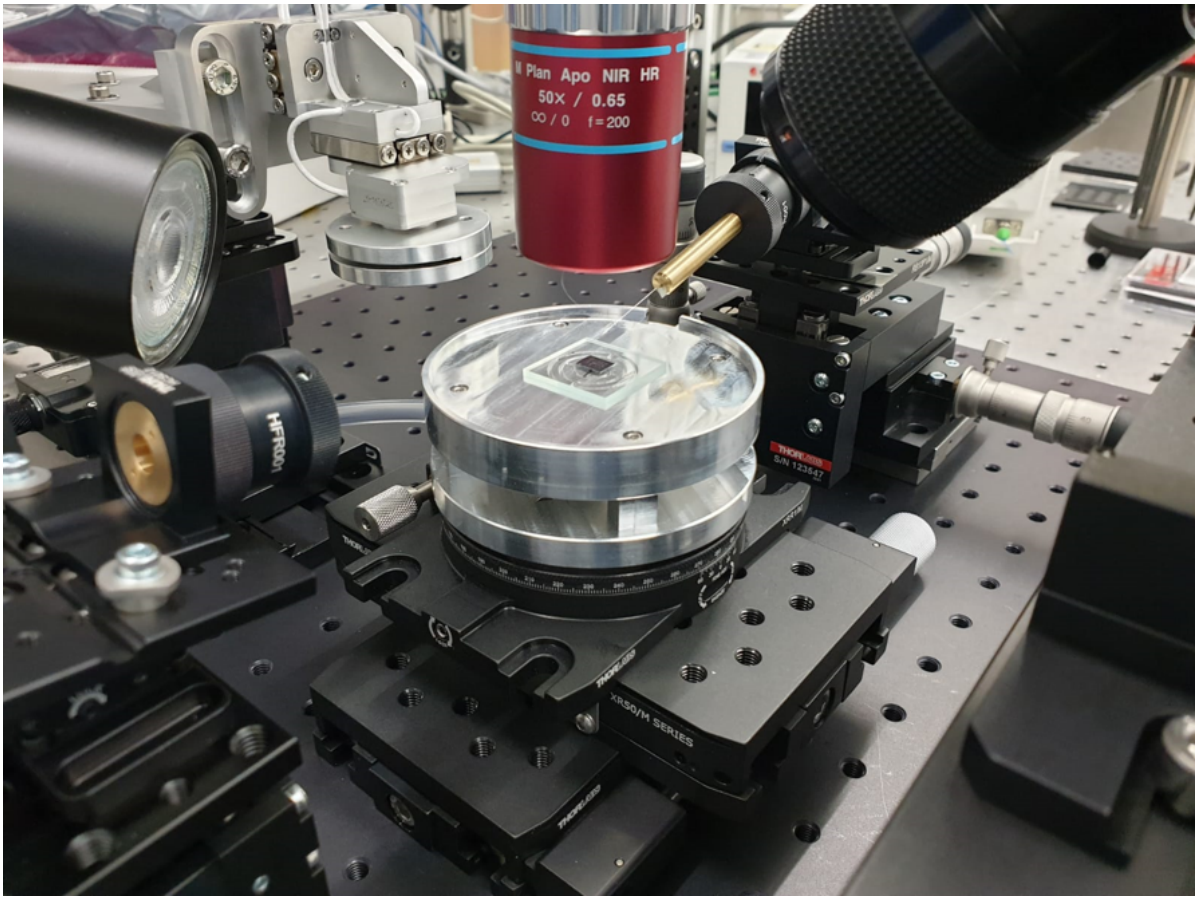

Figure D.2: Close up picture of PIC on chuck.

Bibliography

[1] New semiconductor technologies and applications. *https://irds.ieee.org/topics/new-semiconductor-technologies-and-applications*, 2021.

[2] Gordon Moore. Cramming more components onto integrated circuits (1965). *Ideas That Created the Future*, page 261–266, 2021.

[3] Boris Menchtchikov, Robert Socha, Chumeng Zheng, Sudharshanan Raghunathan, Leendertjan Karssemeijer, Irina Lyulina, Jonathan Lee, Igor Aarts, Krishanu Shome, Chris De Ruiter, and et al. Reduction in overlay error from mark asymmetry using simulation and alignment models. *Optical Microlithography XXXI*, 2018.

[4] A. Freise, A. Bunkowski, and R. Schnabel. Phase and alignment noise in grating interferometers. *New Journal of Physics*, 9:433–433, 2007.

[5] Robert G. Hunsperger. *Integrated Optics: theory and technology*. Springer, 2010.

[6] Stewart E. Miller. Integrated optics: An introduction. *Bell System Technical Journal*, 48(7):2059–2069, 1969.

[7] K. A. Williams, E. A. J. M. Bente, D. Heiss, Y. Jiao, K. Ławniczuk, X. J. M. Leijtens, J. J. G. M. Van Der Tol, and M. K. Smit. Inp photonic circuits using generic integration [invited]. *Photonics Research*, 3(5), 2015.

[8] F. Kish, V. Lal, and P. Evans. System-on-chip photonic integrated circuits. *IEEE Journal of Selected Topics in Quantum Electronics*, 24(1):1–20, 2018.

[9] J. J. G. M. van der Tol, Y. Jiao, J. P. Van Engelen, V. Pogoretskiy, A. A. Kashi, and K. Williams. Inp membrane on silicon (imos) photonics. *IEEE Journal of Quantum Electronics*, 56(1):1–7, 2020.

[10] Riccardo Marchetti, Cosimo Lacava, Lee Carroll, Kamil Gradkowski, and Paolo Minzioni. Coupling strategies for silicon photonics integrated chips [invited]. *Photonics Research*, 7(2):201, 2019.

[11] Shankar Kumar Selvaraja, Diedrik Vermeulen, Marc Schaekers, Erik Sleeckx, Wim Bogaerts, Gunther Roelkens, Pieter Dumon, Dries Van Thourhout, and Roel Baets. Highly efficient grating coupler between optical fiber and silicon photonic circuit. *Conference on Lasers and Electro-Optics/International Quantum Electronics Conference*, 2009.

[12] Li Yu, Lu Liu, Zhiping Zhou, and Xingjun Wang. High efficient vertical binary blazed grating coupler for chip level optical interconnections. *Cleo: 2014*, 2014.

[13] J.P. Graaf, I. Setija, K. Williams, and Y. Jiao. Integrated optical sensor for diffraction based wafer alignment. *Master thesis, Eindhoven University of Technology*, 2020.

[14] Dirk Taillaert, Frederik Van Laere, Melanie Ayre, Wim Bogaerts, Dries Van Thourhout, Peter Bienstman, and Roel Baets. Grating couplers for coupling between optical fibers and nanophotonic waveguides. *Japanese Journal of Applied Physics*, 45(8A):6071–6077, 2006.

[15] Alejandro Martínez, Pablo Sanchis, and Javier Martí. Mach–zehnder interferometers in photonic crystals. *Optical and Quantum Electronics*, 37(1-3):77–93, 2005.

[16] Carlos B. Roundy and Larry Green. Beam profiling monitors beam shaping. *Laser Beam Shaping VI*, 2005.

[17] Lawrence I. Green. Beam profiling at focus: essential for beam shaping. *Laser Beam Shaping IX*, 2008.

[18] J. R. Albani. *Structure and dynamics of macromolecules absorption and fluorescence studies*. Elsevier, 2004.

[19] Jonathan Creasey, John Mattos, and Glenn Tyrrell. Infrared camera mit phosphor coated ccd.

[20] Tara Martin, Robert Brubaker, Peter Dixon, Mari-Anne Gagliardi, and Tom Sudol. 640x512 ingaas focal plane array camera for visible and swir imaging. *Infrared Technology and Applications XXXI*, 2005.

[21] F. Niklaus, G. Stemme, J. Q. Lu, and R. J. Gutmann. Adhesive wafer bonding. *Journal of Applied Physics*, 99(3):031101, 2006.

[22] Fedor Mitschke. *Fiber Optics Physics and Technology*. Springer Berlin, 2018.

[23] Andrew M Kowalevicz Jr and Frank Bucholtz. Beam divergence from an smf-28 optical fiber. Technical report, NAVAL RESEARCH LAB WASHINGTON DC, 2006.

[24] Bradley Snyder and Peter Obrien. Packaging process for grating-coupled silicon photonic waveguides using angle-polished fibers. *IEEE Transactions on Components, Packaging and Manufacturing Technology*, 3(6):954–959, 2013.

[25] Chao Li, Huijuan Zhang, Mingbin Yu, and G. Q. Lo. Cmos-compatible high efficiency double-etched apodized waveguide grating coupler. *Optics Express*, 21(7):7868, 2013.

[26] Chao Li, Koh Sing Chee, Jifang Tao, Huijuan Zhang, Mingbin Yu, and G. Q. Lo. Silicon photonics packaging with lateral fiber coupling to apodized grating coupler embedded circuit. *Opt. Express*, 22(20):24235–24240, Oct 2014.

[27] Francois Pelletier, Guillaume Robidoux, and Yves Painchaud. Fiber coupling technique on a waveguide, 2012.

[28] Victor X. D. Yang, Linda Mao, Nigel Munce, Beau Standish, Norman E. Marcon, Walter Kucharczyk, Brian C. Wilson, and I. Alex Vitkin. Interstitial doppler optical coherence tomography. *17th International Conference on Optical Fibre Sensors*, 2005.

[29] David S. Nyce. *Position sensors*. Wiley, 2016.

[30] Arup Bhattacharya, Andrew R. Metcalf, Ali Mohammadi Nafchi, and Ehsan S. Mousavi. Particle dispersion in a cleanroom – effects of pressurization, door opening and traffic flow. *Building Research Information*, 49(3):294–307, 2020.

[31] James E. Harvey and Richard N. Pfisterer. Understanding diffraction grating behavior: including conical diffraction and rayleigh anomalies from transmission gratings. *Optical Engineering*, 58(08):1, 2019.